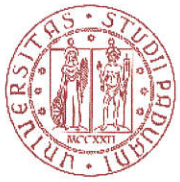

UNIVERSITÀ
DEGLI STUDI
DI PADOVA

Sede Amministrativa: Università degli Studi di Padova

DIPARTIMENTO DI INGEGNERIA DELL'INFORMAZIONE

SCUOLA DI DOTTORATO DI RICERCA IN INGEGNERIA DELL'INFORMAZIONE
INDIRIZZO: SCIENZA E TECNOLOGIA DELL'INFORMAZIONE
CICLO XXVI

TITOLO TESI

DEVELOPMENT AND CHARACTERIZATION OF GRATING-COUPLED SURFACE PLASMON RESONANCE SENSORS FOR MEDICAL AND BIOLOGICAL APPLICATIONS

Direttore della Scuola : Ch.mo Prof. Matteo Bertocco

Coordinatore d'indirizzo: Ch.mo Prof. Carlo Ferrari

Supervisore :Ch.mo Prof. Alessandro Paccagnella

Dottorando : Elisabetta Pasqualotto

Elisabetta Pasqualotto

Estratto del Verbale della riunione del Collegio dei docenti della Scuola di dottorato di ricerca in Ingegneria dell'Informazione del **12 DICEMBRE 2013 ore 15.00.**

La riunione, convocata con posta elettronica del 6 dicembre 2013 (All. A), si è tenuta nell'aula didattica Oe, Via Gradenigo 6/a, Padova.

Presenti:
Leonardo Badia, Andrea Bagno, Alessandra Bertoldo, Andrea Bevilacqua, Gianfranco Bilardi, Giancarlo Calvagno, Sergio Canazza, Luca Corradini, Guido Maria Cortelazzo, Chiara Dalla Man, Carlo Ferrari, Gaudenzio Meneghesso, Andrea Neviani, Piergiorgio Nicolosi, Enrico Pagello, Morten Pedersen, Silvano Pupolin, Giovanni Sparacino, Giorgio Spiazzi, Maria Francesca Susin, Paolo Tenti, Giuseppe Vallone, Lorenzo Vangelista, Stefano Vassanelli, Pietro Zanuttigh. Dottorandi: Chiara Fabris.

Assenti giustificati:
Alessandro Beghi (sostituisce Luca Schenato), Matteo Bertocco, Antonio D. Capobianco, Ruggero Carli, Claudio Cobelli, Barbara Di Camillo, Augusto Ferrante, Boris Kovatchev, Gabriele Manduchi, Emanuele Menegatti, Claudio Narduzzi, Gianluca Nucci, Alessandro Paccagnella, Enoch Peserico, Giorgio Satta, Federico Turkheimer, Giovanni Verzellesi, Paolo Villoresi, Harald Wimmer, Enrico Zanoni, Michele Zorzi. Dottorando: Filippo Basso

Assenti:
Federico Avanzini, Andrea Cester, Lorenzo Finesso, Nicola Laurenti, Luca Palmieri, Michele Pavon, Gianluigi Pillonetto, Michele Rossi, Francesco Ticozzi, Gianna Toffolo, Sandro Zampieri.

ORDINE DEL GIORNO

1. Approvazione verbale seduta precedente (21 maggio 2013)
2. Comunicazioni
3. Valutazione annuale dei dottorandi del primo e secondo anno e ammissione all'anno successivo
4. Ammissione all'esame finale: valutazione dell'attività svolta dai dottorandi XXVI ciclo e dai dottorandi del XXV ciclo in proroga
5. Pratiche studenti
6. Programmazione didattica 2014

Presiede la riunione il Vicedirettore Prof. Giovanni Sparacino, svolge le funzioni di Segretario il Prof. Carlo Ferrari.

Il Vicedirettore propone che **il verbale venga redatto, letto ed approvato seduta stante.**
Il Collegio approva

Il Vicedirettore propone che **il verbale venga redatto, letto ed approvato seduta stante.**
Il Collegio approva

Punto 4. All'OdG: Ammissione all'esame finale: valutazione dell'attività svolta dai dottorandi del XXVI ciclo e dai dottorandi del XXV ciclo in proroga

Il Vicedirettore illustra al collegio i risultati della valutazione condotta dalle commissioni sulla base della bozza della tesi e della presentazione dell'attività triennale svolta.

Sulla base delle valutazioni delle Commissioni (All. 4.1-4.27), il Collegio delibera all'unanimità l'ammissione all'esame finale degli studenti del XXVI ciclo e, di seguito, degli studenti del XXV ciclo in proroga:

BARI Daniele, CANALE Matteo, CARUSO Michele, CASTELLARO Marco, CHIARELLO Fabrizio, CISOTTO Giulia, DALL'ARCHE Alberto, DE SANTI Carlo, FINOTELLO Francesca, GERONAZZO Michele, MASIERO Chiara, MEZZAVILLA Marco, MICHIELETTO Stefano, MICHIELIN Francesco, MUNARETTO Daniele, MUNARO Matteo, PASQUALOTTO Elisabetta, ROSSETTO Isabella, SCHIAVON Michele, TRIFOGLIO Emanuele, VACCARI Simone, ZANANDREA Alberto, ZECCHIN Chiara, ZORDAN Davide; XXV ciclo: ARTICO Fausto, DANIELETTO Matteo, MILANI Emanuele.

Predispone la presentazione di ciascuno di essi come di seguito riportata:
.....omissis.....
Presentazione e giudizio finale sull'attività svolta da **PASQUALOTTO Elisabetta** nell'ambito del XXVI ciclo, Scuola di Dottorato di Ricerca in Ingegneria dell'Informazione, Indirizzo Scienza e tecnologia dell'informazione.

Negli anni accademici 2010/2011, 2011/2012 e 2012/2013 il dottor **PASQUALOTTO Elisabetta** ha frequentato presso il Dipartimento di Ingegneria dell'Informazione dell'Università di Padova la Scuola di Dottorato di Ricerca in Ingegneria dell'Informazione, XXVI ciclo, Indirizzo Scienza e tecnologia dell'informazione.

Titolo borsa a tema vincolato: Sviluppo di biosensori plasmonici

Il candidato dichiara quanto segue:

Parte 1 Didattica

Corsi seguiti:

- Dose, effect, threshold (Prof. Trevisan)
- Dynamical models in system biology (Prof. Altafini)
- Bioelectromagnetics (Prof. Minelli)
- Applied linear algebra (Proff. Damm e Wimmer)
- Statistical Methods (Prof. Finesso)

Seminari seguiti al DEI o in altre sedi

- "Può l'informazione modificare il cervello?", impact lecture tenuta dal Prof. Maffei della Scuola Normale Superiore di Pisa
- "Microfluidic technology for biomedical application", seminario tenuto dal Dr. Elvassore del Dipartimento di Principi e Impianti di Ingegneria Chimica
- "Donne e scienza", convegno tenuto alla scuola Galileiana Superiore di Padova
- Corso di formazione sulla banca dati brevettuale ORBIT, tenutosi al Palazzo Storione di Padova
- "Nanoelectrode and Nanofluidic Based Assays of Ion Channels, Mitochondria Membrane Potential, and Apoptosis", seminario svolto presso il complesso interdipartimentale Vallisneri dal Prof. Peter Burke, Dipartimento di Ingegneria Biomedica, Università della California, Irvine
- "Motion, Geometry and Metadata for Multimedia Compression and Delivery", distinguished lecture tenuta presso il DEI dal Prof. David Taubman, Università di New Southern Wales.
- "Brain models: from functional mapping through the connectome to self-organized criticality", distinguished lecture tenuta presso il DEI dal Dott. Federico Turkheimer, Imperial College.
- "Polymer Networks for Bioengineered Surfaces - New Bioanalytical Devices and Blood Compatible Materials", seminario tenuto presso il Dipartimento di Scienze Chimiche dal Prof. Jürgen Rühe, Università di Freiburg – IMTEK.
- "Mental maps from tactile virtual objects", seminario svolto presso il Dipartimento di Ingegneria dell'Informazione dal Dott. Luca Brayda, IIT di Genova.
- "European universities facing the Asian challenge in science and technology. The role of evaluation", distinguished lecture svolta presso il Dipartimento di Ingegneria dell'Informazione dal Dott. Andrea Bonaccorsi, Università di Pisa e ANVUR
- "Caratterizzazione del fenomeno di desincronizzazione dei ritmi cerebrali con applicazione ad una piattaforma di Brain Computer Interface per la riabilitazione motoria di pazienti reduci da ictus", seminario svolto presso il Dipartimento di Ingegneria dell'Informazione dal Prof. Pupolin e l'Ing. Giulia Cisotto, Dipartimento di Ingegneria dell'Informazione, Università di Padova

Partecipazione a Conferenze Internazionali

- PRIME 2011, 7th Conference on Ph.D. Research in Microelectronics & Electronics, 3 – 7 July 2010 Madonna di Campiglio, Trento, Italy.
- BIODEVICES 2012, 5th International Conference on Biomedical Electronics and Devices, 1-4 luglio, Vilamoura, Algarve, Portogallo.

Partecipazione alle manifestazioni:

- ExpoSanità (Bologna, 16-19 maggio 2012)
- MedTech Italy (Modena,2-3 ottobre 2012)
- MedTech Italy (Modena,2-3 ottobre 2013)

Attività di affiancamento di studenti durante il periodo di tesi

- Co-relatrice della tesi triennale "Studio sui dispositivi plasmonici".
- Co-relatrice della tesi magistrale "Integration of plasmonic based bio-sensor on silicon photodetector"

Parte 2 Ricerca

Descrizione dell'attività di ricerca durante il dottorato (max 2 pagine) mettendo particolarmente

in evidenza i risultati originali conseguiti.

Il tema principale dell'attività di ricerca che ho svolto durante il mio periodo di dottorato è stato lo studio e lo sviluppo di sensori basati sull'effetto di risonanza plasmonica per la rilevazione di molecole di interesse medico e biologico. In particolare, tra le varie configurazioni che permettono l'eccitazione plasmonica, mi sono focalizzata sullo studio dei reticoli nanostrutturati, i quali permettono di raggiungere elevate sensibilità, se paragonati con i dispositivi accoppiati con prisma, e di miniaturizzare il sistema di misura.

Inizialmente la mia attività si è concentrata sullo sviluppo di un banco opto-elettronico che permettesse di rilevare il segnale plasmonico e trasdurlo in un segnale elettrico. L'obiettivo era di costruire un banco versatile, che permettesse di misurare sia la trasmittanza che la riflettanza del grating, oltre che di variare i parametri che entrano in gioco nella configurazione conica, ossia l'angolo di incidenza della luce, l'angolo azimutale, che si crea tra il piano di scattering e il vettore del reticolo, e la polarizzazione della luce incidente. La luce riflessa o trasmessa viene poi trasdotta in corrente grazie ad un array di fotodiodi, e il segnale viene poi acquisito attraverso un analizzatore di parametri.

Grazie a questo banco ho potuto analizzare il comportamento opto-elettronico di tre reticoli diversi:

- Un reticolo d'oro digitale, ideato per la trasmissione straordinaria della luce, e fabbricato attraverso litografia a fascio di elettroni (EBL) dal laboratorio LaNN (Laboratorio di ricerca per la Nanofabbricazione e i Nanodispositivi). Lo sviluppo di questo sensore è l'obiettivo del progetto SPLENDID, progetto di Eccellenza Cariparo, cui ho partecipato. Si è analizzata la luce trasmessa attraverso il reticolo al variare della polarizzazione del fascio incidente sia in stato "fresh" sia dopo un processo di funzionalizzazione con dodecanethiol, ossia una molecola composta da una catena di dodici atomi di carbonio in grado di creare un layer di spessore e indice di rifrazione noti.
- Un reticolo d'oro sinusoidale, ideato per misure di riflettanza con modulazione in polarizzazione delle luce incidente, e fabbricato dal LaNN attraverso litografia interferenziale. Lo sviluppo di questo sensore è l'obiettivo del progetto PLATFORMS, progetto di Strategico dell'Università di Padova, cui ho partecipato. E' stato messo a punto un protocollo di misura in grado di identificare la configurazione di lavoro più sensibile e di fissare, quindi, i parametri di angolo di incidenza e azimutale, in modo da effettuare misure al variare della sola polarizzazione. Quest'ultima è stata considerata l'unico parametro di sensing. Ho poi stimato la sensibilità del sensore grazie a misure di "bulk" con indici di rifrazione diversi. Il sensore è stato inoltre testato per rilevare due molecole biologiche: l'avidina, sfruttando il legame avidina-biotina, e una catena di DNA, immobilizzando sulla superficie del reticolo la catena di acido peptidonucleico (PNA) complementare. I risultati ottenuti, che presentano una buona corrispondenza con i dati simulati, hanno evidenziato l'elevata sensibilità del sistema e la sua efficacia nel rilevare molecole biologiche.
- Un reticolo trapezoidale in argento, ottimizzato per una misura di trasmittanza e realizzato attraverso un processo industriale che ho contribuito a mettere a punto grazie ad una collaborazione con lo Spin-Off dell'università Next Step Engineering. Questi reticoli sono stati poi caratterizzati dal punto di vista opto-elettronico con il banco

sviluppato e ne è stato studiato il comportamento al variare di alcuni parametri geometrici, ottenuti con opportune modifiche del processo produttivo, e al variare dell'angolo di incidenza della luce e quello azimutale. L'efficacia del sistema di rilevazione di variazioni superficiali è stata valutata sia con soluzioni a diversi indici di rifrazione, utilizzando una cella microfluidica, sia attraverso l'immobilizzazione sulla superficie del reticolo di alcantioli di diversa lunghezza. I risultati ottenuti hanno evidenziato l'elevate performance del sensore e la buona ripetibilità data anche dal processo di produzione. Tutti i dati sperimentali sono in accordo con i risultati delle simulazioni.

Nel corso del mio dottorato ho collaborato con due Spin-Off, Next Step Engineering e Wetware Concepts. Grazie a questa collaborazione ho contribuito a mettere a punto un sistema produttivo per la fabbricazione di reticoli nano strutturati, utilizzati poi all'interno della mia attività di ricerca, e di sensori microelettronici per rilevazioni elettrochimiche di molecole. Tale processo produttivo è stato anche modificato per permettere la creazione di sistemi microfluidici con la possibilità di essere integrati con gli elettrodi. Il processo di produzione è oggetto di un brevetto italiano attualmente in fase di deposito, di cui sono una degli inventori.

Durante i primi anni di dottorato, all'attività principale di sviluppo di sensori plasmonici ho affiancato altre attività, tra cui lo studio di protocolli di funzionalizzazione di superfici in oro con poly-L-lysine, attraverso misure di spettroscopia d'impedenza elettrochimica (EIS) e ciclovoltammetrie; e lo sviluppo di un guanto per la riabilitazione, che grazie alla presenza di sensori di forza, è in grado di monitorare i miglioramenti di un soggetto che ha subito delle lesioni all'arto. Sono stati valutati anche dei particolari tessuti che, opportunamente utilizzati, permettono di rilevare variazioni di pressione.

Ho inoltre partecipato alla business competition "Start Cup 2011", presentando un prodotto innovativo per la rilevazione di patogeni (*Brettanomyces*) nel vino, basato su sonde di DNA. Tale idea è nata dalla fusione delle nostre competenze ingegneristiche, all'interno del laboratorio Biodevices del Dipartimento di Ingegneria dell'Informazione, e delle competenze biotecnologiche di un laboratorio dell'Università di Verona, e si è classificata terza alla finale regionale, candidandosi al Premio Nazionale dell'Innovazione 2011.

Titolo definitivo della tesi

Development and characterization of grating-coupled surface plasmon resonance sensors for medical and biological applications

Supervisore: Prof. Alessandro Paccagnella

Parte 3 Pubblicazioni

Elenco pubblicazioni su rivista internazionale

- Mufti Mahmud, **Elisabetta Pasqualotto**, Alessandra Bertoldo, Stefano Girardi, Marta Maschietto, Stefano Vassanelli: "An automated method for detection of layer activation order in information processing pathway of rat barrel cortex under mechanical whisker stimulation". Journal of Neuroscience Methods, Volume 196, Issue 1, 15 March 2011, Pages 141-150.

- A. Ferrario, M. Scaramuzza, **E. Pasqualotto**, A. De Toni, A. Paccagnella. "Development of a Disposable Gold Electrodes-Based Sensor for Electrochemical Measurements of cDNA Hybridization". Procedia Chemistry, Volume 6, 2012, Pages 36–45. (http://www.sciencedirect.com/science/article/pii/S1876619612002021)
- M. Scaramuzza, A. Ferrario, **E. Pasqualotto**, A. De Toni. "Development of an Electrode/Electrolyte Interface Model Based on Pseudo-Distributed Elements Combining COMSOL, MATLAB and HSPICE". Procedia Chemistry, Volume 6, 2012, Pages 69–78. (http://www.sciencedirect.com/science/article/pii/S1876619612002069#)
- **E. Pasqualotto**, A. Ferrario, M. Scaramuzza, A. De Toni, M. Maschietto. "Monitoring Electropermeabilization of Adherent Mammalian Cells Through Electrochemical Impedance Spectroscopy". Procedia Chemistry, Volume 6, 2012, Pages 79-88. (http://www.sciencedirect.com/science/article/pii/S1876619612002070)
- Ferrario, M. Scaramuzza, **E. Pasqualotto**, A. De Toni, A. Paccagnella, "Coadsorption optimization of DNA in binary self assembled monolayer on gold electrode for electrochemical detection of oligonucleotide sequences", Journal of Electroanalytical Chemistry, Volume 689, 15 January 2013, Pages 57-62, ISSN 1572-6657, http://dx.doi.org/10.1016/j.jelechem.2012.11.029.
- **E. Pasqualotto**, G. Ruffato, A. Sonato, G. Zacco, D. Silvestri, M. Morpurgo, A. De Toni and F. Romanato. "Plasmonic platforms for innovative surface plasmon resonance configuration with sensing applications". Microelectronic Engineering, Volume 111, November 2013, Pages 348–353. http://dx.doi.org/10.1016/j.mee.2013.02.088
- G. Ruffato, **E. Pasqualotto**, A. Sonato, G. Zacco, D. Silvestri, M. Morpurgo, A. De Toni, F. Romanato, "Implementation and testing of a compact and high-resolution sensing device based on grating-coupled surface plasmon resonance with polarization modulation", Sensors and Actuators B: Chemical, Volume 185, August 2013, Pages 179-187, ISSN 0925-4005, http://dx.doi.org/10.1016/j.snb.2013.04.113.

Elenco pubblicazioni su convegno internazionale

- Mufti Mahmud, Alessandra Bertoldo, Stefano Girardi, Marta Maschietto, **Elisabetta Pasqualotto**, Stefano Vassanelli. "An Automated Method to Determine Angular Preferentiality using LFPs Recorded from Rat Barrel Cortex by Brain-Chip Interface under Mechanical Whisker Stimulation". International Conference of the IEEE Engineering in Medicine and Biology Society (EMBC'11)
- Mufti Mahmud, Alessandra Bertoldo, Stefano Girardi, Marta Maschietto, Elisabetta Pasqualotto, Stefano Vassanelli. "SigMate: A Comprehensive Software Package for Extracellular Neuronal Signal Processing and Analysis". 5th International IEEE EMBS Conference on Neural Engineering 2011.

- A. Ferrario, M. Scaramuzza, **E. Pasqualotto**, A. De Toni, A. Paccagnella, M. Maschietto, S. Vassanelli. "Electrochemical impedance spectroscopy study of the cells adhesion over microelectrodes array". *Ph.D. Research in Microelectronics and Electronics (PRIME), 2011 7th Conference on* , vol., no., pp.57-60, 3-7 July 2011 doi: 10.1109/PRIME.2011.5966216 URL: http://ieeexplore.ieee.org/stamp/stamp.jsp?tp=&arnumber=5966216&isnumber=5966131
- Scaramuzza M., Ferrario A., **Pasqualotto E.**, Rosati G., DeToni A., Quarta M.,Paccagnella A., Reggiani C.(2012). LOW-COST ENZYME-BASED BIOSENSOR FOR LACTIC ACID AMPEROMETRIC DETECTION-Electrical Modeling and Validation for Clinical and Food Processing Applications. In Proceedings of the International Conference on Biomedical Electronics and Devices, pages 380-383 DOI: 10.5220/0003867603800383
- Marta Maschietto, Stefano Girardi, Florian Felderer, **Elisabetta Pasqualotto**, Stefano Vassanelli. "High Resolution Recordings Of Local Field Potentials With Transistor Needle Chips In Rat Somatosensory and Motor Cortexes". In Proceedings of MEA-Meeting 2012.
- Gianluca Ruffato, **Elisabetta Pasqualotto**, Agnese Sonato, Gabriele Zacco, Davide Silvestri, Monica Dettin, Margherita Morpurgo, Alessandro De Toni, Filippo Romanato, "Novel compact architecture for high-resolution sensing with plasmonic gratings in conical mounting". Proc. of SPIE Vol. 8722, 87220U, doi: 10.1117/12.2014272

Elenco lavori presentati a convegni nazionali/internazionali

- Perino M., **Pasqualotto E.** , Onganello T, Scaramuzza M., Zilio P. *, De Toni A. and Romanato F., "Plasmonic Grating based Biosensor: Design, Fabrication and Testing" Presented at Nanotechitaly 2011, 23-25 November 2011, Venice, Italy.
- M.Perino, T.Ongarello, P.Zilio, **E. Pasqualotto**, M. Scaramuzza, A. De Toni and F.Romanato. "Design, Fabrication and testing of a biosensor using Plasmonic Gratings". Presented at 37th International Conference on Micro and Nano Engineering,19 - 23 September 2011, Berlin, German.
- G. Ruffato, **E. Pasqualotto**, A. Sonato, G. Zacco, D. Silvestri, M. Morpurgo, A. De Toni and F. Romanato. "Ultra-compact grating-coupled plasmonic sensing for high-resolution analysis with polarization modulation". E-MRS 2012, May 14-18 2012, Strasbourg, France.
- **E. Pasqualotto**, G. Ruffato, A. Sonato, G. Zacco, D. Silvestri, M. Morpurgo, A. De Toni and F. Romanato. "Plasmonic platforms for innovative surface plasmon resonance configuration with sensing applications". MNE, 38th International Conference on Micro and Nano Engineering, 16-20th September 2012.
- M. Perino, **E. Pasqualotto**, S. Guggia, G. Rosati, A. Ferrario,M. Scaramuzza, G. Ruffato, A. De Toni, F. Romanato, A. Paccagnella' "Transmitted Signals from Grating Coupling Surface Plasmon Resonant Device for Detection of Alkanethiols Functionalization Layers", 2nd International Conference on Bio-Sensing Technology 2013
- Gianluca Ruffato, **Elisabetta Pasqualotto**, Agnese Sonato, Gabriele Zacco, Davide Silvestri, Monica Dettin, Margherita Morpurgo, Alessandro De Toni, Filippo Romanato, "Innovative sensing architecture based on symmetry breaking of grating-coupled surface plasmon resonance", 1st EOS Topical Meeting on Optics at the Nanoscale 12-14 September 2013, Capri, Italy

Brevetti italiani attualmente in fase di deposito:

- Metodo e apparato per definire e mantenere l'orientazione di dischi polimerici all'interno di processi produttivi industriali di supporti polimerici di immagazzinamento dati digitali.

Il Collegio prende atto di quanto esposto e osserva che durante i tre anni della Scuola di Dottorato il dott. **PASQUALOTTO Elisabetta** si è impegnato con dedizione e profitto nella sua attività di ricerca e di studio, evidenziando un'ottima capacità di lavorare sia in maniera autonoma che all'interno di un gruppo di ricerca. Il Collegio unanime riconosce la notevole assiduità del candidato, le sue ottime capacità nella ricerca e gli originali risultati conseguiti.

Pertanto il collegio lo ammette all'esame finale.

.....omissis.....

Letto, approvato e sottoscritto
Padova, 12/12/2013

Il Segretario

Il Direttore della Scuola

Allegato A

Oggetto: Scuola di dottorato - Riunione collegio docenti giovedì 12 dicembre 2013 ore 15.00
Mittente: Alessandra Calore <calore@dei.unipd.it>
Data: 06/12/2013 16:16
A: avanzini@dei.unipd.it, badia@dei.unipd.it, andrea.bagno@unipd.it, alessandro.beghi@dei.unipd.it, mat@dei.unipd.it, alessandra.bertoldo@dei.unipd.it, andrea.bevilacqua@dei.unipd.it, gianfranco.bilardi@dei.unipd.it, giancarlo.calvagno@dei.unipd.it, canazza@dei.unipd.it, antonio.capobianco@dei.unipd.it, carlirug@dei.unipd.it, andrea.cester@dei.unipd.it, claudio.cobelli@dei.unipd.it, luca.corradini@dei.unipd.it, guidomaria.cortelazzo@dei.unipd.it, dallaman@dei.unipd.it, barbara.dicamillo@dei.unipd.it, augusto@dei.unipd.it, carlo.ferrari@dei.unipd.it, lorenzo.finesso@isib.cnr.it, bpk2u@virginia.edu, nicola.laurenti@dei.unipd.it, gabriele.manduchi@igi.cnr.it, emanuele.menegatti@dei.unipd.it, gaudenzio.meneghesso@dei.unipd.it, claudio.narduzzi@dei.unipd.it, andrea.neviani@dei.unipd.it, piergiorgio.nicolosi@dei.unipd.it, alessandro.paccagnella@dei.unipd.it, enrico.pagello@dei.unipd.it, luca.palmieri@dei.unipd.it, michele.pavon@unipd.it, pedersen@dei.unipd.it, enoch.peserico@dei.unipd.it, gianluigi.pillonetto@dei.unipd.it, silvano.pupolin@dei.unipd.it, michele.rossi@dei.unipd.it, giorgio.satta@dei.unipd.it, schenato@dei.unipd.it, giovanni.sparacino@dei.unipd.it, giorgio.spiazzi@dei.unipd.it, francescamaria.susin@unipd.it, tenti@dei.unipd.it, ticozzi@dei.unipd.it, toffolo@dei.unipd.it, federico.turkheimer@imperial.ac.uk, vallone@dei.unipd.it, lorenzo.vangelista@unipd.it, stefano.vassanelli@unipd.it, giovanni.verzellesi@unimore.it, paolo.villoresi@dei.unipd.it, sandro.zampieri@dei.unipd.it, enrico.zanoni@dei.unipd.it, zanuttigh@dei.unipd.it, michele.zorzi@dei.unipd.it, bassofil@dei.unipd.it, chiara.fabris@dei.unipd.it

Ai Componenti il Collegio dei Docenti
Scuola di Dottorato in Ingegneria dell'Informazione

Siete invitati a partecipare alla riunione che avrà luogo

Giovedì 12 dicembre p.v. alle ore 15.00
in aula didattica Oe, Via Gradenigo 6/a, Padova,

con il seguente ordine del giorno

1. Approvazione verbale seduta precedente
2. Comunicazioni
3. Valutazione annuale dei dottorandi del primo e secondo anno e ammissione all'anno successivo
4. Ammissione all'esame finale: valutazione dell'attività svolta dai dottorandi del XXVI ciclo e dai dottorandi del XXV ciclo in proroga
5. Pratiche studenti
6. Programmazione didattica 2014

Prof. Giovanni Sparacino
vicedirettore

Collegio docenti 12/12/2013

pag. n. 17

DEI
DIPARTIMENTO DI
INGEGNERIA DELL'INFORMAZIONE

UNIVERSITÀ
DEGLI STUDI
DI PADOVA

via Gradenigo, 6/B
35131 Padova, Italy
tel +39 049 8277600
fax +39 049 8277699
info@dei.unipd.it
www.dei.unipd.it

CF 80006480281
P.IVA 00742430283

Al Collegio dei Docenti della
Scuola di Dottorato in
Ingegneria dell'Informazione
Padova, 19 novembre 2013

OGGETTO: *Parere sull'ammissibilità della studentessa di dottorato Pasqualotto Elisabetta all'esame finale.*

La commissione si è riunita il 19 novembre 2013 alle ore 11.30 in sala 201 DEI/A per assistere ad una presentazione tenuta dalla dottoranda Elisabetta Pasqualotto relativa all'attività di ricerca da lei svolta nel triennio di studi in via di conclusione. La dottoranda ha lavorato nell'ambito dei biosensori per applicazioni biologiche e mediche.

L'attività di ricerca svolta da Elisabetta Pasqualotto si è incentrata sullo studio e lo sviluppo di sensori basati sull'effetto di risonanza plasmonica per la rilevazione di molecole di interesse medico e biologico. In particolare, tra le varie configurazioni che permettono l'eccitazione plasmonica, ha approfondito lo studio dei grating nanostrutturati.

La studentessa ha dapprima sviluppato un banco di misura per la trasduzione del segnale plasmonico in un segnale elettrico. Il banco realizzato è versatile ed è in grado di misurare sia la trasmittanza che la riflettanza della luce modulata dai grating, permettendo di variare tutti parametri che entrano in gioco nella configurazione conica e che influenzano il fenomeno di risonanza plasmonica.

Grazie a questo banco di misura la dottoranda ha analizzato tre tipi di grating con caratteristiche differenti e ottimizzati per diversi tipi di analisi. Uno è stato ideato per misure di riflettanza con modulazione in polarizzazione delle luce incidente; è stato dapprima caratterizzato attraverso misure di soluzioni a diverso indice di rifrazione e successivamente è stato applicato per la rilevazione di sostanze di interesse biologico, quali avidina e catene di DNA. Un altro grating, ideato per la trasmissione straordinaria della luce, è di tipo digitale e ne è stata analizzata la transmittanza al variare della polarizzazione della luce incidente sia prima che dopo un processo di funzionalizzazione con una molecola benchmark (dodecanethiol). Il terzo grating è stato sviluppato dalla dottoranda in collaborazione con uno spin-off dell'università ed è stato caratterizzato attraverso misure di soluzioni a diverso indice di rifrazione e funzionalizzazioni con molecole formate da catene di carbonio di diversa lunghezza (alkantioli).

La qualità dei risultati ottenuti è documentata anche dalle pubblicazione di cui la dottoranda è coautrice, tra cui 7 lavori su rivista, 6 lavori su atti di conferenze internazionali e un brevetto in fase di deposito.

Dall'analisi della bozza della tesi emerge che l'ossatura della stessa è già ben delineata per cui, tenuto conto del materiale già disponibile nelle pubblicazioni di cui la dottoranda è coautrice, lo stato di avanzamento del lavoro è giudicato dalla commissione pienamente in linea con l'obiettivo di completare la versione definitiva entro fine gennaio 2014.

Complessivamente, la commissione formula un giudizio pienamente positivo sull'attività di ricerca svolta da Elisabetta Pasqualotto e ne propone l'ammissione all'esame finale.

Il supervisore della dottoranda

Prof. A. Paccagnella

Prof.ssa A. Bertoldo

Prof. A. Neviani

L'uomo che comincia con certezza finisce nel dubbio,
ma colui che comincia nel dubbio finisce con la certezza.
(Francis Bacon)

TABLE OF CONTENTS

List of abbreviations and acronyms 5

Abstract 7

Introduction 15

1 Surface Plasmon Polaritons 19

1.1 Plasmon Polaritons theory 19

1.2 Excitation of Surface Plasmon Polaritons 28

1.2.1 Prism coupler 28

1.2.2 Grating coupler 29

1.3 Sensors based on Surface Plasmon Resonance (SPR) effect 31

1.3.1 Performance 33

Linearity 36

1.3.2 Biorecognition elements and applications for the detection of chemical and biological molecules 36

1.3.3 Advances in SPR biosensor technology 40

2 Plasmonic devices and experimental configurations 43

2.1 Grating coupling SPR sensors 43

2.1.1 Gold sinusoidal gratings for reflectance analysis 44

2.1.2 Gold digital gratings for Extraordinary Optical Transmission 46

2.1.3 Silver trapezoidal gratings for transmittance analysis 48

2.2 Measurement equipments 50

2.2.1 Reflectance analysis configuration 51

2.2.2 Transmittance analysis configuration 54

2.2.3 Test bench electrical characterization 57

2.3 Functionalization processes 60

2.4 Microfluidic chips fabrication 67

3 Theoretical analysis and simulations 69

3.1 Vector model of gold sinusoidal grating 69
3.1.1 Non-zero azimuthal incident angle analysis 70
3.1.2 Dependency on incident light polarization 73
3.2 Simulation of gold digital grating through Finite Elements Method (FEM) 75
3.3 Simulations of silver trapezoidal grating: vector model and Rigorous Coupled-Wave Analysis (RCWA) 80
4 Experimental results 89
4.1 Measurements of gold sinusoidal grating reflectance 89
4.1.1 Measurement protocol 89
4.1.2 Response to bulk variations of refractive index : analysis of saline solutions 91
4.1.3 Measurements of surface variations of refractive index: detection of bio-analytes 94
4.1.3.1 Avidin detection 94
4.1.3.2 DNA detection 97
4.2 Measurements of gold digital grating transmittance 100
4.2.1 Measurement protocol 100
4.2.2 Measurements of surface refractive index variations 101
4.3 Measurements of silver trapezoidal grating transmittance 104
4.3.1 Measurement protocol 104
4.3.2 Bare grating characterization 105
4.3.3 Response to bulk variations of refractive index: analysis with different solutions 113
4.3.4 Measurements of surface refractive index variations: functionalization with increasing length alkanethiols 118
5 Conclusions 125

Appendix A 129

Acknowledgment 135

Bibliography 137

List of abbreviations and acronyms

AFM	Atomic Force Microscopy
ATR	Attenuated Total Reflection
A.U.	Arbitrary Unit
C_6	1-Mercaptohexane (or Hexanethiol)
C_8	n-Octylmercaptan (or Octanethiol)
C_{12}	n-Dodecyl mercaptan (or Dodecanethiol)
C_{18}	Mercaptan C18 (or Octadecanethiol)
CCD	Charge-Coupled Device
CM	Cavity Mode
DNA	Deoxyribonucleic acid
EBL	Electron Beam Lithography
EM	Electromagnetic
EMA	Effective Medium Approximation
EOT	Extraordinary Optical Transmission
FEM	Finite Elements Method
GCSPR	Grating-Coupled Surface Plasmon Resonance (sensor)
ITO	Indium Tin Oxide
LIL	Laser Interference Lithography
NOA	Norland Optical Adhesive
PCB	Printed Circuit Board
PCSPR	Prism-Coupled Surface Plasmon Resonance (sensor)
PDMS	Polydimethylsiloxane
PEO	Poly(ethylene oxide)
PGMEA	Propylene glycol monomethyl ether acetate
PVD	Physical Vapor Deposition
PMMA	Polymethylmethacrylate
PNA	Peptide Nucleic Acids

RI	Refractive Index
RIU	Refractive Index Unit
RCWA	Rigorous Coupled Wave Analysis
SAM	Self-Assembled Monolayer
SEM	Scanning Electron Microscope
SPPs	Surface Plasmon Polaritons
SPR	Surface Plasmon Resonance
TM	Transverse Magnetic
TE	Transverse Electric
VIS-IR	Visible-Infrared

Abstract

Italiano

Il tema principale dell'attività di ricerca che ho svolto durante il mio periodo di Dottorato in Scienza e Tecnologia dell'Informazione è stato lo studio e lo sviluppo di sensori basati sull'effetto di risonanza plasmonica per la rilevazione di molecole di interesse medico e biologico.

In particolare, tra le varie configurazioni che permettono l'eccitazione plasmonica, mi sono focalizzata sullo studio dei reticoli nanostrutturati, i quali permettono di raggiungere elevate sensibilità, se paragonati ai dispositivi accoppiati con prisma, e di miniaturizzare e integrare il sistema di misura come obiettivo nel lungo periodo.

Inizialmente la mia attività si è concentrata sullo sviluppo di un banco opto-elettronico che permettesse di rilevare il segnale plasmonico e trasdurlo in un segnale elettrico. Il banco doveva essere in grado di variare indipendentemente alcuni parametri determinanti per l'eccitazione plasmonica, ossia l'angolo di incidenza del fascio laser, l'angolo azimutale tra il piano di scattering e il vettore del reticolo, e la polarizzazione della luce incidente. La luce modulata dal reticolo viene poi trasformata in corrente elettrica attraverso un array di fotodiodi, e quindi acquisita attraverso un analizzatore di parametri. Ho mirato a realizzare un banco molto versatile in modo da poter effettuare misure sia di riflettanza, andando ad analizzare la luce riflessa dal reticolo, sia di trasmittanza, analizzando la luce trasmessa dal campione. L'introduzione di uno stadio motorizzato ha permesso di rendere la misura più automatizzata e gestibile via software, attraverso un programma custom sviluppato in LabVIEW, e lasciando manuali solo pochi passaggi iniziali.

Ho analizzato tre tipologie diverse di reticoli:

- Reticolo d'oro con superficie sinusoidale, ottimizzato per effettuare misure in riflessione con modulazione della polarizzazione della luce incidente, sfruttando l'aumento di sensibilità derivante dall'angolo azimutale non nullo. Tale reticolo è stato fornito dal laboratorio LaNN (Laboratorio di ricerca per la Nanofabbricazione e i Nanodispositivi) del Consiglio Nazionale delle Ricerche (CNR) di Padova. Il reticolo è stato realizzato attraverso litografia interferenziale di uno strato di fotoresist deposto su un vetrino (o silicio), da cui è stato ricavato uno stampo che permette la

replica della nano struttura; infine, attraverso un'evaporazione termica, è stato depositato uno strato d'oro. Inizialmente ho analizzato il reticolo in condizione "fresh"; successivamente ho effettuato misure di "bulk" con indici di rifrazione diversi, per poter stimare la sensibilità del sensore. Ho poi misurato la capacità del dispositivo nel rilevare molecole di interesse biologico, dapprima attraverso prove di rilevazione di avidina presente in una soluzione, sfruttando il legame avidina-biotina, poi con prove di rilevazione di singole catene di DNA, attraverso l'immobilizzazione sulla superficie della nanostruttra di acido peptidonucleico (PNA) complementare.

- Reticolo d'oro digitale, ideato per sfruttare il fenomeno di trasmissione straordinaria della luce. Tale reticolo è stato realizzato dal laboratorio LaNN del CNR di Padova attraverso la tecnica di litografia a fascio di elettroni (Electron Beam Lithography-EBL) e nasce con l'obiettivo di creare un sistema di rilevazione estremamente semplice, poiché l'unico parametro di sensing, e quindi variabile, è la polarizzazione della luce incidente. La capacità del sistema di discriminare variazioni superficiali di indice di rifrazione è stata valutata funzionalizzando il reticolo con dodecanethiol, ossia una molecola composta da una catena di dodici atomi di carbonio in grado di formare uno strato di dimensioni e indice di rifrazione noti.
- Reticolo trapezoidale in argento, nato dalla collaborazione con lo Spin-Off Next Step Engineering, che mi ha coinvolta nell'ultimo periodo di dottorato. Infatti, ho partecipato in prima persona alla realizzazione del sensore, sfruttando le facilities industriali a cui l'azienda ha accesso, permettendo di produrre dispositivi a basso costo e in elevate quantità, quindi adatti ad un utilizzo di tipo "usa e getta". Il processo di fabbricazione prevede la realizzazione di uno stampo attraverso litografia interferenziale, una fase di replica a stampo su substrato polimerico e la deposizione di uno strato metallico per polverizzazione catodica. Tali sensori sono stati ottimizzati per la misura della luce trasmessa e si è analizzato il comportamento al variare dell'angolo di incidenza e dell'angolo azimutale. Si è quindi misurato il comportamento del sensore in presenza di bulk ad indici di rifrazione diversi per la stima della sensibilità, e successivamente si sono effettuate misure funzionalizzando il campione con alcantioli di diversa lunghezza.

I risultati sperimentali sono stati confrontati con quelli ottenuti dalle simulazioni. Infatti si è studiato il comportamento di ogni reticolo attraverso metodi di simulazione diversi. In particolare il reticolo digitale in oro è stato studiato attraverso il metodo degli

elementi finiti (FEM) implementato in COMSOL Multiphysics, il modello vettoriale è stato applicato sia per lo studio del reticolo sinusoidale in oro che del reticolo trapezoidale in argento. Quest'ultimo reticolo è stato analizzato anche attraverso il metodo RCWA (Rigorous Coupled Wave Analysis).

Come già accennato, durante l'ultimo periodo di dottorato ho contribuito a sviluppare, in collaborazione con lo Spin-Off dell'università di Padova Next Step Engineering, un innovativo processo di produzione industriale che consente di creare non solo reticoli per la rilevazione di segnali plasmonici, ma anche dispositivi ibridi elettronici/microfluidici per applicazioni biologiche e mediche, all'interno di una singola linea produttiva automatizzata. Con questo processo ho prodotto i reticoli in argento, che ho utilizzato per la mia attività sperimentale. Il processo di produzione è oggetto di un brevetto italiano attualmente in fase di deposito, di cui sono uno degli inventori.

Durante il dottorato ho approfondito anche lo sviluppo di dispositivi microfluidici sia attraverso tecniche di incisione polimerica, in grado di creare profili di taglio netti senza deformarne la struttura planare, sia apportando le appropriate modifiche al processo produttivo utilizzato da Next Step Engineering, precedentemente citato. I dispositivi realizzati sono stati utilizzati per le misure di bulk a diversi indici di rifrazione utilizzando i reticoli in argento.

English

The core of my research activity during the Ph.D. period has been the study and the development of Surface Plasmon Resonance (SPR) based sensors for the detection of molecules of biological and medical interest.

In particular, between the different configurations allowing plasmon excitation, I have focused my research on the study of nanostructured gratings, which allow to achieve a higher sensitivity than the prism coupled sensors and to miniaturize the measurement system.

First my activity focused on the development of an opto-electronic bench able to detect plasmonic signal and to transduce it into an electric one. The test bench must allow varying independently some parameters that are fundamental for plasmonic excitation, such as the incident angle of laser beam, the azimuthal angle between the scattering plane and the grating vector, and the incident light polarization. The light modulated by the grating is transduced into electrical current through a photodiodes array and then acquired by a parameters analyzer. I have realized a versatile bench in order to perform measurements of both reflectance, analyzing the light reflected from the grating, and transmittance. The use of a motorized rotation stage has automated the measurement and it is controlled by a custom National Instruments LabVIEW software: in this way only few initial steps must be manually performed.

I have analyzed three types of gratings:

- Gold sinusoidal grating, optimized for reflectance measurements in incident light polarization modulation, exploiting the sensitivity increase due to a non-zero azimuthal angle. This grating has been provided us by LaNN laboratory (Laboratory of research for Nanofabrication and Nanodevices) of National Council of Research (CNR) of Padova. The grating has been manufactured through lithography (by Laser Interference Lithography-LIL) of a photoresist deposited over a glass (or silicon wafer), nanostructure replica and thermal evaporation of the gold plasmonic layer. First I have analyzed the bare grating, and then I have measured bulk with different refractive indexes in order to estimate sensor sensitivity. Then I have measured if the sensor is able to detect biological molecules, first through tests of avidin detection, exploiting avidin-biotin binding, and then through tests of DNA detection, via complementary Peptide Nucleic Acid (PNA) immobilization.

- Gold digital grating, that exploits light extraordinary transmission. This grating has been fabricated by LaNN laboratory of CNR of Padova through Electron Beam Lithography (EBL) technique, and it has been designed in order to realize a simple and compact detection system, since the only sensing parameter considered is incident light polarization. Grating ability to detect surface changes of refractive index has been evaluated by a functionalization process with dodecanethiol, that is a molecule composed of a chain of twelve carbon atoms that forms a layer of well-known thickness and refractive index.
- Silver trapezoidal grating, developed thanks to the collaboration with the Spin-Off Next Step Engineering, that has involved me in the last months of my Ph.D.. In fact, I have participated in grating fabrication exploiting the industrial facilities of the Spin-Off, which allow producing high quantity of low-cost devices, suitable to be a disposable sensor. The manufacturing process consists of the development of a stamper obtained through interferential lithography, the replica molding of polymeric substrate and the metal layer deposition through sputtering. These gratings have been optimized for transmittance measurements and their response as a function of incident light and azimuthal angles has been analyzed. Measurements of bulk with different refractive indexes, in order to estimate sensor sensitivity, and then of grating functionalized with different lengths alkanethiols have been performed.

All experimental data have been compared with simulations results. In fact the behavior of the gratings has been studied through different simulation methods. In particular the digital gold grating has been studied through Finite Element Method (FEM) implemented in COMSOL Multiphysics; the vector model has been applied for both sinusoidal gold gratings and trapezoidal silver ones. The latter grating has been also analyzed through Rigorous Coupled Wave Analysis (RCWA).

As already mentioned, during the last period of my Ph.D., I have collaborated with Next Step Engineering to develop an innovative industrial process that allows creating both grating for plasmonic events detection and electronic/microfluidic hybrid devices within a single, well-established, production line. With this process I have manufactured all the custom devices I used for my experimental activity. Moreover, this industrial process is the object of an Italian patent that is now pending and I am one of the inventors.

During my PhD I have also developed microfluidic devices through a particular technique of polymer etching, able to create clear-cut profiles without deforming the planar structure, and also through suitable changes of production process adopted by Next Step Engineering, previously mentioned. The former devices have been used with silver gratings for the measurements of bulk with different refractive indexes.

Introduction

Surface Plasmon Polaritons (SPPs) are electromagnetic excitations propagating along the interface between a noble metal medium, usually gold or silver, and a dielectric one. They originate from the coupling of electromagnetic waves with electron surface plasma inside the metal.

Electromagnetic (EM) fields intensity decays exponentially with the increasing of distance from the metal/dielectric interface, so SPPs are confined within few hundreds of nanometers and they are very sensitive to refractive index (RI) changes occurring at the surface. This is why optical sensors based on excitation of SPPs have been widely studied for the detection of chemical and biological molecules.

In last decades Plasmonic has known an increasing interest in a growing range of scientific fields and its advances and progress have offered promising ideas for applications in many areas: sensing, solar cells, optoelectronics and communications. The possibility to exploit material properties at the nanoscale and to control light interaction with matter revealed new unexpected phenomena and opened the route to new research-threads in many disciplines: physics, material science and information engineering, biotechnology, biochemistry and medicine. In this way Plasmonic has increasingly become a cross-disciplinary research field, where contributions of different backgrounds, engineering and physics as well as biology and chemistry, is needed in order to provide the required know-how so to design and realize such plasmonic devices.

Since SPPs momentum is greater than light in vacuum, they have a non-radiative nature. As a consequence, SPPs excitation by incident light is possible only assembling proper optical configurations. In Otto's and Kretschmann-Raether's configurations, the excitation coupling is achieved by increasing the incident light momentum with the use of a high refractive index prism. The recent advances in nanofabrication methods and nanoparticle synthesis are leading to the advent of a variety of new nanostructures that can resonantly be excited by visible light to produce SPPs. These are gratings obtained by a periodic pattern of metallic multilayer. The diffraction is exploited in order to comply with the momentum equality between SPPs and incident light.

Grating Coupling Configurations have a higher number of degrees of freedom with respect to the Prism Coupling Configurations, such as incident angle, azimuthal angle and light polarization.

In this work three different gratings have been analyzed:

1) a gold sinusoidal grating for reflectance analysis: the reflected light as a function of incident light polarization has been studied, exploiting the increased sensitivity due to the non-zero azimuthal angle. It has been provided us by LaNN laboratory (Laboratory for Nanofabrication of Nanodevices) of CNR (National Council of Research) of Padova
2) a gold digital grating for Extraordinary Optical Transmission (EOT): the transmitted light as a function of incident light polarization has been analyzed. It has been provided us by LaNN laboratory of CNR of Padova
3) a silver trapezoidal grating for transmittance analysis: it has been fabricated in collaboration with Next Step Engineering, a Spin-Off of the Department of Information Engineering. It has been analyzed as a function of incident and azimuthal angles.

Gratings behavior has been studied as a function of mentioned parameters and simulations allow us to compute theoretical excitation conditions. In order to carry out experimental measurements, an opto-electronical test bench has been developed and it allows controlling the parameters involved in SPPs excitation. Moreover it can be adapted for both reflectance and transmittance analysis. After a preliminary bare gratings characterization, gratings behavior to refractive index changes has been evaluated through different surface functionalization processes, and experimental data have been compared to simulations results.

The work has been organized as follows:

Chapter 1: Surface Plasmon Polaritons. Starting from Maxwell's equations, surface plasmon polaritons are described as surface propagating solutions localized at the interface between a metallic medium and a dielectric one. The basic characteristics of these modes are illustrated: field polarization, propagation length and spatial extension from the interfaces. Because of their non-radiative nature, optical excitation is possible only with proper configurations. Prism coupling and diffraction gratings techniques are introduced and briefly described. The chapter ends with a short review

about SPPs application to biosensors for biological and medical molecules detections and biosensors basic features are also described.

Chapter 2: Materials and Methods. In this chapter the various analyzed gratings and their fabrication methods have been described. The developed optoelectronic bench is illustrated in detail, considering both types of configurations, for reflectance and for transmittance analysis. A test bench characterization has been developed in order to verify set-up errors. A description of the different functionalization processes and of the microfluidic chips fabrication is also reported.

Chapter 3: Theoretical analysis and simulations. In this chapter results of simulations have been described, in order to understand gratings behavior and the parameters range that must be experimentally analyzed. Different gratings have been evaluated through different simulation methods: Wave-Vector Conservation Law for sinusoidal and trapezoidal gratings, the last one have been studied also through Rigorous Coupled-Wave Analysis (RCWA), instead the digital grating has been analyzed through Finite Elements Method (FEM) fully implemented in the commercial software *COMSOL Multiphysics®* version 3.5a.

Chapter 4: Experimental results. In this chapter the experimental results, carried out from tests in laboratory, will be presented. Functionalization protocols have been applied in order to compare bare and functionalized grating behavior and so to verify the capability of the sensor to detect surface refractive index variations. More detailed measurements have been developed for the gold sinusoidal grating and the silver trapezoidal one. The former has been adopted for the detection of two different molecules: avidin and a DNA chain. The latter has been characterized in bare state through an analysis in angles modulation, and then measurements of different functionalization layers have also developed through alkanethiols of increasing length. An analysis of different refractive index of bulk has been also developed using both gratings in order to estimate sensor sensitivity and resolution.

1 Surface Plasmon Polaritons

The first observation of surface plasmons was made in 1902 by Wood [1], who have noted anomalies in the spectrum of light diffracted on a metallic diffraction grating. In 1941 Fano [2] has proven that these anomalies are associated with the excitation of electromagnetic waves on the surface of the diffraction gratings. In 1968 Otto [3] demonstrated that the drop in reflectivity in the attenuated total reflection method is due to the excitation of surface plasmons, and in the same year, Kretschmann and Raether observed excitation of surface plasmons in another configuration based on the same method [4]. The physical explanation of this phenomenon and the connection between Wood's anomalies and surface plasmons polaritons (SPPs) was finally established by Cowan and Arakawa [5]: a plane-wave illuminating the patterned area is diffracted by the periodic structure and it is possible for at least one of the diffracted orders to couple with SPPs modes.

These pioneering works established a convenient method for the excitation and investigation of surface polaritons, before modern nanofabrication technique allowed diffraction gratings realization.

1.1 Plasmon Polaritons theory

Surface Plasmon Polaritons are electromagnetic waves propagating along the interface between two media with opposite refractive index (i.e. a dielectric and a conductor), evanescently confined in the perpendicular direction and arising via the coupling of electromagnetic fields with the conductor plasma electrons.

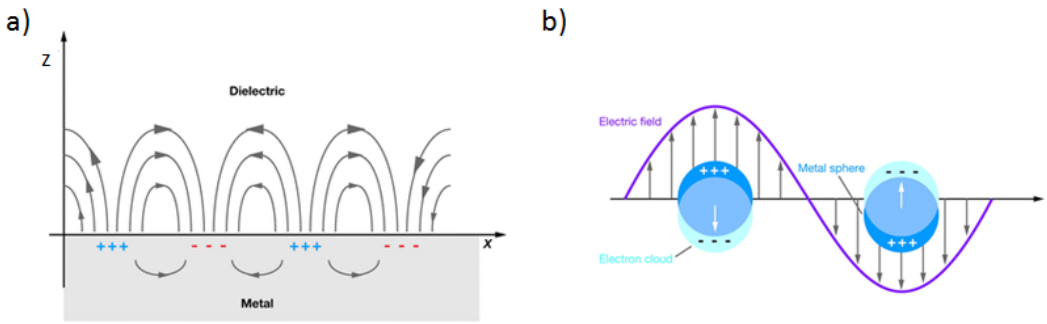

Figure 1.1: Surface plasmon polaritons fields at the metal/dielectric interface

The starting point to understand surface plasmon polaritons is looking for a confined wavelike solution of Maxwell's equations at the interface of two semi-infinite media, with the imposition of the associated boundary conditions. So, in absence of external charge and current, Maxwell's equations are in the following form [6]:

$$\nabla \cdot \mathbf{D} = 0 \tag{1.1}$$

$$\nabla \cdot \mathbf{B} = 0 \tag{1.2}$$

$$\nabla \times \mathbf{E} = -\frac{\partial \mathbf{B}}{\partial t} \tag{1.3}$$

$$\nabla \times \mathbf{H} = \frac{\partial \mathbf{D}}{\partial t} \tag{1.4}$$

where $\mathbf{D}$ is the dielectric displacement, $\mathbf{E}$ the electric field, $\mathbf{H}$ the magnetic field, and $\mathbf{B}$ the magnetic induction or magnetic flux density. These macroscopic fields are related by the following constitutive relations:

$$\mathbf{D} = \varepsilon \mathbf{E} \tag{1.5}$$

$$\mathbf{B} = \mu \mathbf{H} \tag{1.6}$$

where $\varepsilon=\varepsilon_0\varepsilon_r$ and $\mu= \mu_0\mu_r$, ε_r and μ_r are respectively the relative dielectric permittivity and the relative magnetic permeability of the medium, ε_0 and μ_0 are their values in vacuum.

The equations 1.3, 1.4 and 1.6 can be combined to yield

$$\nabla \times \nabla \times \mathbf{E} = -\mu_0 \frac{\partial^2 \mathbf{D}}{\partial t^2} \tag{1.7}$$

Using the identities $\nabla \times \nabla \times \mathbf{E} \equiv \nabla(\nabla \cdot \mathbf{E}) - \nabla^2 \mathbf{E}$ as well as $\nabla \cdot (\varepsilon \mathbf{E}) \equiv \mathbf{E} \cdot \nabla \varepsilon_r + \varepsilon_r \nabla \cdot \mathbf{E}$, 1.7 can be rewritten as:

$$\nabla\left(-\frac{1}{\varepsilon_r}\mathbf{E} \cdot \nabla \varepsilon_r\right) - \nabla^2 \mathbf{E} = -\mu_0 \varepsilon \frac{\partial^2 \mathbf{E}}{\partial t^2} \tag{1.8}$$

In hypothesis of homogeneous media and negligible variation of dielectric profile, 1.8 becomes

$$\nabla^2 \mathbf{E} - \frac{\varepsilon_r}{c^2}\frac{\partial^2 \mathbf{E}}{\partial t^2} = 0 \tag{1.9}$$

This equation has to be solved separately in regions of constant ε.

Assuming a harmonic time dependence $\mathbf{E}(\mathbf{r}, t) = \mathbf{E}(\mathbf{r})e^{-i\omega t}$ of the electric field, 1.9 becomes

$$\nabla^2 \mathbf{E} + k_0^2 \varepsilon_r \mathbf{E} = 0 \tag{1.10a}$$

and the same analysis can be done for the magnetic field, obtaining

$$\nabla^2 \mathbf{H} + k_0^2 \varepsilon_r \mathbf{H} = 0 \tag{1.10b}$$

known as Helmholtz equations, where $k_0=\omega/c$ is the wave number of the propagating wave in vacuum.

In the case of two semi-infinite media, ε depends only on one spatial coordinate, so it is a one-dimensional problem. Considering the Cartesian system in fig. 1.1a, the wave propagates along the x-direction, and the plane z=0 coincides with the interface sustaining the propagating wave, which can be described as:

$$\mathbf{H}(x,y,z) = \mathbf{H}(z)e^{i\beta x} \tag{1.11a}$$

$$\mathbf{E}(x,y,z) = \mathbf{E}(z)e^{i\beta x} \tag{1.11b}$$

where $\beta=k_x$ is the *propagation constant* of traveling wave and corresponds to the component of the wave vector in the direction of propagation. Inserting these expressions into 1.10a and 1.10b we obtain:

$$\frac{\partial^2\mathbf{H}(z)}{\partial z^2}+(\varepsilon_r k_0^2 - k_x^2)\mathbf{H}(z) = 0 \tag{1.12a}$$

$$\frac{\partial^2\mathbf{E}(z)}{\partial z^2}+(\varepsilon_r k_0^2 - k_x^2)\mathbf{E}(z) = 0 \tag{1.12b}$$

These equations are the starting point for the general analysis of guided electromagnetic modes in waveguides. Solving these equations, two sets of self-consistent solutions with different polarization properties of the propagating waves can be observed. The first set are the transverse magnetic (TM or p) modes, where only the field components E_x, E_z and H_y are nonzero, and the second set the transverse electric (TE or s) modes, with only H_x, H_z and E_y being nonzero.

If we consider a system of two media like the one depicted in fig. 1.1a, where the upper part (z > 0) is a dielectric medium with a dielectric constant ($\varepsilon_d = \varepsilon_d' + i\varepsilon_d''$) and the lower part is a conductive medium described by a typical metallic dielectric constant ($\varepsilon_m = \varepsilon_m' + i\varepsilon_m''$), whose real part must be negative, the boundary conditions at the interface between the two media are:

$$\mathbf{n}\cdot(\mathbf{D_d} - \mathbf{D_m}) = 0 \tag{1.13}$$

$$\mathbf{n}\,\mathrm{x}\,(\mathbf{E_d} - \mathbf{E_m}) = 0 \tag{1.14}$$

$$\mathbf{n}\cdot(\mathbf{B_d} - \mathbf{B_m}) = 0 \tag{1.15}$$

$$\mathbf{n}\,\mathrm{x}\,(\mathbf{H_d} - \mathbf{H_m}) = 0 \tag{1.16}$$

where **n** is the normal to the surface.

These boundary conditions can be considered to solve equation 1.9, and we obtain:

$$\mathrm{E}_{\mathrm{d}}^{\parallel} = \mathrm{E}_{\mathrm{m}}^{\parallel} \tag{1.17}$$

$$\varepsilon_{\mathrm{d}}\mathrm{E}_{\mathrm{d}}^{\perp} = \varepsilon_{\mathrm{m}}\mathrm{E}_{\mathrm{m}}^{\perp} \tag{1.18}$$

$$\mathrm{H}_{\mathrm{d}}^{\parallel} = \mathrm{H}_{\mathrm{m}}^{\parallel} \tag{1.19}$$

$$\mu_{\mathrm{d}}\mathrm{H}_{\mathrm{d}}^{\perp} = \mu_{\mathrm{m}}\mathrm{H}_{\mathrm{m}}^{\perp} \tag{1.20}$$

We first consider a TM plane wave which propagates in the positive x-direction. Since we are looking for localized EM-waves, the magnetic field should have the following form:

$$z > 0 \qquad \mathbf{H}(\mathrm{x},\mathrm{z},\mathrm{t}) = (0, \mathrm{H}_{\mathrm{y,d}}, 0)e^{ik_{x,d}x - k_{z,d}z}e^{-i\omega_d t} \tag{1.21a}$$

$$z < 0 \qquad \mathbf{H}(\mathrm{x},\mathrm{z},\mathrm{t}) = (0, \mathrm{H}_{\mathrm{y,m}}, 0)e^{ik_{x,m}x + k_{z,m}z}e^{-i\omega_m t} \tag{1.21b}$$

In order to have a solution localized at the metal/dielectric interface (z=0) we have to assume $k_{z,j\ (j=d,m)}$ purely imaginary and so the plus sign is considered for z > 0 and the minus sign for z < 0. Since equation 1.16 must be satisfied for every (x,t) at z=0, it follows that $\omega_d=\omega_m=\omega$, $H_{y,d}=H_{y,m}=H_y$ *and* $k_{x,d}=k_{x,m}=k_x$, and equations 1.21a and 1.21b can be written as:

$$z > 0 \qquad \mathbf{H}(\mathrm{x},\mathrm{z},\mathrm{t}) = (0, \mathrm{H}_{\mathrm{y}}, 0)e^{ik_x x - k_{z,d}z}e^{-i\omega t} \tag{1.22a}$$

$$z < 0 \qquad \mathbf{H}(\mathrm{x},\mathrm{z},\mathrm{t}) = (0, \mathrm{H}_{\mathrm{y}}, 0)e^{ik_x x + k_{z,m}z}e^{-i\omega t} \tag{1.22b}$$

Starting from Maxwell's equations we can find also the electric field expressions:

$$z > 0 \qquad \mathbf{E}(\mathrm{x},\mathrm{z},\mathrm{t}) = (\frac{\mathrm{H_y}k_{z,d}}{\omega\varepsilon_d}, 0, \frac{\mathrm{H_y}ik_x}{\omega\varepsilon_d})e^{ik_x x - k_{z,d}z}e^{-i\omega t} \tag{1.22c}$$

$$z < 0 \qquad \mathbf{E}(\mathrm{x},\mathrm{z},\mathrm{t}) = (-\frac{\mathrm{H_y}k_{z,m}}{\omega\varepsilon_m}, 0, \frac{\mathrm{H_y}ik_x}{\omega\varepsilon_m})e^{ik_x x - k_{z,m}z}e^{-i\omega t} \tag{1.22d}$$

The boundary condition expressed in equation 1.14 imposes that:

$$\frac{k_{z,d}}{\varepsilon_d} + \frac{k_{z,m}}{\varepsilon_m} = 0 \tag{1.23}$$

If we assume that the dielectric function of the metal $\varepsilon_m(\omega)$ is real, it follows, since $k_{z,d}$ and $k_{z,m}$ must be real and positive, that ε_m must be negative for this surface electromagnetic waves to exist. Using the last expression and the definition of $k_{z,j}$ (j=d,m) obtained replacing the solution into the wave equation:

$$k_{z,j} = \sqrt{k_x^2 - \varepsilon_j\left(\frac{\omega}{c}\right)^2} \tag{1.24}$$

we obtain the explicit expression of the wavenumber of the surface plasmon polaritons as a function of frequency ω:

$$k_x = \frac{\omega}{c}\sqrt{\frac{\varepsilon_d\varepsilon_m}{\varepsilon_d+\varepsilon_m}} \tag{1.25}$$

Equation 1.25 coincides with the dispersion relation β of SPPs propagating at the interface between the two half spaces. If the structure is lossless ($\varepsilon_m'' = \varepsilon_d'' = 0$), equation 1.25 represents a guided mode only if ε_m' and ε_d' are of opposite signs and $\varepsilon_m' < -\varepsilon_d'$ [7].

We now consider a transverse-electric (TE) plane wave in the same previous system in order to find the solution of Maxwell's equations localized at the interface between the two media. The electric and the magnetic fields are:

$$z > 0 \qquad \mathbf{E}(\mathrm{x},\mathrm{z},\mathrm{t}) = (0, \mathrm{E_y}, 0)e^{ik_x x - k_{z,d} z} e^{-i\omega t} \tag{1.26a}$$

$$z < 0 \qquad \mathbf{E}(\mathrm{x},\mathrm{z},\mathrm{t}) = (0, \mathrm{E_y}, 0)e^{ik_x x + k_{z,m} z} e^{-i\omega t} \tag{1.26b}$$

$$z > 0 \qquad \mathbf{H}(\mathrm{x},\mathrm{z},\mathrm{t}) = (-\frac{ic\mathrm{E_y}k_{z,d}}{\omega}, 0, \frac{c\mathrm{E_y}k_x}{\omega})e^{ik_x x - k_{z,d} z} e^{-i\omega t} \tag{1.26c}$$

$$z < 0 \qquad \mathbf{H}(\mathrm{x},\mathrm{z},\mathrm{t}) = (\frac{ic\mathrm{E_y}k_{z,m}}{\omega}, 0, \frac{c\mathrm{E_y}k_x}{\omega})e^{ik_x x + k_{z,m} z} e^{-i\omega t} \tag{1.26d}$$

The continuity conditions of the tangential components of the fields at the interface yields:

$$\left(k_{z,d} + k_{z,m}\right)\mathrm{E}_y = 0 \tag{1.27}$$

Since confinement to the surface requires Re[$k_{z,d}$]>0 and Re[$k_{z,m}$]>0, this condition is fulfilled if E_y=0. Thus a TE mode cannot propagate along the planar dielectric-metal interface. Surface plasmon polaritons only exist for TM polarization.

Spatial Extension of the SPPs Fields

Surface plasmons polaritons are surface waves localized at the dielectric/metal interface. The field amplitude decreases exponentially as exp ($-|k_{z,j}z|$), normal to the surface. The value of the skin depth at which the field falls to 1/e is:

$$d_z = \frac{1}{|k_{z,j}|} \tag{1.28}$$

From equations 1.24 and 1.25, we can obtain the skin depth in the two media:

$$z > 0 \qquad d_z = \frac{\lambda}{2\pi}\sqrt{-\frac{\varepsilon_d + \varepsilon\prime_m}{\varepsilon_d^2}} \tag{1.29}$$

$$z < 0 \qquad d_z = \frac{\lambda}{2\pi}\sqrt{-\frac{\varepsilon_d + \varepsilon\prime_m}{\varepsilon\prime_m^2}} \tag{1.30}$$

If we consider SPPs at interface between a noble metal (gold or silver) and a dielectric (air or water), for λ=633 nm, we obtain the skin depth values reported in the following table.

Metal	ε_m	d_z **(z>0,** ε_{air}**=1)**	d_z **(z<0,** ε_{air}**=1)**	d_z **(z>0,** ε_{water}**=1.78)**	d_z **(z<0,** ε_{water}**=1.78)**
Au	-12.1+*i*1.3	335.6 nm	27.8 nm	180.9 nm	26.8 nm
Ag	-17+*i*0.7	403.0 nm	23.7 nm	220.8 nm	23.1 nm

Table 1.1: Value of dielectric permittivity and skin depth for gold and silver considering both air and water.

Propagation length of SPPs

Since the dielectric function of the metal is complex, the wave vector k_x of surface wave is complex. SPPs wavevector is given by:

$$k_x = \beta = \frac{\omega}{c}\sqrt{\frac{\varepsilon_d \varepsilon'_m}{\varepsilon_d + \varepsilon'_m}} + i\frac{\omega}{c}\sqrt{\left(\frac{\varepsilon_d \varepsilon'_m}{\varepsilon_d + \varepsilon'_m}\right)^3}\frac{\varepsilon''_m}{2\varepsilon'^2_m} \tag{1.31a}$$

where the real and the imaginary parts of SPPs momentum are:

$$Re(k_x) = \frac{\omega}{c}\sqrt{\frac{\varepsilon_d \varepsilon'_m}{\varepsilon_d + \varepsilon'_m}} \tag{1.31b}$$

$$Im(k_x) = \frac{\omega}{c}\sqrt{\left(\frac{\varepsilon_d \varepsilon'_m}{\varepsilon_d + \varepsilon'_m}\right)^3}\frac{\varepsilon''_m}{2\varepsilon'^2_m} \tag{1.31c}$$

where $\varepsilon_d > 0$ (dielectric), ε'_m (< 0) and ε''_m are respectively the real and imaginary parts of the permettivity ε_m in the metallic medium, λ is the considered wavelength. It is worth noting that $Im(k_x) \propto \varepsilon''_m$, i.e. SPPs dissipation is strictly related to the adsorption contributions inside the metal. The surface plasmon decay in *x*-direction can be evaluated from $Im(k_x)$ because the intensity decreased as exp $(-2 \cdot Im(k_x))$ and the length L at which the intensity decreases to $1/e$ is

$$L = \frac{1}{2Im(k_x)} \tag{1.32}$$

If we consider SPPs at interface between a noble metal (gold or silver) and a dielectric (air or water), for λ=633 nm, we obtain the propagation length values reported in table 1.2. In Figure 1.2 dielectric permettivity real ε'_m and imaginary ε''_m parts and the propagation length are showed in the range 200 − 1500 nm for the most common metals. Most of metals exhibit a common trend in the VIS-nearIR spectral range: ε'_m

decreases for increasing wavelength and is negative in the VIS-IR range, while ε''_m increases with wavelength.

Metal	ε_m	L (ε_{air}=1)	L (ε_{water}=1.78)
Au	-12.1+*i*1.3	10.0 µm	3.8 µm
Ag	-17+*i*0.7	38.0 µm	14.8 µm

Table 1.2: Value of dielectric permittivity and SPPs propagation length for gold and silver considering both air and water.

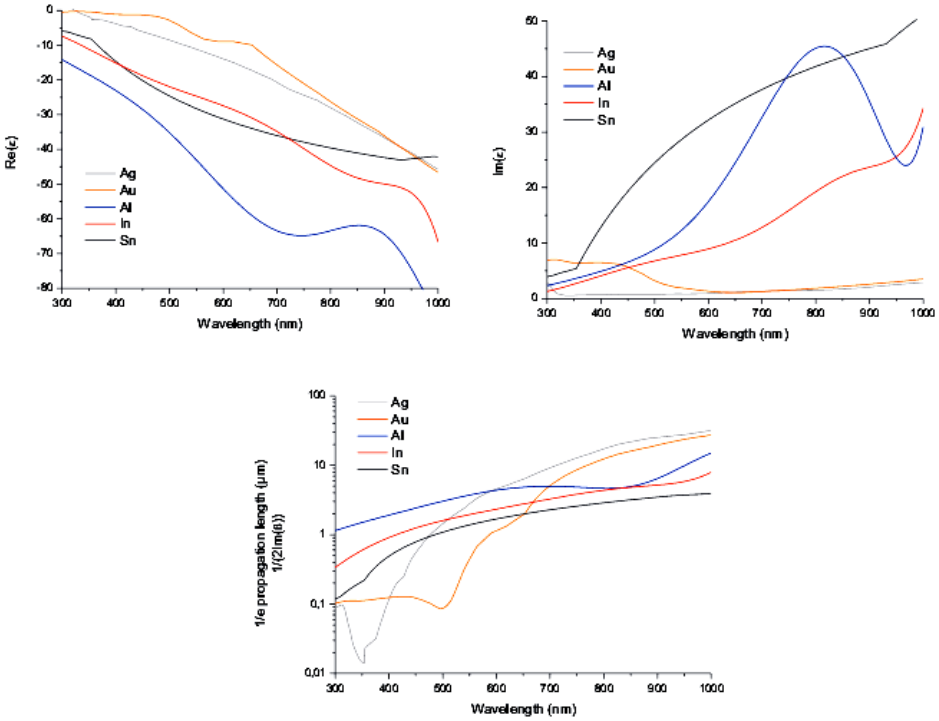

Figure 1.2: Real (left) and imaginary (right) part of the dielectric constant for some common metals. Bottom: propagation lengths

The dielectric function in metals

Over a wide frequency range, the optical properties of metals can be explained by a *plasma model*, where a gas of free electrons of number density *n* moves against a fixed background of positive ion cores. For alkali metals, this range extends up to the ultraviolet, while for noble metals interband transitions occur at visible frequencies,

limiting the validity of this approach. In the plasma model, details of the lattice potential and electron-electron interactions are not taken into account, but we can assume that some aspects of the band structure are incorporates into the effective optical mass *m* of the electron. The electrons oscillate in response to the applied electromagnetic field, and their motion is damped via collisions occurring with a characteristic collision frequency $\gamma = 1/\tau$. τ is known as the *relaxation time* of the free electron gas, which is typically on the order of 10^{-14} s at room temperature, corresponding to γ = 100 THz.

In the presence of an external electric field, the motion of an electron of the plasma sea is the solution of:

$$m\ddot{\boldsymbol{x}} = -m\gamma\dot{\boldsymbol{x}} - e\mathbf{E} \tag{1.33}$$

where *e* is the electron charge.

If we assume a harmonic time dependence of the electric field E, a particular solution of equation 1.33 describing the oscillation of the electron is $\mathbf{x}(t)=\mathbf{x}_0 e^{-i\omega t}$. Replacing this solution into the equation of motion we obtain:

$$\boldsymbol{x}(t) = \frac{e}{m(\omega^2+i\gamma\omega)}\mathbf{E}(t) \tag{1.34}$$

The displacement of electrons gives rise to a macroscopic polarization:

$$\mathbf{P} = -en\boldsymbol{x} = -\frac{ne^2}{m(\omega^2+i\gamma\omega)}\,\mathbf{E} \tag{1.35}$$

where *n* is the free electron density. Since $P=\varepsilon_0(\varepsilon_r-1)E$, the explicit form of the relative dielectric function of metals in plasma approximation can be obtained:

$$\varepsilon(\omega) = 1 - \frac{\omega_p^2}{\omega^2+i\gamma\omega} \tag{1.36}$$

where $\omega_p = \frac{ne^2}{\epsilon_0 m}$ is the *plasma frequency* of free electron gas. The real and the imaginary part of this complex dielectric function $\varepsilon(\omega) = \varepsilon'(\omega) + i\varepsilon''(\omega)$ are given by

$$\varepsilon'(\omega) = 1 - \frac{\omega_p^2\tau^2}{1+\omega^2\tau^2} \tag{1.37a}$$

$$\varepsilon''(\omega) = \frac{\omega_p^2\tau}{\omega(1+\omega^2\tau^2)} \tag{1.37b}$$

For $\omega >> 1/\tau$ imaginary part is negligible and dielectric function reduces to:

$$\varepsilon(\omega) = 1 - \frac{\omega_p^2}{\omega^2} \tag{1.38}$$

Substituting this expression into SPPs momentum relation and rearranging terms, the SPPs dispersion law can be obtained (fig. 1.3). Maxwell's theory shows that electromagnetic surface waves can propagate along a metallic surface or on metallic films with a broad spectrum of eigen frequencies from *to* ω=0 up to $\omega=\omega_p/\sqrt{2}$ depending

on the wave vector ***k***. Their dispersion relation ω(**k**) lies right of the light line which means that the surface plasmons have a longer wave vector than light waves of the same energy $\hbar\omega$, propagating along the surface [8]. As fig. 1.3 shows there is no intersection between SPPs dispersion curve and light line, so surface polaritons are non-radiative waves and they cannot be excited directly by incident light waves that propagates in air. For k→ +∞ dispersion curve asymptotically approaches the frequency $\omega = \frac{\omega_p}{\sqrt{1+\varepsilon_d}}$.

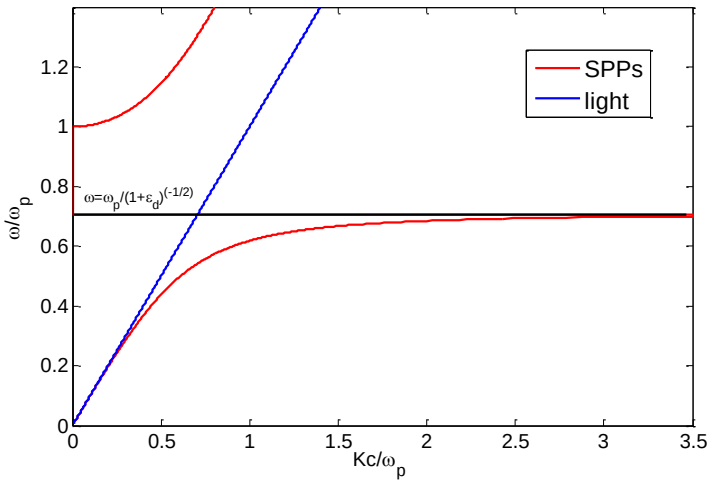

Figure 1.3: The dispersion relation of the free electron gas.

1.2 Excitation of Surface Plasmon Polaritons

A light wave can couple to a surface plasmon at a metal-dielectric interface if the component of light wavevector that is parallel to the interface matches the propagation constant of the surface plasmon. As the propagation constant of a surface plasmon at a metal-dielectric interface is larger than the wavenumber of the light wave in the dielectric, surface plasmons cannot be excited directly by light incident onto a smooth metal surface. The wavevector of light can be increased to match that of the surface plasmon by the attenuated total reflection (ATR) or diffraction phenomena. This enhancement and subsequently the coupling between light and a surface plasmon are performed in a coupling device (coupler). The most common couplers used in SPR sensors include a prism coupler and a grating coupler [7].

1.2.1 Prism coupler

Prism couplers represent the most frequently used method for optical excitation of surface plasmons. In the Kretschmann configuration of the attenuated total reflection (ATR) method (fig. 1.4), a light wave passes through a high refractive index prism and is totally reflected at the base of the prism, generating an evanescent wave penetrating a thin metal film.

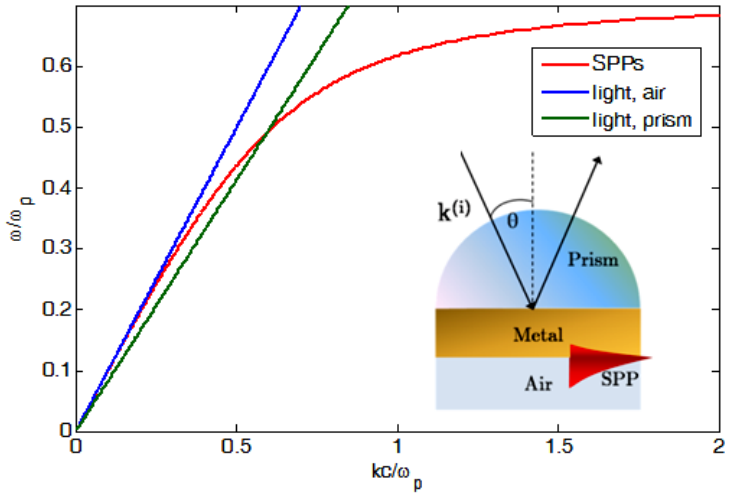

Figure 1.4: Dispersion law in prism-coupling configuration. The interception between red and green curve represents the momentum matching condition. In the inset graph: Kretschmann's configuration.

The evanescent wave propagates along the interface with the propagation constant, which can be adjusted to match that of the surface plasmon by controlling the angle of incidence. Thus, the matching condition is

$$Re\{k_{SPPs}\} = \frac{2\pi}{\lambda} n_p \sin\vartheta \tag{1.39}$$

where ϑ is the light incident angle, λ is the incident light wavelength and n_p is the refractive index of the prism that must be higher than the dielectric one.

For thick metal films (or surfaces of bulk metal), for which the Kretschmann's configuration cannot be used, SPPs can be excited in the Otto configuration (figure 1.5), in which a thin dielectric layer (usually air) is introduced between the prism and the metal layer. Here, the prism where total internal reflection occurs is placed close to the metal surface, so that photon tunneling occurs through the air gap between the prism and the surface. The resonant conditions are analogous to those in the Kretschmann's configuration. This configuration is also preferable when direct contact with the metal surface is undesirable, e.g. for studying the surface quality.

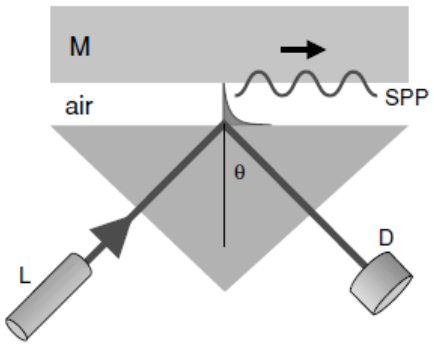

Figure 1.5: Otto's configuration

1.2.2 Grating coupler

An alternative solution in order to optically excite surface plasmons polaritons is based on the diffraction of light incident on a metallic grating. Incident light momentum $k^{(in)}$ couples to grating crystal momentum $\boldsymbol{G}$, whose modulus is $G = \frac{2\pi}{\Lambda}$, where Λ is the grating period. The momentum of a specific diffracted order is [8]:

$$\boldsymbol{k}^m = \boldsymbol{k}^{(in)} + m\boldsymbol{G} \tag{1.40}$$

where m is the diffraction order. SPPs excitation takes place when the on-plane momentum component of a specific diffracted order equals SPPs momentum $\boldsymbol{k}_{SPPs}$, i.e.

$$\boldsymbol{k}_{SPPs} = \boldsymbol{k}_{||}^{(in)} + m\boldsymbol{G} \tag{1.41}$$

In classical mounting, where the scattering plane is parallel to the grating symmetry plane (fig. 1.6), equation 1.41 can be written as

$$Re\{k_{SPPs}\} = \frac{2\pi}{\lambda} n_d \sin\vartheta + m\frac{2\pi}{\Lambda} = k_x^m \tag{1.42}$$

where ϑ is the light incident angle, λ is the incident light wavelength and n_d is the refractive index of dielectric over the grating surface [9].

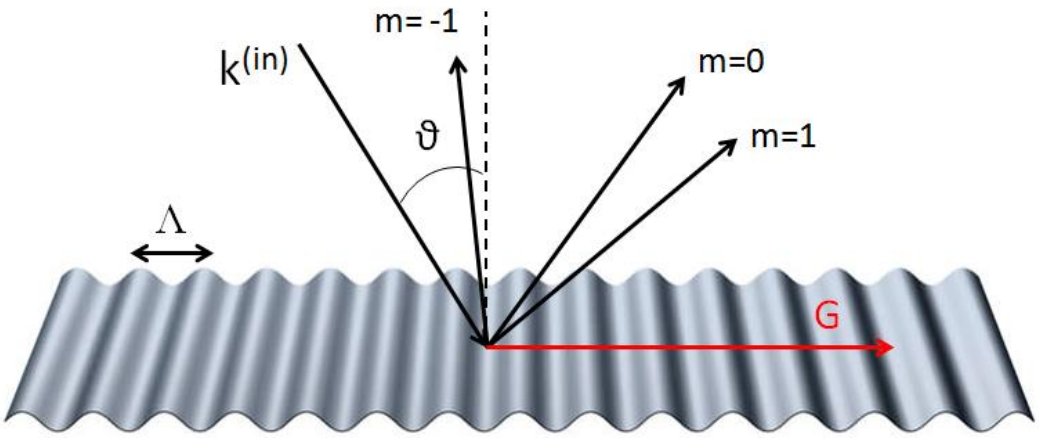

Figure 1.6: Grating classical mounting.

1.3 Sensors based on Surface Plasmon Resonance (SPR) effect

In principle, SPR sensors measure refractive index changes that occur at the surface of a metal film supporting propagating surface plasmons [10]. A surface plasmon excited by a light wave propagates along the metal film, and its evanescent field probes the medium (sample) in contact with the metal film. A change in the refractive index of the dielectric gives rise to a change in the propagation constant of the surface plasmons, and so it alters the characteristics of the light wave coupled to the surface plasmon, such as the coupling incident angle and wavelength, coupling intensity and phase (figure 1.7). On the basis of which characteristic of the light modulated by a surface plasmon is measured, SPR sensors are classified as sensors with angular, wavelength, intensity or phase modulation.

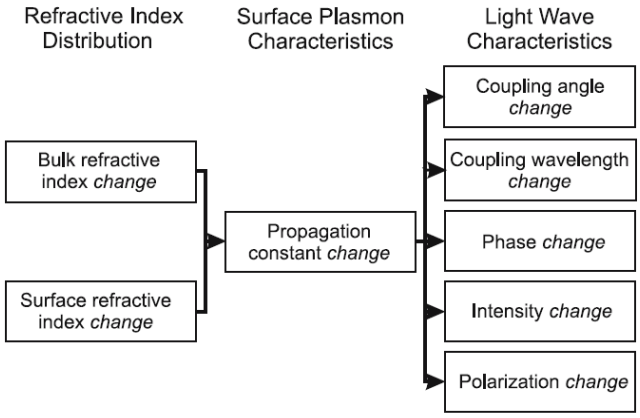

Figure 1.7: concept of surface plasmon resonance sensor

In SPR sensors with angular modulation, a monochromatic light wave is used to excite SPPs and the strength of coupling between the incident wave and surface plasmons is observed at multiple angles of incidence: SPPs excitation is observed as a dip in the angular spectrum of reflected light. The angle of incidence yielding the strongest coupling (reflectivity minimum) is measured and used as sensor output [11].

In SPR sensors with wavelength modulation, a surface plasmon is excited by a collimated light wave containing multiple wavelengths, typically a beam of polychromatic light. The excitation of surface plasmons is observed as a dip in the wavelength spectrum of reflected light. The wavelength yielding the strongest coupling is measured and used as a sensor output [12], [13].

In SPR sensors with intensity modulation the strength of the coupling between the light wave and surface plasmons is measured at a single angle of incidence and wavelength and the intensity of light serves as sensor output [14]. In phase modulation SPR, the shift in phase of reflected light is measured at a single angle of incidence and wavelength of the light wave and used as sensor output [15].

SPR affinity biosensors consists of:

- a *biorecognition element*: it is a probe able to interact selectively with a specific analyte and it is immobilized over the sensor active surface through a functionalization process;
- a transducer: a detector that translates the binding event into an output signal.

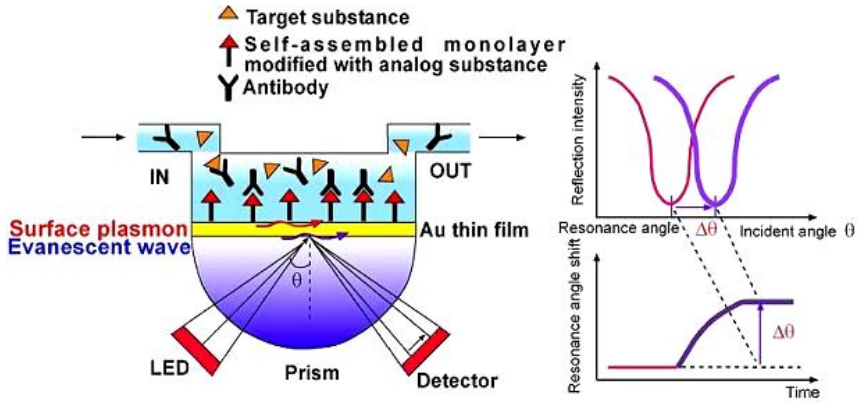

Figure 1.8: Example of SPR biosensor. The resonance incident angle variation is the sensing parameter.

The core of the transducer is the optical platform on which a surface plasmon is optically excited and propagates, e.g. a modulated metallic grating or a flat metallic layer in Kretschmann's configuration. Analyte molecules in a liquid sample in contact with the SPR sensor bind to the biorecognition elements, producing an increase in the refractive index at the sensor surface which is optically measured by SPPs excitation and translated into an output signal (fig. 1.8).

The sensor response Y to a given value X of the molecules that is measured can be predicted by the sensor transfer function T , $Y = T(X)$ determined from a theoretical model of sensor response or from a sensor calibration.

1.3.1 Performance

The main performance characteristics of SPR (bio)sensors include sensitivity, linearity, resolution, accuracy, reproducibility, dynamic range, and limit of detection [7].

Sensitivity

Sensors sensitivity *S* is the ratio of the change in sensor output *Y* to the change of the quantity to be measured, such as concentration analyte:

$$S = \frac{\partial Y}{\partial X} \tag{2.1}$$

The sensitivity of an SPR sensor to a refractive index S_{RI} can be expressed as a product of two terms

$$S_{RI} = \frac{\partial Y}{\partial n_{ef}} \frac{\partial n_{ef}}{\partial n_d} \tag{2.2}$$

where the first term describes the sensitivity of sensor output to the effective refractive index of a surface plasmon and depends on the method of excitation of surface plasmons and the used modulation approach, the second term describes the sensitivity of the effective index of a surface plasmon to refractive index and is *independent* of the modulation method and the method of excitation [9].

Resolution

The resolution of a SPR biosensor is defined as the smallest change in the bulk refractive index that produces a detectable change in the sensor output and it is strictly related to the level of uncertainty of the sensor output: the sensor noise. The refractive index resolution σ_n is typically expressed in terms of the standard deviation of noise of the sensor output σ_Y translated to the refractive index of bulk medium:

$$\sigma_n = \frac{\sigma_Y}{S_{RI}} \tag{2.3}$$

where S_{RI} is the bulk refractive index sensitivity.

SPR sensors of all the modulation approaches need to measure the intensity of the light wave coupled to a surface plasmon to determine the sensor output. Therefore, their resolution is limited by the noise in the intensity of the detected light. Dominant

sources of noise are the fluctuations in the light intensity emitted by the light source, shot noise associated with photon statistics, and noise in conversion of the light intensity into electric signal by the detector. Noise in the intensity of light emitted by the light source is proportional to the intensity and its standard deviation σ_L can be given as $\sigma_L = \sigma_{rL} I$ where σ_{rL} is relative standard deviation and I is the measured light intensity.

Shot noise is associated with random arrival of photons on a detector and corresponding random production of photoelectrons. Photon flux usually obeys Poisson statistics and produces a shot noise σ_S is directly proportional to the square root of the detected light intensity: $\sigma_S = \sigma_{rS}\sqrt{I}$ where σ_{rS} is relative standard deviation. Detector noise consists of several contributions that originate mostly in temperature noise and its standard deviation σ_D is independent on the light intensity.

The resulting noise of a measured light intensity σ_I is a statistical superposition of all the noise components and is expressed as:

$$\sigma_I(I) = \sqrt{I^2\sigma_{rL}^2 + I\sigma_{rS}^2 + \sigma_D^2} \tag{2.4}$$

To reduce the noise, light intensity is averaged: time averaging involves the average of time series of intensity from the same detector, spatial averaging instead the average of the output of multiple detectors. As in the time domain all the noise contributions behave independently, the time averaging of *N* spectra reduces the total noise as follows:

$$\sigma_I^N = \frac{\sigma_I}{\sqrt{N}} \tag{2.5}$$

The noise in the light intensity is translated to sensor output noise by a data processing algorithm used to generate the sensor output. Although various methods for processing data from spectroscopic SPR sensors have been developed (centroid method [16], polynomial fitting [17], and optimal linear data analysis [18]), the noise in angular or wavelength spectra was found to transform to the noise in the sensor output in a similar fashion.

Centroid method uses a simple algorithm which finds the geometric center of the SPR dip under a certain threshold. The centroid position x_c is calculated as follows using a weigth centroid algorithm [19]:

$$x_c = \frac{\sum_i x_i (I_T - I_i)^2}{\sum_i (I_T - I_i)^2} \tag{2.6}$$

where x_i is the spectral position of the contributing intensity I_i and I_T denotes the threshold value. If the noise of each intensity value can be detected and treated as

independent, the resulting standard deviation of calculated dip position σ_c can be calculated from eq. 2.6:

$$\sigma_c^2 = \sum_i \left(\frac{\partial x_c}{\partial I_i}\right)^2 \sigma_i^2 \tag{2.7}$$

Piliarik and Homola [7] investigated the propagation of noise through the centroid data processing algorithm and demonstrated that the noise of the centroid method can be expressed as:

$$\sigma_n = K \frac{1}{\sqrt{N}} \frac{\sigma_T}{d} \frac{w}{S_{RI}} \tag{2.8}$$

where *N* is the number of intensities used for the calculation of the centroid, σ_T is the total intensity noise at the threshold, *d* is the difference of intensities at the SPR dip minimum and at the threshold, *w* is the width of the dip, S_{RI} is the bulk refractive index sensitivity of the sensor, and *K* is a factor depending on the relative contributions of the sources of noise.

This results shows that resolution strictly depends on resonance profile and, as expected, output noise. From eq. 2.8 resolution is proportional to output noise σ and resonance width *w*, whereas it decreases with increasing sensor sensitivity S_{RI} and depth of resonance dip *d*. The ratio *w*/ S_{RI} depends only weakly on the choice of coupler and modulation and therefore has only a minor effect on the sensor resolution. As a consequence of eq. 2.8, it is worth noting that resonance-dip width *w* should be minimized while depth *d* should be maximized in order to optimize the refractive index resolution σ_n.

Limit of detection

The Limit Of Detection (LOD) is the concentration of analyte c_L derived from the smallest measure Y_L that can be detected with reasonable certainty. The value is given by

$$Y_{LOD} = Y_b + m\,\sigma_b \tag{2.9}$$

where Y_b is an estimation of blank (sample with no analyte) sample output, σ_b is the standard deviation of the blank measurements, *m* is a numerical factor chosen according to the desired confidence level (typically 2-3) [20]. Since the concentration of analyte in blank sample is zero, the LOD concentration c_L is given by

$$c_L = \frac{m\sigma_b}{S_c} \tag{2.10}$$

Linearity

Sensor linearity defines the extent to which the relationship between the molecule concentration and the sensor output is linear over the working range. Linearity is usually specified in terms of the maximum deviation from a linear transfer function over the dynamic range. Sensors with linear transfer function are desirable as they require fewer calibration points to produce an accurate sensor calibration. However, response of SPR biosensors is usually a non-linear function of the analyte concentration and therefore calibration is important.

Accuracy

The accuracy is the ability of a measurement to match the real value of the quantity being measured:

$$X_{measured} = X_{true} + e \tag{2.11}$$

where *e* is the measurement error due to random errors (not eliminable) and systematic errors (eliminable via calibration).

1.3.2 Biorecognition elements and applications for the detection of chemical and biological molecules

In SPR affinity biosensors, one of the interacting molecules (biorecognition element or target molecule) is immobilized on the solid surface of the SPR sensor and the other is contained in a liquid sample. Which of the molecules is immobilized depends on the used detection format: in direct, sandwich, and competitive detection formats, the molecule that needs to be immobilized is a biorecognition element; in the inhibition detection format, the immobilized molecule is the target molecule or its derivative. The choice of appropriate biorecognition elements and immobilization method is of critical importance with direct impact on key performance characteristics of the sensor [7]. The format of detection is chosen on the basis of the size of target analyte molecules, binding characteristics of available biomolecular recognition element, range of concentrations of analyte to be measured.

The most used detection modes are:

- direct detection: the biorecognition element is immobilized on the sensor surface. Analyte in solution binds to the antibody, producing a refractive index change detected by the sensor. This mode is usually preferred in applications where direct binding of analyte of concentrations of interest produces a sufficient response
- sandwich detection: the sensor surface with captured analyte is incubated with a second antibody. The specificity and the limit of detection can be improved by using the sandwich detection format.
- competitive detection: the sensing surface is coated with an antibody interacting with the analyte (generally small, molecular weight < 5000); when a conjugated analyte is added to the sample, the analyte and its conjugated analogue compete for a limited number of binding sites on the surface. The binding response is inversely proportional to the analyte concentration
- inhibition detection: a fixed concentration of an antibody with affinity to analyte is mixed with a sample containing an unknown concentration of analyte. This mixture is injected in the flow cell of the SPR sensor and passed over a sensor surface to which analyte or its analogue is immobilized. Noncomplex antibodies are measured as they bind to the analyte molecules immobilized on the sensor surface. The binding response is inversely proportional to the concentration of analyte.

Various types of biorecognition elements and immobilization methods are available to allow the SPR sensing platforms to be tailored for specific detection of chemical and biological substances. Proteins (e.g., antibodies) and peptides are most frequently immobilized via covalent bonds formed between amino groups of the protein and activated carboxyls on a self assembled monolayer of alkanethiolates or within a dextran matrix. Oligonucleotides can be efficiently immobilized via interaction between avidin or streptavidin immobilized on the sensing surface and biotinylated oligonucleotide. Small molecules are usually conjugated with a larger protein, like bovine serum albumin-BSA, which is then covalently immobilized on the sensor surface. High-throughput SPR sensors demand immobilization methods capable of accurate spatially controlled delivery of different biorecognition elements to different areas of the sensing surface. This can be achieved by combining the streptavidin-coated surface with a spatially controlled delivery of biotinylated biorecognition elements by microspotting.

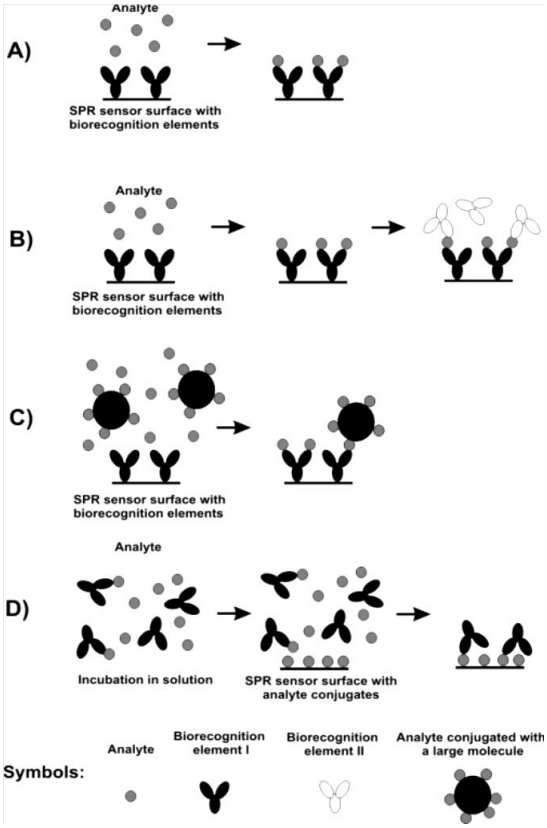

Figure 1.9: Main detection formats used in SPR biosensors: A) direct detection; B) sandwich detection format; C) competitive detection format; D) inhibition detection format.

SPR biosensors have been applied in numerous important fields including medical diagnostics, environmental monitoring, and food safety and security.

Concerning the medical area, SPR biosensors have been demonstrated to hold promise for the detection of analytes related to medical diagnostics such as cancer markers [21], allergy markers [22], heart attack markers [23], antibodies [24], drugs [25], and hormones [26].

Also SPR biosensor applications in food analysis continues to increase, as the number of publications on SPR biosensors for the detection of analytes related to food quality and safety demonstrates [27] [28] [29]. The targeted analytes include pathogens, toxins, drug residues, vitamins, hormones, antibodies, chemical contaminants, allergens, and proteins.

Some examples of commercial devices exploiting direct and sandwich detection are reported in the table 1.3.

SPR technology has been also applied for the environmental monitoring that includes in particular pesticides [30], aromatic hydrocarbons, heavy metals [31], phenols and dioxins [32]. Some commercial SPR sensors for environmental monitoring are reported in table 1.4 [7].

Analyte	Sensor System	LOD	Detection Format
Escherichia C. O157:H7	Multiskop	10^4 cells/mL	direct
	Spreeta	10^6 cells/mL	direct
	SR 7000	10^3 cfu/mL	sandwich
	Biacore 2000	25 cfu/mL	direct
Salmonellae	Biacore 3000	10^3 cfu/mL	sandwich
	Multiskop	10^2 cfu/mL	direct
	Plasmonic	10^3 cells/mL	sandwich
	Biacore 2000	23 cfu/mL	direct
Vibrio Cholearae O1	Multiskop	4 x 10^3 cfu/mL	direct
Staphylococcal Ent.tox.	Biacore X	1 ng/mL	direct
	Spreeta	5.6 ng/mL	direct
		0.6 ng/mL	sandwich
	Biacore 1000	2.5 ng/mL	sandwich
B-casein	Biacore 3000	85 ng/mL	sandwich
IgG	Biacore Q	16.8 ng/mL	direct
Lactoferrin	Biacore Q	1.1 ng/mL	direct
Lactoperoxidase	Biacore Q	75 ng/mL	direct
Prostate Cancer Marker	Ibis II	0.15 ng/mL	sandwich
	Biacore 2000	10 ng/mL	direct
		1 ng/mL	sandwich
Interleukin-8	Biacore X	0.02 ng/mL	sandwich
Carcinoembrionic Antig.	Autolab Springle	0.5 ng/mL	direct
anti-Insulin Antibodies	Biacore 2000	0.6 µg/mL	direct
IgE (allergy marker)	SPR 20	10 ppb	direct
Cd, Zn, Ni	Biacore X	≈pM	direct
Fibronectin	custom-built	2.5 µg/mL	direct
VEGF	custom-built	1 pM	sandwich
Peanut Allergens	Spreeta	700 ng/mL	direct

Table 1.3: Examples of devices that exploit direct and sandwich detection for medical applications

SPR biosensor technology has made substantial advances in terms of both sensor hardware and biospecific coatings. SPR biosensors have been applied for the detection of a variety of chemical and biological analytes. The performance of SPR biosensor technology will continue to evolve and the advanced SPR sensor platforms combined with novel biospecific surfaces with high resistance to the nonspecific binding will lead to robust SPR biosensors enabling rapid, sensitive, and specific detection of chemical and biological analytes in complex samples in the field. These biosensors will benefit numerous important sectors such as medical diagnostics, environmental monitoring, and food safety and security.

SPR systems have proved to be a powerful tool for the detection of a wide variety of molecules and the studies nowadays focuses on the development of compact SPR systems with high sensitivity and resolution.

analyte	sensor system	detection matrix	limit of detection	detection format
pesticides				
atrazine	Sensia	water	20 pg/mL	inhibition
			1 pg/mL	
chlorpyrifos	custom-built	water	50 pg/mL	inhibition
carbaryl	custom-built	water	1 ng/mL	inhibition
DDT	Sensia	water	15 pg/mL	inhibition
DDT		water	18 pg/mL	inhibition
carbaryl			50 pg/mL	
chloropyrifos			52 pg/mL	
2,4-dichlorophenoxyacetic acid	SPR-20	buffer	0.5 ng/mL	inhibition
	custom-built	buffer	10 ppt	inhibition
2,4,6-trinitrotoluene (TNT)				
	Biacore 2000	buffer	10 pg/mL	inhibition
	Biacore 2000	buffer	10 pg/mL	inhibition
aromatic hydrocarbons				
2-hydroxybiphenyl	SPR-20	buffer	0.1 ng/mL	inhibition
benzo[*a*]pyrene	SPR-20	buffer	0.01 ng/mL	inhibition
	SPR-20	buffer	0.05 ng/mL	inhibition
heavy metals				
Cu^{2+} ions	custom-built	buffer	~pM	direct
Cd, Zn, Ni	Biacore X	buffer	~μM	direct
Cu^{2+}	custom-built	deionized water	32 pM	direct
Ni^{2+}			178 pM	
phenols				
bisphenol A	SPR-20	buffer	10 ng/mL	inhibition
	Spreeta	buffer	1 ng/mL	inhibition
2,4-dichlorphenol	SPR-20	buffer	20 ng/mL	competitive
PCB	Biacore 2000	buffer	2.5 ng/mL	competitive
2,3,7,8-TCDD	Biacore 2000	buffer	0.1 ng/mL	competitive

Table 1.4: SPR sensors for environmental monitoring

1.3.3 Advances in SPR biosensor technology

Currently, several groups are using different SPR approaches to detect a change of refractive index. Sensors using Prism-Coupled SPR (PCSPR) with Kretschmann configuration [33] can be readily combined with any type of interrogation: angular, wavelength, intensity or phase modulation [9]. PCSPR sensors typically show refractive index sensitivity for typical angular interrogation architecture that ranges between 50-150°/RIU [34], with higher sensitivity at shorter wavelengths [35], and refractive index resolutions in the orders 10^{-6}-10^{-7} RIU. An optical sensor based on spectroscopy of long-range surface plasmons was reported by Nenninger et al. [36]. In that work, a long-range surface plasmon was excited on a special multilayer structure consisting of a glass substrate, a Teflon AF layer, and a thin gold layer. A resolution as low as 2 x 10^{-7} RIU was achieved. Most recently, Homola's group demonstrated an improved configuration for

excitation of long-range surface plasmons and demonstrated an SPR sensor with a resolution as low as 3 x 10^{-8} RIU [37].

Development of portable SPR sensor platforms suitable for deployment in the field presents an important direction in SPR sensor research. Several miniaturized SPR optical platforms based on spectroscopy of surface plasmons have been developed. A concept of the miniature SPR sensor based on integration of all electro-optical components in a monolithic platform developed by Texas Instruments in the mid-1990s [38] was further advanced by researchers at Texas Instruments and the University of Washington. The initial version of this platform exhibited a refractive index resolution of 5 x 10^{-6} RIU. Baseline noise and smoothness of response of this sensor were investigated by Chinowsky et al. [39], who showed that the baseline noise established under constant conditions was <2 x 10^{-7} RIU; however, the sensor response to a gradual change in the refractive index revealed departures from the expected sensor output of about 8 x 10^{-5} RIU.

However, PCSPR sensors suffer from cumbersome optical alignment and are not amenable to miniaturization and integration [40]. An alternative common way for SPR excitation is metallic grating couplers that have not been used in SPR sensors as widely as the prism couplers. Grating-Coupled SPR (GCSPR) sensors, in classical mounting, with either wavelength or angular interrogation have been demonstrated to have sensitivity 2-3 times lower than PCSPR [41]. However, GCSPR sensors are compatible with mass production and consequently are an attractive approach for fabrication of low-cost SPR sensing structure. Moreover, they have the intrinsic possibility to be used with different sensing architectures and interrogation systems. Homola's group demonstrated a miniaturized GCSPR sensor implemented with a CCD allowed detection sensitivity of 50°/RIU and resolution of 5 · 10^{-6} over 200 sensing parallel channels [42]. A recent approach was reported by Telezhnikova and Homola [43] with the development of a sensor based on spectroscopy of surface plasmons on diffractive gratings and a refractive index resolution of this sensor was established at 3 x 10^{-7} RIU. Other groups provides high sensing performance by coupling the grating plasmonic field with core-shell nanoparticles, demonstrating an enhancement up to 36 times in angular shift with respect to prism-coupling [44], or using more complex periodic nanostructures such as metamaterial-made sensing layers [45].

2 Plasmonic devices and experimental configurations

In this chapter the devices and the instrumentation used for the measurements will be described. First the various gratings will be presented outlining the fabrication methods and the geometrical features.

The development of an opto-electronic bench for SPR signals analysis had a fundamental role in my activity since the focus of my research had been the realization of compact sensing systems based on GCSPR sensors. It will be described in detail in section 2.2 analyzing the different configurations that allow to acquire the transmitted or reflected light modulated by the periodic structure.

A section has been dedicated to the description of the different functionalization process, performed in the experiments, that allowed to verify the resonance shift due to the refractive index variation and to detect specific analytes.

Measurements of buffer solutions have been carried out by using microfluidic chips which has been developed through two different methods, that will be described at the end of this chapter.

2.1 Grating coupling SPR sensors

Our research focused on grating-coupled SPR sensor, and we have analyzed three different gratings:

- A gold sinusoidal grating, optimized for reflectance measurements in polarization angle modulation
- A gold digital grating, that exploits light Extraordinary Optical Transmission (EOT)
- A silver trapezoidal grating, fabricated through an industrial process and optimized for transmittance measurements in azimuthal angle modulation

In the following sections the different gratings will be described in detail focusing on the geometrical parameters that distinguish them from each other and on the fabrication processes.

2.1.1 Gold sinusoidal gratings for reflectance analysis

The gold sinusoidal grating has been fabricated by LaNN laboratory of CNR of Padova through substrate lithography (by Laser Interference Lithography - LIL), nanostructure replica and thermal evaporation of the plasmonic layer [46] [47]. The material stack and grating geometry has been optimized by theoretical calculations for reflectance analysis in polarization angle modulation, taking into account material chemical stability.

Interferential Lithography (IL) is the preferred method for the fabrication of periodic patterns that must be spatially coherent over large areas. It is a conceptually simple process where two coherent beams interfere in order to produce a standing wave which can be recorded over a sensitive substrate. The spatial period of the pattern can be as low as half the wavelength of the interfering light, allowing for structures down to about 100 nm using UV radiation.

A bottom anti-reflection coating (XHRiC-11, BARC) was spun on a pre-cleaned silicon surface at 3000 rpm for 30 s. After a soft baking step (175°C for 1'), the substrate was coated with a S1805 resist film obtained from a S1805 (Microposit®, Shipley European Limited, U.K.): PGMEA (propylene glycol monomethyl ether acetate) (2:3) solution, with a spin speed of 3000 rpm for 30 s. The exposure step was performed setting the laser incidence angle at 19° and the exposure dose at 40 mJ/cm^2. Exposed regions were removed by immersing the sample in MF319. In a further step, a polydimethylsiloxane (PDMS-Sylgard 184 10:1) mold, obtained from the LIL master, was employed to imprint the nano-pattern onto thiolene resin (Norland Optical Adhesive-NOA 61) replica, supported onto microscope glass slides. Figure 2.1 shows the phases of the described soft lithography.

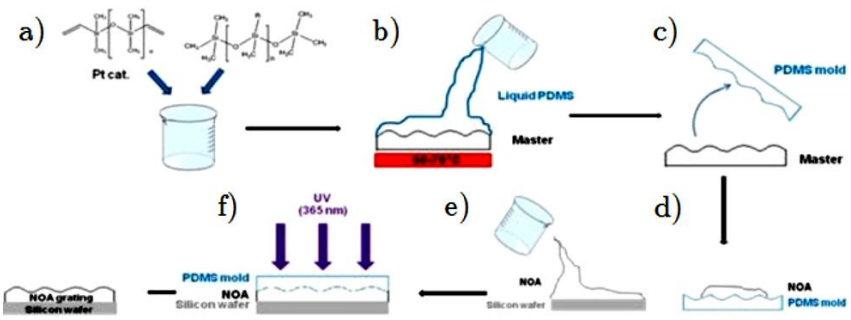

Figure 2.1: Scheme of soft-lithography replica of sinusoidal gratings

A gold (40 nm) layer was evaporated above the patterned resin film and a thin chromium film (5 nm) was used as adhesion layer between the metal and the dielectric. The optical characterization of the grating is shown in figure 2.2: the images are acquired through atomic force microscopy (AFM). The profile reports the values of sinusoidal height and period that are respectively of ≈25 nm and ≈500 nm.

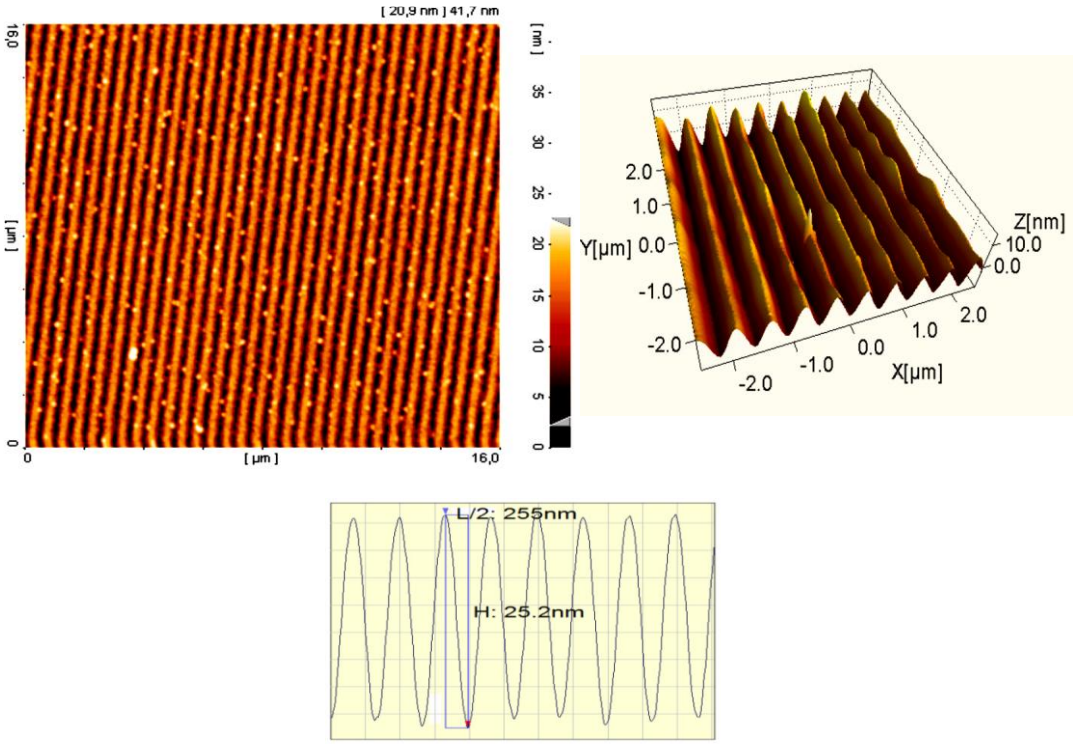

Figure 2.2: The upper pictures represent AFM analysis of a gold sinusoidal grating of period ~ 500 nm (left), and 3D reconstruction (right). The picture below shows the profile of the grating surface.

We decided to use plasmonic gratings with different values of the grating pitch, around 400 and 500 nm, for analysis in aqueous liquid solution and air respectively, in order to use the same sensing bench, that will be described in section 2.2, since it has a fixed incident wavelength of 635 nm. In fact, by scaling the grating period from 500 to 400 nm, when passing from air to water in the dielectric side, surface plasmon resonance is achieved for resonance order m = -1 in both cases and the curves of the resonance polar angle ϑ as a function of the azimuth angle φ almost overlap for the two conditions. Thus, by fixing the incident polar angle at ϑ = 40°, the excitation of high-sensitive SPPs, close to merging condition, is achieved for azimuth rotation around 50° for both types of analyses. On the other hand by performing, for instance, an SPR

analysis in liquid environment with the air-optimized grating of period around 500 nm, SPPs resonance is achieved for resonance order N = +1 in angular configurations which are totally different from the previous ones and with less effective sensing performance [48].

2.1.2 Gold digital gratings for Extraordinary Optical Transmission

Since the discovery of the Extraordinary Optical Transmission (EOT) [49], plasmonic gratings have become subject of great interest. Despite EOT has been discovered on 2D arrays of holes, 1D metallic gratings have become soon object of study, since this geometry is easier to threat. In particular, 1D geometry represents the ideal choice for the transmission analysis of TE and TM polarization. Theoretical studies, performed using different analytical and computational methods [50] [51], showed that the optical response of a metallic grating is given by a combination of three main phenomena [52] [53]: Surface Plasmon Polaritons (SPPs) resonances, whose nature can be only TM, cavity mode resonances (CM), and Wood-Rayleigh anomalies that can be excited both for TE and TM polarization.

Experimental analyzes of 1D gratings are much less than those performed on 2D gratings. Barbara et al. [54] in 2002 presented a first study in the optical regime, using a silica grating covered with gold. Later, Pang et al. [55] presented an experimental study in which different geometrical grating parameters were analyzed. In both cases only the p-polarization case was studied deeply.

For the simple geometry and the limited experimental studies, we decided to analyze the digital grating behaviour developing a compact measurement system.

First a theoretical analysis on grating geometry parameters has been performed, in order to find the grating layout that maximizes the transmittance variation due to a functionalization layer. This theoretical analysis will be explained in detail in section 3.2. The geometry that maximizes the considered sensing parameter (in this case is the transmittance variation when the grating is lighted by p-polarized light) are a gold height of 290 nm and a grating period of 630 nm. These values have been obtained fixing the duty cycle, that is the ratio between the slits width and the period, at 0.4.

Once defined the best geometrical parameters, gratings have been fabricated through Electron Beam Lithography (EBL). The fabrication process consists of different

steps. An EBL process [56] has been performed on a glass substrate by using a JEOL EB6300FS EBL system operating at 100 keV, with 2 nA current. A thin layer of ITO on the substrate acts as conductive layer necessary for the following electrolytic growth. The substrate was previously spinned with a 490 nm thick PMMA resist layer [57]. After the spin coating, the resist has been soft baked at 180 °C on a hot plate for 10 min. A dose of 800 $\mu C/cm^2$ has been used during the exposure. The exposed pattern has been corrected to prevent proximity effects by using Layout Beamer Software. Thanks to the proximity correction, the pattern geometry and uniformity was granted on large areas, even on the sample edges. After the exposure, a deionized water: IPA = 3:7 solution has been used for the resist development (20 s at room temperature). The metallic structures were obtained through an electrolytic growth made on the ITO layer. The electrolytic bath used in the process is the commercial solution Karatclad™ 265 HS, with 4.5 nominal ph. The deposition temperature was 36 °C, Au 8 g/l, density 15 Bè. A growth current of 100 mA, voltage of 2.9 V has been used. The chip layout includes four grating that have been labeled with a number (1 ÷ 4) and an area of 9 mm^2.

Figure 2.3 shows two scanning electron microscope (SEM) images of the gratings.

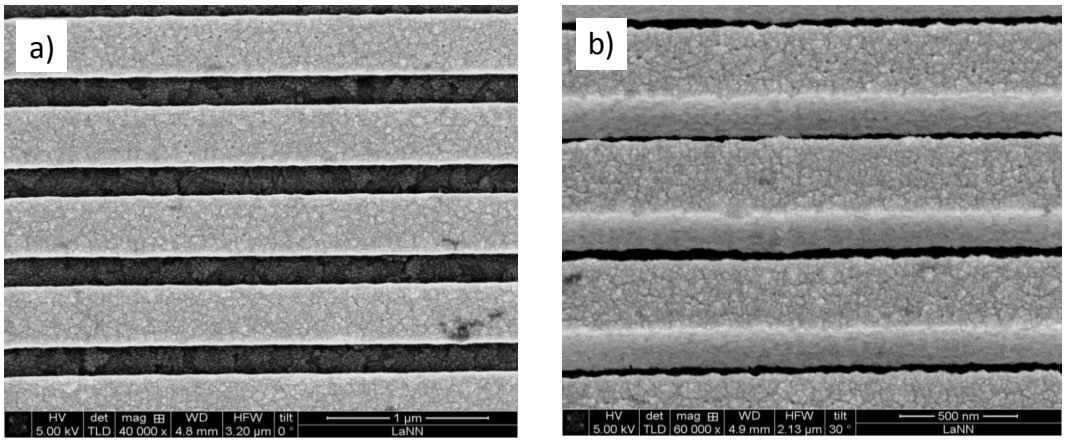

Figure 2.3: A top view SEM image of the grating (a) and a cross section view one (b).

A first experimental characterization has been performed by using a variable angle spectroscopic ellipsometer (J.A.Woollam Co.). The equipment allows performing measurements over a wide spectral range from 193nm up to 2200nm and its variable wavelength and polarization angle of incidence light allows flexible measurements. In

particular, our measurements have been performed at normal incidence, and the polarization angle has been varied from 0° (tangential component of electric field perpendicular to the slits axis - TM) to 90° (tangential component of electric field parallel to slits axis - TE).

2.1.3 Silver trapezoidal gratings for transmittance analysis

Silver trapezoidal gratings have been fabricated through an industrial process of plastic material. For gratings realization, I collaborated with a Spin-Off of university of Padova that is Next Step Engineering, specialized in design and fabrication of sensors based on plastic substrate.

The grating fabrication process consists of various steps. The first step is the molding of the plastic substrate, which presents the periodic nanostructure on a side, by using a stamper, developed by interferential lithography. The silver thin film deposition is made by a physical vapor deposition (PVD) method and different optical densities have been tested (see section 4.3.2). Gratings surface profile is trapezoidal, with a period of 740 nm and a height of about 20 nm. This last parameter can be slightly modified by varying the molding temperature and its effect on plasmonic signal has been experimentally analyzed (see section 4.3.2). We have analyzed different molding temperatures and metal thickness because they are parameters that can be easily changed in the present industrial process. However most of geometrical parameters are currently fixed but changes in the industrial process would allow modifying them.

Figure 2.4 represents the geometry of the silver trapezoidal nanostructure.

Further fabrication details are omitted because they are intellectual property of the Spin-Off.

Grating surface has been optically characterized through atomic force microscopy (AFM), whose images (figure 2.5) confirm geometrical parameters above mentioned.

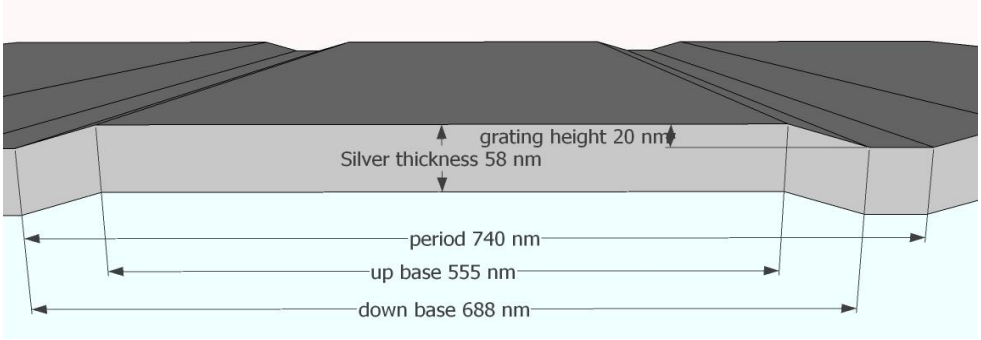

Figure 2.4: Scheme of silver trapezoidal grating geometry

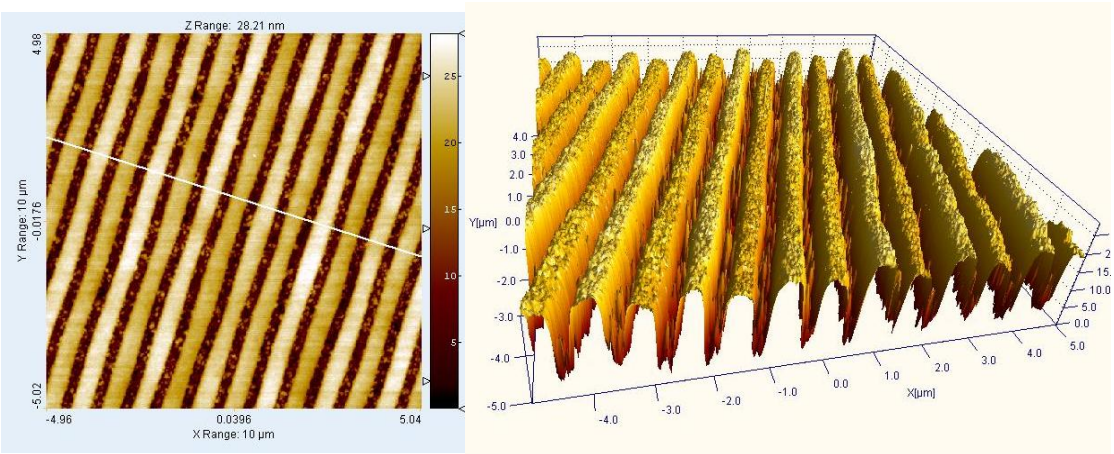

Figure 2.5: Atomic Force Microscopy (AFM) images. On the left an upper view of the grating and on the right a 3D reconstruction

2.2 Measurement equipments

One of the aims of my research activity has been the development of a compact bench capable to vary the set-up parameters involved in SPPs excitation, and consequently to analyze plasmonic resonance effect. The plasmonic signal is then transduced into an electric one, by using a photodiodes array for further signal processing.

The bench has been realized versatile so it can be adapted for both transmitted and reflected light by the grating.

The light source is a 635 nm wavelength laser with circular beam, and its characteristics are summarized in table 2.1.

Wavelength (nm)	635
Laser Class - CDRH	IIIa
Output Power (mW)	4.90
Beam Diameter, $1/e^2$ (mm)	1.10
Beam Divergence (mrad)	0.70
Pointing Accuracy (mrad)	<4
Input Voltage (V)	5-10 DC
Current (mA)	60/70 (Typical/Maximum)
Operating Temperature (°C)	-10 to +40
Storage Temperature (°C)	-40 to +80
Diameter (inches)	0.580
Length (inches)	1.32

Table 2.1: Laser technical characteristics

As above mentioned, laser light modulated by the gratings is then transduced by a photodiodes array. The photodiodes (Hamamatsu© S4111-16R) have been chosen for the low-light-level sensitivity, low dark current and low cross-talk features. Datasheet characteristics are summarized in table 2.2 and the layout is shown in figure 2.6.

Window Material	Resin
Active Area (per 1 element)	Size: 1.45X0.9 mm
	Effective Area: 1.305 mm²
Photo Sensitivity for λ ≈ 635 nm	0.39 A/W
Max Reverse Voltage	V_R = 15 V
Spectral Response Range	λ = [340÷1100] nm
Peak Sensitivity	Λ_P = 960 nm
Dark Current	for V_R = 10 mV: 5 pA
	for V_R = 10 V: 25 pA
Shunt Resistance for V_R = 10 mV	Min: 2.0 GΩ
	Typ: 250 GΩ
Thermal Capacitance	for V_R = 10 mV: 200 pF
	for V_R = 10 V: 50 pF

Table 2.2: Hamamatsu© S4111-16R electrical and optical characteristics at a temperature T=25°.

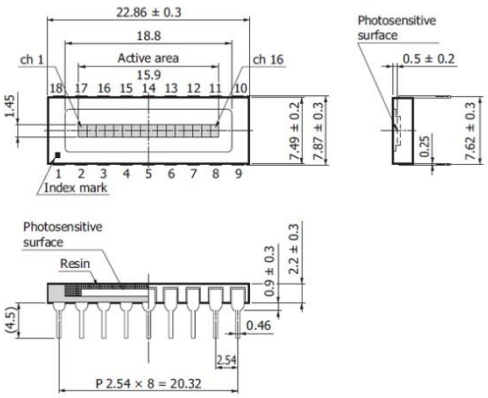

Figure 2.6: Hamamatsu© S4111-16R geometrical characteristic.

As figure 2.6 shows, the photodiodes have been chosen also because its package allows to match the grating substrate with the resin layer for transmitted light acquisition.

Photodiodes signal is controlled first by a switch/control unit (HP 3488A) that allows to connect a single photodiode as well as the whole array. The signal is then acquired by a semiconductor parameter analyzer (HP 4156B), that is very accurate for low current measurements. Both the instruments are controlled by a custom LabVIEW software, which also provides the data acquisition and storage. This equipment has been adopted for this initial phase of system development, even if it is cumbersome. For system miniaturization, a simpler data acquisition instrumentation can be used.

Now we analyze the different bench configurations focusing on the components and instrumentation. A preliminary electrical characterization of the bench has been performed in order to identify the measurements errors.

2.2.1 Reflectance analysis configuration

The reflectance analysis configuration has been realized for gold sinusoidal gratings (section 2.1.1) measurements. This grating has been optimized for reflectance analysis as a function of polarization modulation in conical mounting. First the gold grating is azimuthally rotated in order to support excitation of Surface Plasmon Polaritons (SPPs) with enhanced sensitivity and then a polarization scan of the incident light is performed and reflected light is collected.

The measurements set-up is represented in figure 2.7 where the parameters involved in SPPs excitation are highlighted, i.e.:

- The incoming laser light wavelength λ
- The polarization of the incoming light α
- The incident angle ϑ between the normal to grating surface and incoming light direction
- The azimuthal angle that is the angle between the scattering plane and the grating vector **G**

The test bench is capable to vary all these parameters except the laser wavelength that is fixed at 635 nm.

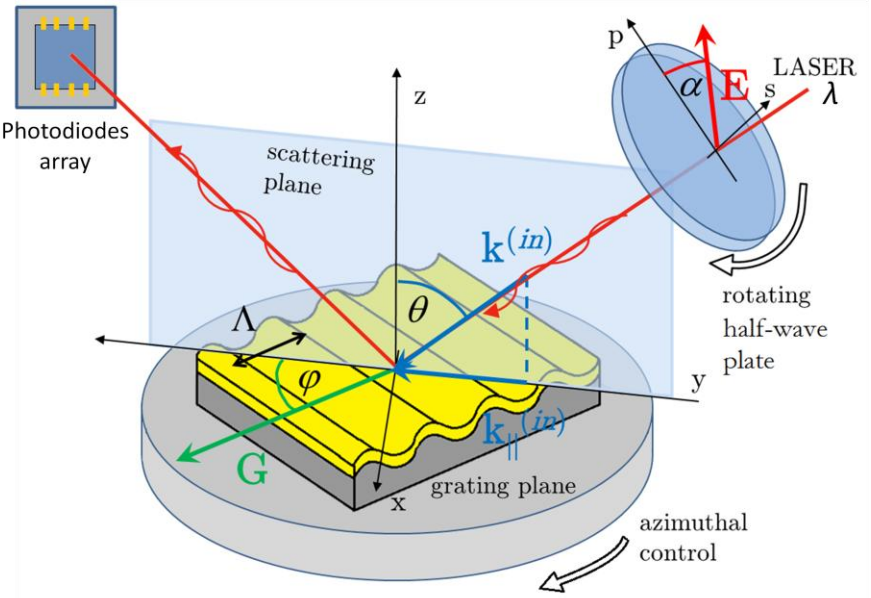

Figure 2.7: Illustration of the experimental setup: fixed-wavelength laser (λ = 635 nm), rotating half-wave plate, plasmonic grating over a sample holder with azimuthal control, photodiode array (or CCD) for reflectivity collection connected to an electronic chain for data transduction. During the polarization-modulation analysis, polar and azimuthal angles (ϑ,φ) are kept fixed in correspondence of the plasmonic resonance and a polarization scan of the angle α is performed.

The realization of this set-up has been performed as follows.

The laser beam passes through a polarizer (Thorlabs: LPVISE100-A), in order to have a steady intensity and a polarized light, and then through a half-wave plate (Thorlabs: LPVISB100-MP), in order to control the polarization lighting the grating. The half-wave plate is mounted on a motorized rotation stage (Thorlabs: PRM1/MZ8E), so

the polarization can be controlled via software with an accuracy of 0.1%, and the measurements are automated. The laser, the polarizer and the motorized rotation stage with the half wave plate are mounted on a vertical rotation stage (Thorlabs: SL20/M, C1525/M, P14) that allows to vary the incident angle of laser beam on grating surface.

The grating holder consists of two translation stages (Edmund: 56-794, Thorlabs: DT25/M) able to move the surface along *x* and *y* directions, a goniometer (Thorlabs: GN18/M) in order to finely adjust the incidence angle (± 5°, accuracy 0.15°) and a metric rotation stage (Edmund: NT55-028) to change the azimuth angle.

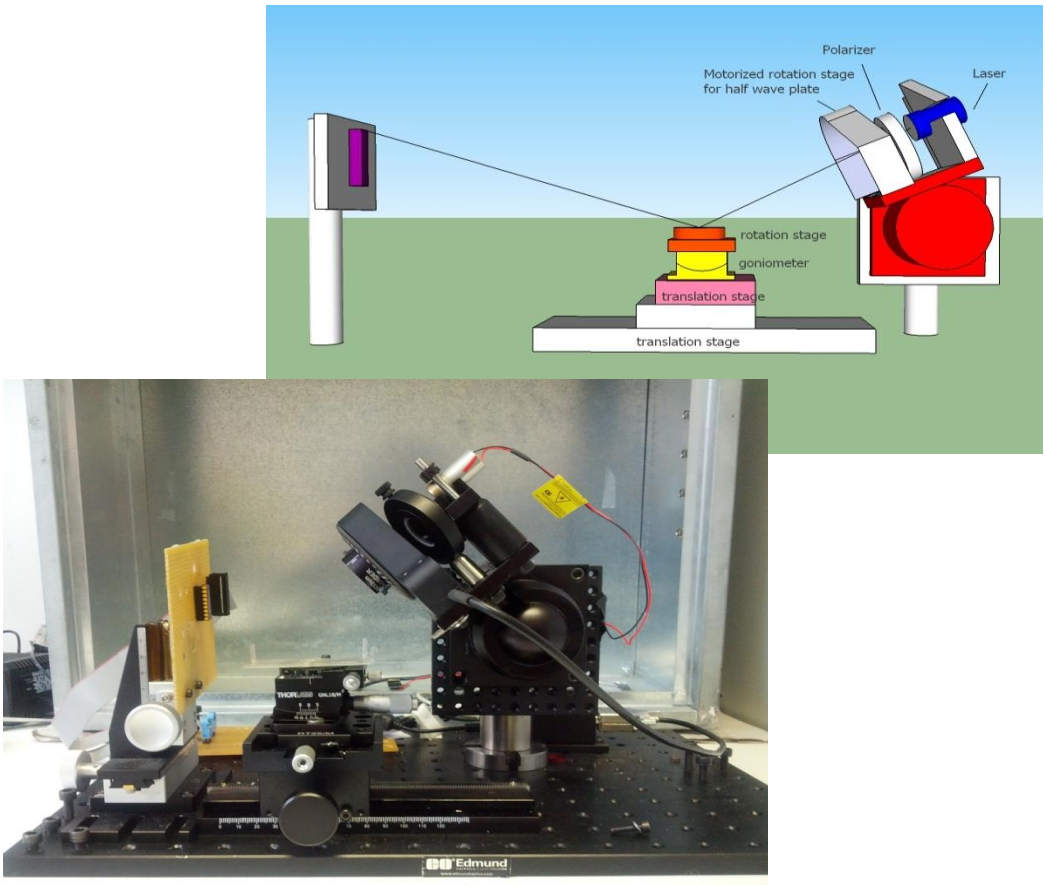

Figure 2.8: Picture and scheme of the developed bench in reflectance analysis configuration. On the right holder the laser and the motorized rotation stage can be distinguished, the central stages allow to align the sample to the incident beam and azimuthally control it, and on the left translation stages there is the photodiodes array mounted on a board.

For functionalization experiments, a custom holder has been developed in order to uniquely fix the grating to the rotation stage and to avoid unwanted azimuth angle

variations. This holder allows to functionalize the grating without removing it and so without changing the resonance azimuthal angle fixed in bare condition. On the contrary, for solution analysis, the grating is embedded in a microfluidic chip which is fixed on the rotation stage controlling the azimuthal angle.

The light reflected by the gratings is detected through commercial photodiodes array (Hamamatsu S4111, 16 elements) which converts the signal into current. The array is mounted in a *y-z* axis translational stage (Edmund: E55-025) that linearly moves it along the two axis, in order to align the laser beam and the active area of a photodiode.

Photodetectors are individually addressable by the switch/control unit, that is connected to the semiconductor parameter analyzer. The bench is shown in figure 2.8, where the gold grating is embedded in a microfluidic chip over the central rotation stage.

2.2.2 Transmittance analysis configuration

The bench can be properly modified in order to analyze also grating transmitted light. As mentioned in sections 2.1.2 - 2.1.3, transmittance analysis has been performed for both gold digital grating and silver trapezoidal one but the configuration is different in the two cases:

- Gold digital grating: in this case the extraordinary transmission is exploited and the transmitted light is analyzed when grating is perpendicularly lighted. In these conditions only transverse magnetic mode (TM) of incident light can affect SPPs excitation, and measurements as a function of incident light polarization must be performed. Transmittance variation, due to dielectric refractive index changes, when the grating is lighted by TM mode light has been considered the sensing parameter.
- Silver trapezoidal grating: this grating is analyzed in conical mounting controlling the azimuthal angle. The peak azimuthal angle variation due to surface refractive index changes is considered the sensing parameter.

We now consider the two configurations in detail and the components mentioned are referred to the ones introduced in section 2.2.1.

Gold digital grating

The bench for the analysis of gold digital grating is very simple, since no incident or azimuthal angle control is required. Transmittance variation when TM mode light reaches the periodic nanostructure, due to the surface dielectric refractive index changes, is the sensing parameter, so no modulation is required. In our analysis, we have preferred to analyze system behavior as a function of light polarization and the only degree of freedom in this bench configuration is the incoming light polarization angle.

As figure 2.9 shows, bench mechanical components are the same of the reflectance analysis configuration but they are properly mounted for this type of measurement. The laser and polarizer holder, that is a rotation stage, is fixed so the laser beam is vertical. The light passes through the polarizer in order to have a steady intensity and then through the half wave plate mounted on the motorized rotation stage: in this way the polarization angle can be varied via software and the measurement is automated. The grating is positioned over the photodiodes array and it is optically matched to the fused silica photodiodes protective layer via an optical matching oil (Cargille Immersion Oil Type A), in order to avoid refractive index variation between the two media.

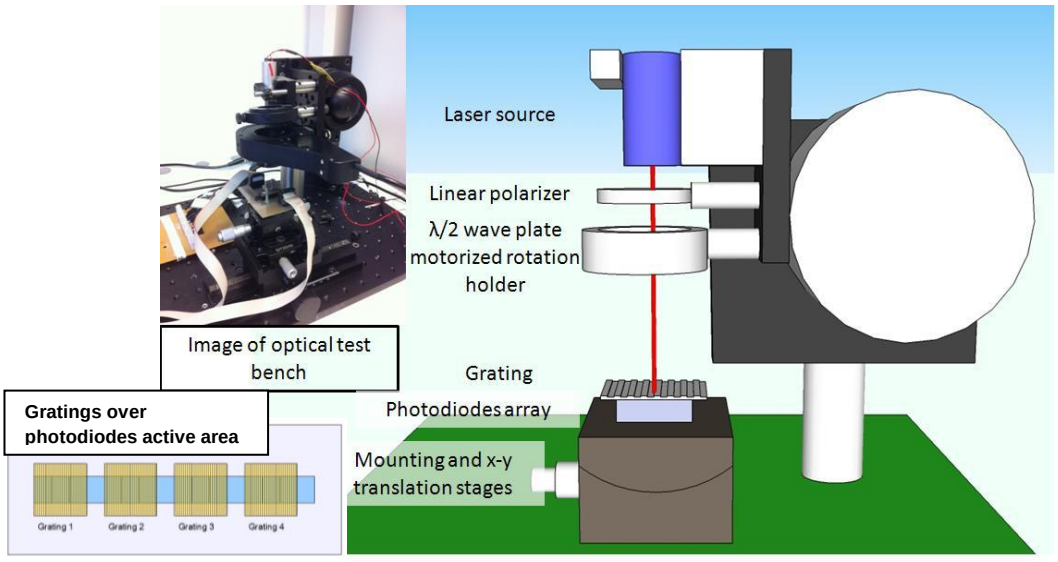

Figure 2.9: Images of the bench for transmittance analysis in polarization angle modulation and a scheme of gratings allocation over photodiodes active area

A custom printed circuit board (PCB) has been developed to contact the photodiodes and fix the array on the translation stages below, that assure the alignment of the grating with the laser beam. Photodiodes signals are processed by the same switch matrix and parameter analyzer mentioned in the previous paragraph.

Silver trapezoidal grating

Silver trapezoidal gratings have been analyzed in conical mounting so the bench configuration is similar to the one presented in paragraph 2.2.1. The main differences consists on the acquisition of transmitted light, instead of the reflected one, and the sensing parameter, that in this case is the peak azimuthal angle variation instead of polarization angle.

The bench is represented in figure 2.10. The rotation stage, that holds the laser and the polarizer, allows the incident angle variation, which can be also finely varied thanks the small goniometer positioned under the laser holder. The grating is optically matched to the photodiodes array by using an optical matching oil, and they are positioned over the motorized rotation stage that controls the azimuth angle. The use of the motorized stage permits to automate the measurements.

The translation stage under it allows to align the laser beam and the sample and also the laser beam with the center of the rotation stage, in order to analyze the same point on the sample for all the azimuthal angles.

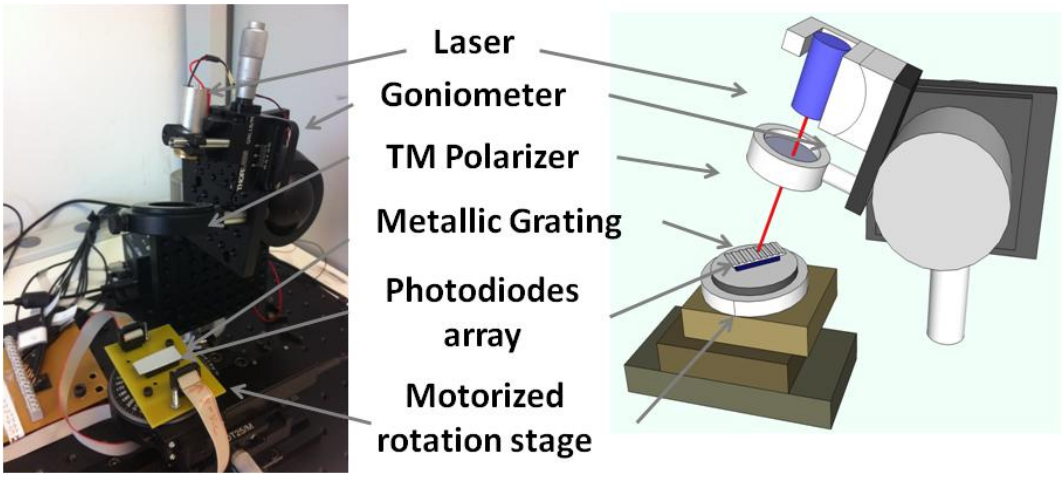

Figure 2.10: Images of the bench for transmittance analysis in azimuthal angle modulation

2.2.3 Test bench electrical characterization

A preliminary electrical characterization of the bench has been performed in order to estimate bench noise and so the errors that could affect the measurements.

First we have analyzed the noise of the photodiodes and laser intensity oscillations. The characterization consists of:

- Voltage-current measurements: the current as a function of the voltage applied to photodiodes is measured through the parameter analyzer (HP 4156B)
- Drift measurements: in this type of measurements the voltage applied to the photodiodes is fixed at -2 V and then the current is measured as a function of time.

In both cases the integration time of the parameter analyzer is set to 20 ms. Photodiodes has been characterized in dark and in laser lighting condition.

Measurements in dark condition allow us to estimate the current variation that affects the measurements when no light illuminates the photodiodes, and its value is of the order of 10^{-10} A. No evident current drift has been noted.

To understand how this intrinsic noise can affect a measurements, photodiodes have been analyzed also when laser light impinges them (figure 2.11).

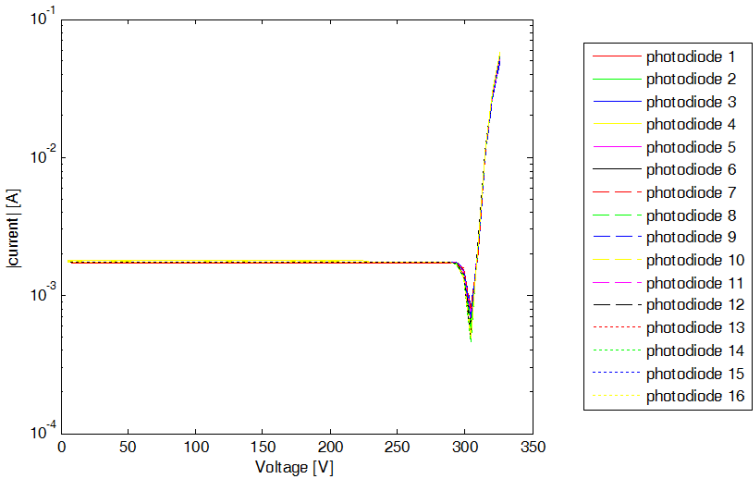

Figure 2.11: I/V measurements of the 16 photodiodes of the array

Table 2.3 reports the values obtained from the measurements. As we can see from the values obtained, the current acquired when photodiodes are lighted by the

laser is seven orders of magnitude greater than the dark condition, so the intrinsic noise of photodiodes can be neglected.

DARK		LASER LIGHT	
CURRENT MEAN	**STANDARD DEVIATION**	**CURRENT MEAN**	**STANDARD DEVIATION**
-5.0×10^{-10} A	2.7×10^{-10} A	-1.749×10^{-3}	9.8×10^{-6}

Table 2.3: Current mean and standard deviation measured through photodiodes in dark and laser light conditions.

We have also evaluated the laser oscillations through measurements as a function of time. We have noted a high laser intensity variation during the few minutes after the laser is switched on, as figure 2.12 shows. Current percentage variation ($(I_{max} - I_{min})/I_{min} * 100$) due to laser oscillations is about 8% but it can be reduced to 6% if the initial temporal window is not considered. This error affects output intensity and it must be considered principally in gold digital grating analysis, since the transmittance variation is the sensing parameter.

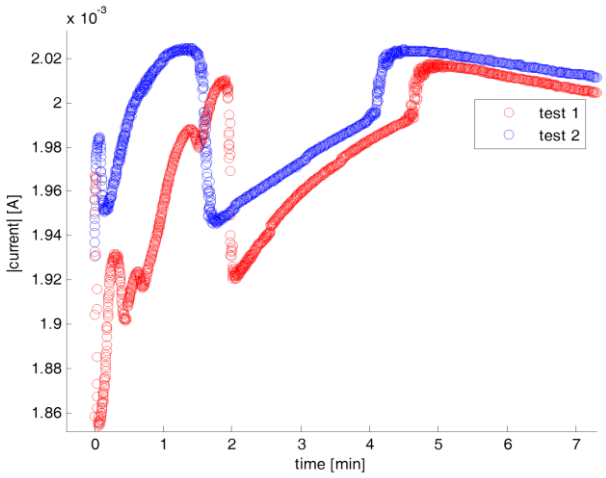

Figure 2.12: Laser drift measurements

The parameters analyzed for the other two gratings are the polarization for the gold sinusoidal grating and the azimuth angle for the silver trapezoidal one. Both the parameters are controlled by the motorized rotation stage, as described in sections 2.2.1 and 2.2.2, so a preliminary study on polarization and azimuth angle errors has been evaluated.

Measurement repetitions with the same test conditions have been performed several times for both bench configurations, in order to better determine the measurements errors. For polarization analysis the phase of the harmonic signal acquired has been evaluated for each measurement repetition, and a parameter variation of 0.12° has been found.

The same analysis has been done for resonance azimuthal angle of silver grating and a parameter standard deviation of 0.019° has been found, with a maximum variation of 0.09° as shown in figure 2.13.

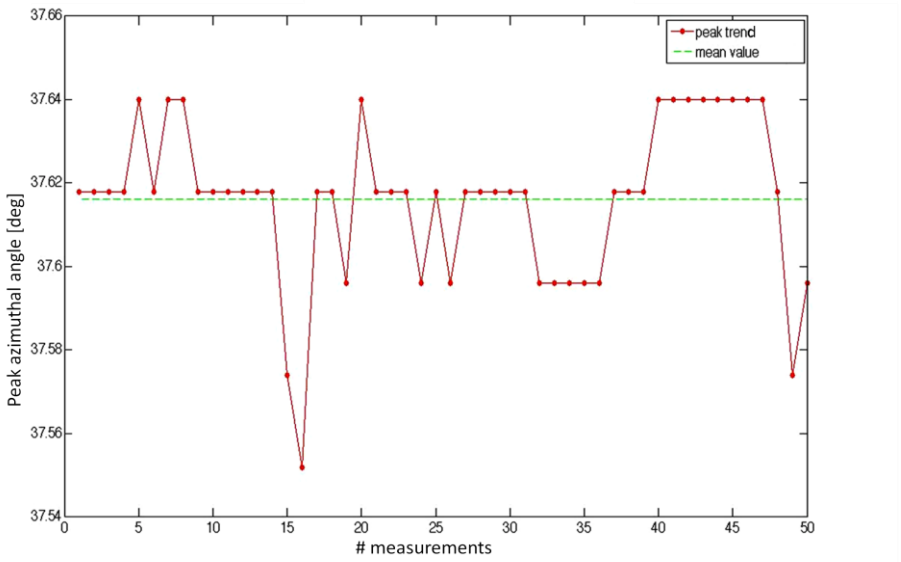

Figure 2.13: Azimuthal angle of the peaks for 50 measurements in the same test conditions.

Errors estimation is fundamental to evaluate if a parameter shift is due to a refractive index change. In fact only the parameter variations higher than the measurement error can determine the presence of an analyte. In chapter 4 we will see that the parameters shifts experimentally found are always greater than the estimated measurement errors.

2.3 Functionalization processes

The functionalization process has a fundamental role in biosensor development, and in particular the choice of the biorecognition element that permits the selective binding with the analyte under analysis.

Surface plasmon resonance conditions shift, due to surface refractive index variation, has been tested through both different functionalization layers and detection of biological molecules. In this section the various molecules used in the experiments and the relative immobilization protocols will be described.

The effective medium approximation method is also introduced, and it will be used in chapter 4 for the approximation of the functionalization layers.

Alkanethiols

Alkanethiols are the most commonly used molecules for self-assembled monolayer (SAM) formation. The study of SAM is particularly promising in the field of sensors, in corrosion prevention, in nanofabrication (especially for information technology), for the construction of nanodevices, for medical implants, and in pharmacology, among others [58].

We have used alkanethiols with increasing carbon chain length, that form a SAM over the grating surface of known thickness and refractive index [59] [60] [61]. These characteristics allow us to test the capability of our sensor to detect refractive index variations.

Alkanethiols are molecules composed of: a headgroup (linking group), a backbone (main chain), and a specific terminal (active) group. The headgroup guides the self-assembly process on the substrate, linking the hydrocarbon chain (of variable length) to the metal surface through a strong bond (figure 2.14). The interactions among backbone hydrocarbon chains (involving Van der Waals and hydrophobic forces) ensure the packing of the monolayer and contribute to stabilize the structures. The terminal group confers specific properties to the surface (hydrophilic, hydrophobic), controlling interactions on the metal/environment interface and it can be used to immobilize different molecules, biomolecules, or nanostructures by weak interactions or covalent bonds. On the other hand shorter chains have been shown to lead to denser packing

while a more complex and less dense packing is typical for the longer-chain species [62]: for longer strands the surface coverage decreases, consistently with a less-ordered arrangement of the longer chains, presumably due to an increasing polymeric behavior.

The alkanethiols we used are C-chains, that are defined by the chemical formula $CH_3(CH_2)_{n-1}SH$ and end with a thiol group (-SH) that allows the link with the substrate.

The molecules used are: C_6 (1-Mercaptohexane, $CH_3(CH_2)_5SH$), C_8 (n-Octylmercaptan, $CH_3(CH_2)_7SH$), C_{12} (n-Dodecyl mercaptan, $CH_3(CH_2)_{11}SH$) and C_{18} (Mercaptan C_{18}, $CH_3(CH_2)_{17}SH$).

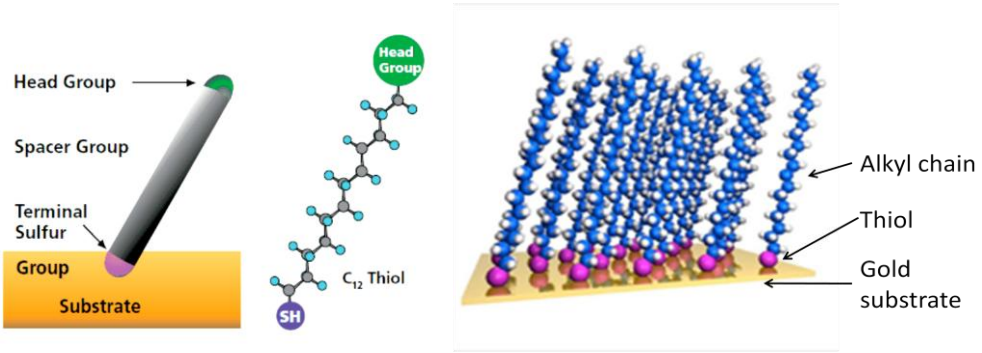

Figure 2.14: scheme of alkanethiols structure and the binding onto a gold substrate

Two different functionalization protocols have been performed: by immersion and by drop-casting.

For functionalization processes by immersion, alkanethiols are dissolved in ethanol at the concentration of 10 mM. Each grating is positioned in a Petri dish and it is immersed in the functionalization solution for twelve hours. The Petri dish is closed with parafilm. The grating is then rinsed in abundant deionized water and dried under N_2 flux.

Concerning the drop-casting functionalization, alkanethiols are dissolved in glycerol in order to avoid the rapid evaporation of the solution. Each grating is positioned in a Petri dish, covered by a 20 µl drop of the functionalization solution for twelve hours and in controlled humidity condition. The Petri dish is closed with parafilm. The grating is then rinsed in abundant deionized water and dried under N_2 flux.

All the reagents are provided by Sigma Aldrich.

Avidin/biotin reaction sample preparation

The avidin-biotin complex is the strongest known non-covalent interaction (K_d=10^{-15}M) between a protein and ligand. The bond formation between biotin and avidin is very rapid, and once formed, because of its non-covalent nature, is unaffected by extremes of pH, temperature, organic solvents and other denaturing agents [63]. Like secondary antibodies, the avidin-biotin detection system allows an almost unlimited number of primary detection reagents (i.e., antibodies, nucleic acids probes and ligands) to be easily captured, recovered, immobilized or detected with a very small number of secondary detection reagents generated by modifying avidin or streptavidin [64]. Thus because of the versatility of this binding and its wide range of applications for sensing purposes, biotin/avidin reaction was chosen as detection-test assay. Due to Surface Plasmons (SPs) high sensitivity to surface conditions, non-specific protein adsorption onto the plasmonic sensing surface gains an important role in the biodevice preparation [65]. For this aim it is widely accepted that a hydrophilic spacer layer has to be inserted between the probe and the surface (a metal in our case).

Several polymers have been suggested and are being successfully used as spacing layer, among which cellulose, dextran, acrylamide, alkanethiolate SAMs, phosphorylcholine derivatives, and poly(ethylene oxide) (PEO) (also called polyethylene glycol – PEG), well known for its resistance to nonspecific protein adsorption. The use of PEO for the inhibition of protein adsorption from biological media has been widely demonstrated since the '80s [66] [67] [68]. Besides the excellent resistance to nonspecific protein adsorption, poly(ethylene oxide) has the peculiarity to allow single-step experimental approaches to immobilize the sensor probe to the surface [69]. Within the specific case of SPR application, a thiol group can be attached to one end for metal-polymer binding, while the other end can be used as the biorecognizing element (e.g. a peptide, antibody or nucleic acid probe). Bio-recognizing layers on top of gold surfaces are commonly built up following a multiple step approach, in which a first deposition of a thiolated compound (that forms the first self-assembled monolayer) is later followed by a bioconjugation step through which the biosensing element is covalently linked to the other end of the thiol compound. However, the efficiency of each of these steps may vary with some deposition variables (e.g. the degree of thiol oxidation, the pH and concentration of the reagents in covalent coupling) and this can

lead to later inter-assay sensing variability. In order to reduce this risk, a standardized deposition strategy is desirable in which the sensitive variables are minimal. This can be achieved by carrying out the deposition through a single step procedure using a thiol derivative with its second-end that already contains both the sensing ligand and the PEO moiety.

In our case, PEO polymer chain was bound to the gold plasmonic platform via a Cysteine-terminated group, while the other functional end was linked to a biotin molecule which is known to assure a great affinity and specificity to avidin in biological solutions [70].

Thiol-protected end-functionalized biotin-PEO-Cys (bPEO) was synthesized by coupling S-trityl-cysteine to the hydroxyl end of biotin-PEO Mw 5 KDa. The trityl group (trt) acts as protector from oxidation of the reactive cysteine thiol residue, and it can be easily removed by acidic treatment with trifluoroacetic acid (TFA) just prior to grafting onto the gold surface.

Gold-coated substrates were pre-cleaned in a basic peroxide solution (5:1:1 double distilled H_2O, 30% H_2O_2 and 25% NH_4OH) for 10 minutes, rinsed in double distilled water and dried under N_2 flux. The trt-protective group was removed immediately before deposition by dissolving the α-methoxy-ω-trt-cys-poly(ethyleneoxide) powder in the minimum amount of TFA (about 20 µl) for 20 minutes at room temperature. N_2-saturated double distilled H_2O was then added up to reach 1 mM final thiol concentration. The insoluble trt residue was removed by centrifugation (10000 g, 4°C, 10 min). mPEO-Cys deposition was then carried out by immersing the substrate in the supernatant solution for 48 h.

The biorecognition event was performed by immersing a 4 µg/ml avidin/dilution buffer solutions for 2 hours over the bPEO-Cys-coated surface. ω-trt-cys-monomethoxypoly(ethylene oxide) (mPEO, 5KDa), S-trityl-cysteine (trs-Cys), trifluoroacetic acid (TFA) were purchased from Sigma-Aldrich.

DNA detection

Conventional methods for the analysis of specific gene sequences are based on either direct sequencing or DNA hybridization methods. Because of its simplicity, the

second option is more commonly used in diagnostic laboratories. In DNA hybridization, the target gene sequence is identified by a DNA probe that can form a double-stranded hybrid (dsDNA) with its complementary nucleic acid, i.e., the target sequence (cDNA), with high efficiency and extremely high specificity, even in presence of a complex and heterogeneous sample. DNA probes are single-stranded DNA (ssDNA) labeled to provide detectable signals after successful DNA hybridization [71], that create a self-assembled monolayer on the electrode surface during functionalization process (figure 2.15).

It is possible to improve the efficacy of the DNA capturing probe by using DNA analogues with superior properties than DNA itself [72]. Peptide Nucleic Acids (PNA) are an example, consisting of a backbone of repeating N-(2-aminoethyl)glycine units linked by peptide bonds and bearing nucleotide bases. When compared to their DNA or RNA analogues, PNAs possess higher affinity for sequence-complementary oligonucleotides, are chemically more stable and allow better discrimination between fully complementary and single-base mismatched DNA sequences. In our experiments a biorecognizer layer consisting of PNA probes was exploited for the detection in biological solution of complementary 22mer DNA strands.

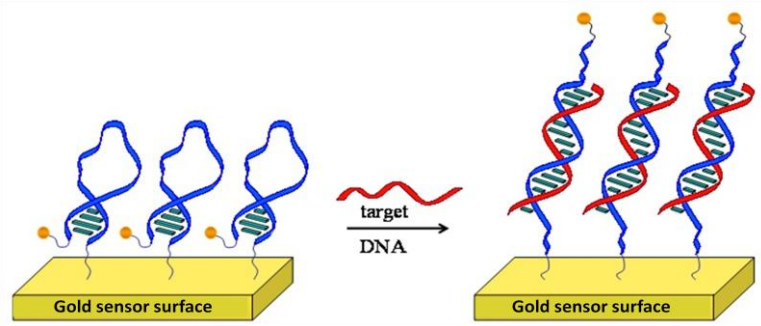

Figure 2.15: Hybridization event of a DNA target with ssDNA immobilized over the sensor active area.

The gold substrate was cleaned just prior to use (10 minutes in a 5:1:1 double distilled H_2O, 30% H_2O_2 and 25% NH_4OH solution) and then immersed in a 20 µM HS-PNA solution in deionized H_2O. The PNA chain is a sequence of 22 nucleotides. After 24 h the substrate was rinsed with deionized H_2O and dried. A HS-PEG (MW 458.6) capping layer was deposited by immersing the grating in a PEG aqueous solution (4.84 mM) for 2 h, rinsed thoroughly and dried, in order to avoid nonspecifically adsorbed sequences from the surface. The sensing layer was immersed in a 1 µM DNA solution in saline-sodium citrate (SSC) at 35°C for 2 h.

Effective medium approximation (EMA) for thin coating film

The capability of the GCSPR systems developed to detect surface refractive index variations have been tested by means of a functionalization of the metal surface with thin self-assembling coating layers. The comparison of plasmonic signal before and after the functionalization process provides information about the change of plasmonic resonance conditions, such as dip position shifts in term of incident or azimuthal angle or polarization.

In order to estimate the refractive index sensitivity $S_n = \Delta Y/\Delta n$, where ΔY is the shift of the sensing parameter, depending on the selected modulation, an estimation of the effective refractive index variation *n* due to a monolayer functionalization is necessary, since the adsorbed films are much thinner than the decay length of SPPs evanescent field. The confined SPPs electromagnetic field decays exponentially into a dielectric medium that is different for the presence of the functionalization layer. The effective permittivity ε_{eff} is calculated by averaging the permittivity $\varepsilon(z)$ over the depth of the whole multilayered structure, always weighting the local refractive index with a factor that takes into account the exponential decay of the field [61]. The intensity of light is the field strength squared, so it decays with height *z* above the metal surface as $[\exp(-z/l_d)]^2$, where l_d is the extension length of the excited SPPs. Thus, the proper weighting factor in calculating this average refractive index should just be $[\exp(-z/l_d)]^2=\exp(-2z/l_d)$. This average is therefore calculated with the depth integral:

$$\varepsilon_{eff} = \frac{2}{l_d}\int_0^\infty \varepsilon(z)\exp\left(-\frac{2z}{l_d}\right)dz \qquad (2.1)$$

From Maxwell's equations we get an analytical expression for the extension length as a function of the exciting wavelength λ and the surrounding media:

$$l_d = \frac{\lambda}{2\pi}\sqrt{-\frac{\varepsilon_{eff}+\varepsilon_m}{\varepsilon_{eff}^2}} \qquad (2.2)$$

where ε_m is the dielectric permittivity of the metal. For a single-layer functionalization of thickness *d* and dielectric permittivity ε_l, as the one shown in figure 2.16, we find out from eq. 2.1:

$$\varepsilon_{eff} = \varepsilon_b + (\varepsilon_l - \varepsilon_b)\left(1 - e^{-\frac{2d}{l_d}}\right) \qquad (2.3)$$

where ε_b is the dielectric permittivity of the bulk solution ($\varepsilon_b = \varepsilon_0$ if the functionalization layer is in contact with air).

Figure 2.16: Schematic diagram of a bilayer structure involving a functionalization layer of thickness *d* and refractive index ε_l directly on the metal surface, above which is bulk solution (ε_b) or air (ε_0)

Since the layer thickness is usually much thinner than the SPPs extension length in air (d/ $l_d \approx 10^{-2}$) it is reasonable to approximate:

$$\Delta\varepsilon = \varepsilon_{eff} - \varepsilon_0 \cong (\varepsilon_l - \varepsilon_0)\frac{2d}{l_d} \quad (2.4)$$

Inserting this expression into equation 2.2, we obtain a third degree polynomial equation to be solved in l_d unknown, that is:

$$\pi^2\varepsilon_0^2 l_d^3 + [4d\pi^2\varepsilon_0(\varepsilon_l - \varepsilon_0) + 4\pi^2(\varepsilon_l - \varepsilon_0)^2 d^2 + \lambda^2(\varepsilon_l + \varepsilon_m)]l_d^2 + \frac{d}{2}(\varepsilon_l - \varepsilon_0)\lambda^2 = 0 \quad (2.5)$$

and l_d can be obtained with the condition $l_d \geq 0$. Its value can be substituted in equation 2.4 in order to estimate the effective refractive index change:

$$\Delta n_{eff} = \frac{\partial n}{\partial \varepsilon}\Delta\varepsilon_{eff} \cong \frac{\varepsilon_l - \varepsilon_0}{\sqrt{\varepsilon_0}}\frac{d}{l_d} \quad (2.6)$$

Thus if film thickness and optical properties, in terms of complex dielectric permittivity, are known, it is possible to estimate the corresponding variation n_{eff} in the effective refractive index which affects the excited surface plasmon polaritons.

2.4 Microfluidic chips fabrication

The estimation of sensors sensitivity has been developed through measurements of solutions with different refractive indexes, by using a microfluidic chip that allows the solution to flow to the sensor surface.

Two different microfluidic chips have been developed: one for the gold sinusoidal gratings, fabricated by LaNN laboratory through soft-lithography technique, and one for the silver trapezoidal gratings, developed in collaboration with the Spin-Off Next Step Engineering.

Concerning the first, the microfluidic cell embedded into the plasmonic platform was fabricated by soft-lithography technique using commercial thiolene resin optical adhesives [73]. The resulting structure is a two-level resin cell on a glass substrate, consisting of a gasket with an opening in the detection zone and inlet ports distant from the detection region so that tube connectors can be placed farther apart and do not obstruct the optical path. The first bottom layer is fabricated as it follows (see figure 2.17 for a schematic description): thiolene monomer liquid NOA61 (Norland Products Inc. Cranbury USA) is inserted between two surfaces, being the upper surface a thin, transparent polyethylene (PE) sheet, while the lower surface a microscope glass slide. The two surfaces are kept separated by spacers. The monomer liquid is photopolymerized with UV light (365 nm, 5000-PC DYMAX UV-light lamp) with a transparency mask to locally solidify the adhesive in the exposed zones [74]. The UV exposure dose is chosen high enough to solidify the whole layer thickness but not so high to produce full curing of the adhesive to the PE sheet (“partial-curing”). The uncured residual liquid is then removed by rinsing with a solution 1:1 of acetone and ethanol followed by drying under a nitrogen stream. The same procedure can be repeated in order to reproduce any other thiolene pattern that in turn is bound to the multilayered cell. Thus the second and top layer is fabricated by repeating the above steps with a thin layer of NOA enclosed between two PE sheets. After exposure, the supporting PE sheets can be easily peeled away, leaving the thiolene pattern to be applied on the substrate. To improve the adhesion of the two layers, the whole setup is finally exposed to UV radiation (“hard-curing”).

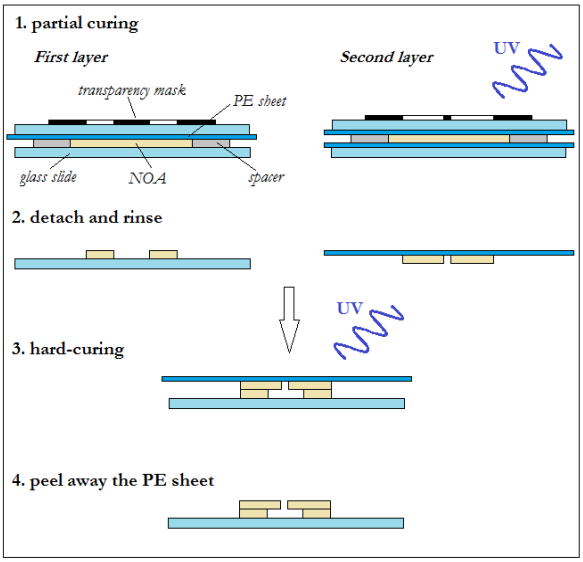

Figure 2.17: Diagram of the soft-lithography process for the two-level cell fabrication

The second microfluidic chip has been fabricated in collaboration with Next Step Engineering, through a particular technique of polymer etching, able to create clear-cut profiles without deforming the planar structure. This technique is used to create the microfluidic channel and the central fluid chamber on a plastic substrate that is then united to the grating thanks an adhesive layer, cut through a plotter, and to another plastic layer that has the input and output holes for tube connectors (figure 2.18).

The microfluidic system contains 200 µl of solution, and a microfluidic pump (Gilson-Peristaltic Pump MINIPLUS Evolution) is used to flow the liquids inside the system. The microfluidic chip is shown in figure 2.18.

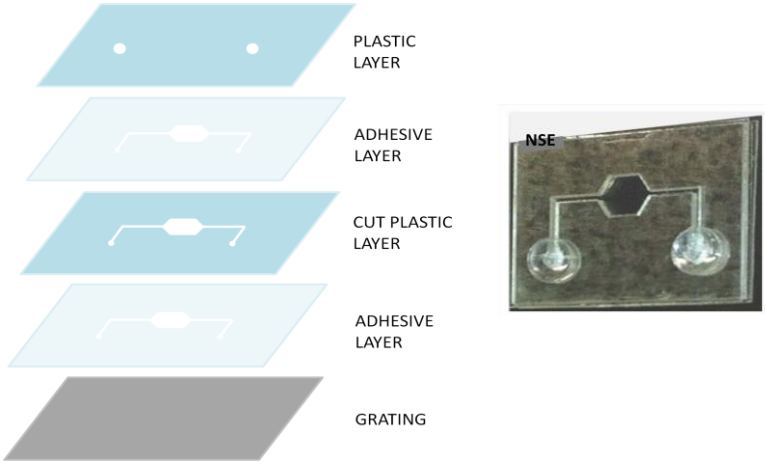

Figure 2.18: Scheme of microfluidic chip construction on the left and the picture of the microfluidic chip on the right

3 Theoretical analysis and simulations

Surface plasmon polaritons excitation and propagation on the various periodic structures has been analyzed through different simulation methods. In this chapter the different approaches are briefly presented focusing on simulations results that will be compared to experimental results in the next chapter.

3.1 Vector model of gold sinusoidal grating

The vector model provides a simple but effective approach for the study of surface plasmon polaritons excitation and propagation on periodic structures. In this analysis, the grating is modeled as an uniaxial crystal with a momentum ***G***, whose modulus is given by $G=2\pi/\Lambda$, where Λ is the grating period. Incident light momentum couples with grating vector ***G*** and surface plasmons are excited if the resonance condition for the on-plane components (equation 1.41) is satisfied.

The equation of momentum-conservation law plays a fundamental role in this approach, since it represents the only available condition in order to describe and analyze SPPs excitation. This method can give information about SPPs excitation as a function of incident angle and light wavelength, but since further details such as grating profile and shape are not taken into account, this approach is a good approximation just for shallow gratings. An analysis of the effects of groove depth and shape on SPPs resonance should require a more complex and rigorous approach.

If a metallic grating is illuminated with fixed wavelength λ and varying incident polar angle ϑ, a reflectivity dip appears in correspondence of the incidence angle ϑ_{res} at which the momentum-conservation law on the grating plane (equation 1.41) is satisfied. In the case of shallow grooves, the expression of k_{SPPs} (equation 1.25) valid for flat interfaces is a good approximation.

In the considered reference frame, the scattering plane is kept fixed and parallel to the x-axis, the grating vector ***G*** and the SPP momentum $\boldsymbol{k}_{SPPs}$. Since the grating period Λ is about 500 nm, i.e. lower than the typical incident wavelength in the optical range, in our cases of interest the resonance order is usually m = −1 , thus eq. (1.41) becomes:

$$\boldsymbol{k}_{SPPs} = \boldsymbol{k}_{||}^{(in)} - \boldsymbol{G} \tag{3.1}$$

If scattering plane is parallel to grating vector ***G***, equation 4.1 leads to the scalar relation

$$\frac{2\pi}{\lambda}\sqrt{\frac{\varepsilon_m\varepsilon_d}{\varepsilon_m+\varepsilon_d}} = \left|\frac{2\pi}{\lambda}\sin\vartheta_{res} - \frac{2\pi}{\Lambda}\right| \tag{3.2}$$

where ϑ_{res} is the incident angle in which the surface plasmon resonance occurs.

3.1.1 Non-zero azimuthal incident angle analysis

The previous analysis can be generalized by introducing a non-zero azimuth angle that is the angle between the scattering plane and the grating vector ***G*** (fig. 3.1).

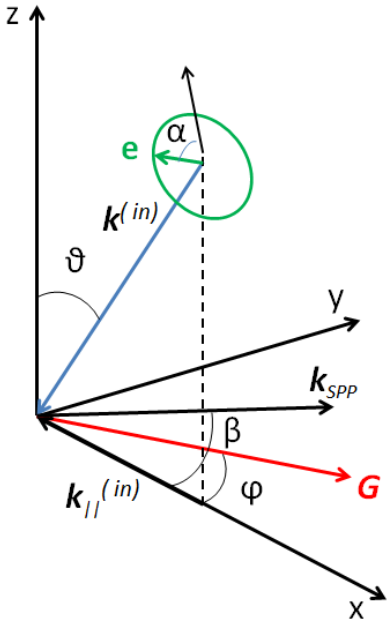

Figure 3.1: Scheme of the considered reference frame and scattering plane orientation

The incoming plane wave direction is now described with the polar angle ϑ and the azimuth angle φ, respectively formed by the wavevector with the normal to the surface and with the x-axis direction. So the grating vector is no more parallel to x-axis direction and its components in the Cartesian system (figure 3.1) are:

$$\boldsymbol{G} = (G\cos\varphi, G\sin\varphi, 0) \tag{3.3}$$

Considering $\boldsymbol{k}^{(in)}=(k_0\sin\vartheta, 0, -k_0\cos\vartheta)$, with $k_0=2\pi/\lambda$, the resonance condition is given by

$$k_{SPP,x} = k_0 n_d \sin\vartheta + m\frac{2\pi}{\Lambda}\cos\varphi = k_{SPP}\cos\beta \tag{3.4a}$$

$$k_{SPP,y} = m\frac{2\pi}{\Lambda}\sin\varphi = k_{SPP}\sin\beta \tag{3.4b}$$

where n_d is the refractive index of the dielectric, $k_{SPP} = k_0\sqrt{\frac{\varepsilon_d\varepsilon_m}{\varepsilon_d+\varepsilon_m}}$, and β is the angle between the vector k_{SPP} and the x-axis.

From equation 3.4 we can obtain the explicit expression for the resonance incident angle [75], considering m=-1:

$$\vartheta_{\mp} = arcsin\left(\frac{\lambda}{\Lambda}\cos\varphi \mp \sqrt{S^2 - \left(\frac{\lambda}{\Lambda}\sin\varphi\right)^2}\right) \tag{3.5}$$

where $S=k_{SPP}/(2\pi/\lambda)$.

As a consequence of the last expression, SPPs are supported by a grating structure only in the azimuth range where the term under square-root is positive, i.e.:

$$S^2 - \left(\frac{\lambda}{\Lambda}\sin\varphi\right)^2 \geq 0 \tag{3.6}$$

From the last equation the range of azimuth angle values can be obtained:

$$0 \leq \varphi \leq arcsin\left(S\frac{\Lambda}{\lambda}\right) = \varphi_{max} \tag{3.7}$$

For azimuth angle greater than φ_{max} no resonance angle ϑ_{res} can exist. ϑ_- is an increasing function of azimuth angle (fig. 3.2), in fact the resonance polar angle shifts towards greater values as far as the resonance value in correspondence of the maximum φ_{max} is assumed.

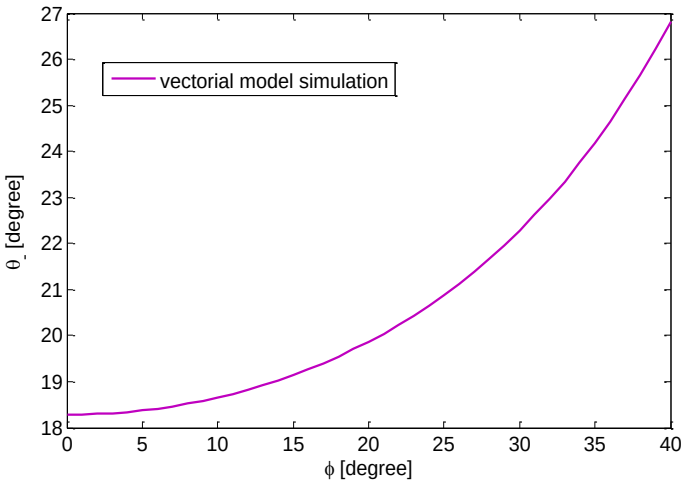

Figure 3.2.: Simulated resonance angle ϑ_{res} as a function of azimuth φ, considering a silver grating with Λ=500 nm.

Depending on the grating period Λ and on the incident light wavelength λ, also a second solution ϑ_+ in eq. 3.5 could exist between a critical azimuth angle φ_c and the maximum value φ_{max}: in this range two resonance dips can be excited with the same incident wavelength at two distinct resonance angles ϑ_- and ϑ_+ [75]. For azimuthal

rotation larger than the critical value, the SPPs energy threshold corresponds to the excitation of SPPs directed perpendicularly to the incident light. The critical azimuth angle is given by:

$$\varphi_c = arccos\left(\frac{1-S^2+\frac{\lambda^2}{\Lambda^2}}{2\frac{\lambda}{\Lambda}}\right) \tag{3.8}$$

The second resonance ϑ_+ shifts towards lower values as far as it reaches the resonance value in correspondence of the maximum azimuth. The two dips approach and merge into a single broad dip in correspondence of the maximum azimuth value φ_{max}.

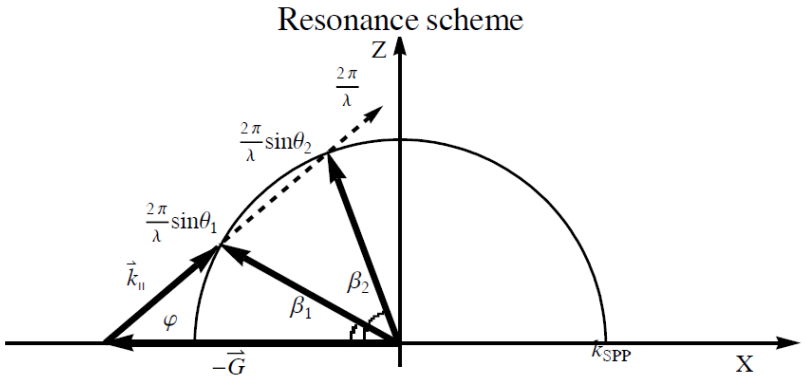

Figure 3.3.: Scheme of the resonance configuration for in-plane incident momentum $k_{\parallel}$, SPP momentum k_{SPP} and grating vector *G*.

Romanato & al. [76] demonstrated that sensitivity can be enhanced of one order of magnitude, with respect to conventional fixed grating, if the grating is azimuthally rotated until the excitation of double SPPs with a single wavelength, as depicted in figure 3.4. The SPPs propagation direction can be controlled by rotating the grating azimuthally and double SPPs excitation by a single wavelength is possible when the grating azimuthal rotation is larger than a specific angle. Under this condition, a small change in refractive index induces a much larger change in reflectivity, resulting in a higher sensitivity (more than 10 fold increase) than that for the non-rotated case.

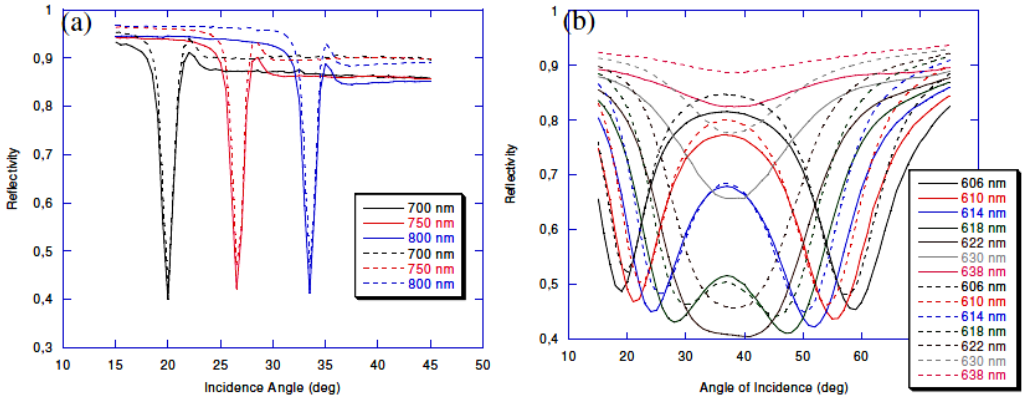

Figure 3.4: Comparison of SPR spectrum between uncoated (solid line) and C_{12}-coated (dashed line) Au grating. (a) Grating with φ = 0° (conventional mounted grating), where different line colors correspond to different incident wavelengths; and (b) φ = 60° (2 SPPs by single wavelength excitation condition), different colors of line represent difference incident wavelength.

3.1.2 Dependency on incident light polarization

In the classical mounting, where the scattering plane is parallel to the grating symmetry plane, only transverse magnetic mode (TM-mode) is capable to excite surface plasmon polaritons: under TM-mode illumination, a dip appears in reflectivity in correspondence of the incidence angle ϑ_{res} at which the incident energy couples with surface plasmon modes and dissipates while propagating along the metal surface.

For non-zero azimuth angle, the symmetry is broken and therefore not only TM-mode but also transverse electric mode (TE-mode or *s*-polarization) can contribute to SPPs excitation. As azimuth increases, *p*-polarization (TM-mode) is no longer the most effective for SPPs excitation and the illuminating polarization must be tuned in order to optimize the coupling.

Reflectivity-minimum R_{min} exhibits an harmonic dependence on polarization angle α with a periodicity of π [77]:

$$R_{min} = f_0 - f_1 \cos(2\alpha + \alpha_0) \tag{3.9}$$

where f_0 , f_1 and α_0 are expected to be fitting parameters that depend on the incidence angles and wavelength and on the optical properties of the metallic grating (layer materials and thicknesses).

This behavior can be explained by assuming that only the electric-field that lies on the grating symmetry plane affects SPPs excitation and the other components affects the reflectivity term. Using versor notation we have:

$$\mathbf{E} = \mathrm{E}\vec{\mathbf{e}} \tag{3.10a}$$

$$\boldsymbol{k}_{SPP} = k_{SPP}\vec{\boldsymbol{k}}_{SPP} \tag{3.10b}$$

$$\boldsymbol{G} = G\vec{\boldsymbol{g}} \tag{3.10c}$$

with

$$\vec{\mathbf{e}} = (\cos\alpha\cos\vartheta, \sin\alpha, \cos\alpha\sin\vartheta) \tag{3.11a}$$

$$\vec{\boldsymbol{k}}_{SPP} = (\cos\beta, \sin\beta, 0) \tag{3.11b}$$

$$\vec{\boldsymbol{g}} = (\cos\varphi, \sin\varphi, 0) \tag{3.11c}$$

and $\vec{\mathbf{n}} = (0,0,1)$ identifies the direction normal to the grating surface.

The reflectivity term results to be proportional to:

$$R \propto |\vec{\mathbf{e}} \cdot (\vec{\mathbf{g}} \times \vec{\mathbf{n}})|^2 \tag{3.12}$$

Using versor notations (3.11a-c), it follows:

$$\vec{\mathbf{e}} \cdot (\vec{\mathbf{g}} \times \vec{\mathbf{n}}) = \cos\alpha\cos\vartheta\sin\varphi - \sin\alpha\cos\varphi \tag{3.13}$$

thus

$$\begin{aligned} R &\propto |\cos\alpha\cos\vartheta\sin\varphi - \sin\alpha\cos\varphi|^2 \\ &= \frac{\cos^2\vartheta\sin^2\varphi+\cos^2\varphi}{2} + \frac{\cos^2\vartheta\sin^2\varphi+\cos^2\varphi}{2}\sin(2\alpha+\alpha_0) \end{aligned} \tag{3.14}$$

where

$$\alpha_0 = arccos\left(-\frac{\cos\vartheta\sin 2\varphi}{\cos^2\vartheta\sin^2\varphi+\cos^2\varphi}\right) \tag{3.15}$$

The coupling strength is maximized, i.e. the reflectivity depth is minimized, if the relation cos ($2\alpha_{min} + \alpha_0$) = 1 is satisfied in eq. 3.9, where α_{min} is the optimal polarization angle. Thus the following relation can be obtained:

$$\alpha_{min} = \pi - \arctan(\tan\varphi\cos\vartheta_{res}) \tag{3.16}$$

that evidences the relation between polarization and incident and azimuthal angles.

Vector model allowed to understand the consequences of symmetry breaking after azimuthal rotation and provided an analytical expression for the optimal polarization angle which well reproduces the trend of experimental data. Last expression of α_{min} will result extremely useful during the measurements (chapter 4), when it will be necessary to select the incident polarization that optimized the reflectivity depth for sensing purposes. This vector model has been implemented in MATLAB.

3.2 Simulation of gold digital grating through Finite Elements Method (FEM)

The 1D grating geometry is known to support difference resonances mechanism [56] [53] [78], including cavity modes, Wood-Rayleigh anomalies and plasmonic resonances. The simpler geometry allows to perform an optimization process of the geometrical parameters which determine the resonance conditions. By carefully designing the geometry, it is possible to tune a resonance at a precise wavelength. Under certain optical configurations, it is possible to collect a transmitted light signal from the grating through the substrate; this signal can be coupled with common photodiodes to transduce the transmitted light into a current signal [79]. In this way surface refractive index changes on the grating surface due to a functionalization events modify the plasmonic response of the grating itself, leading to a change in the transmission value which can be detected as photodiodes current variations. The optical characterization is focused on far field transmission properties and in particular on polarization dependence of the incident light.

Gold digital grating have been simulated through Finite Elements Method (FEM) in order to identify the best geometry for sensing surface refractive index changes. FEM is a numerical technique for finding approximate solutions to boundary value problems for differential or integral equations. FEM of any problem involves basically four steps [80]:

- discretizing the solution region into a finite number of subregions or elements
- deriving governing equations for a typical element
- assembling of all elements in the solution region
- solving the system of equation obtained.

The method is fully implemented in the commercial software *COMSOL Multiphysics®* version 3.5a, in particular using RF package. In order to minimize computational time, electromagnetic fields distributions have been computed with FEM only in one period of the grating, setting periodic boundary conditions. The simulated system is reported in figure 3.5: only the model that exploits the far-field properties of the transmitted light has been considered. In this configuration, grating substrate (glass)

is optically matched via cedar wood oil to the quartz protection layer of photodiodes array.

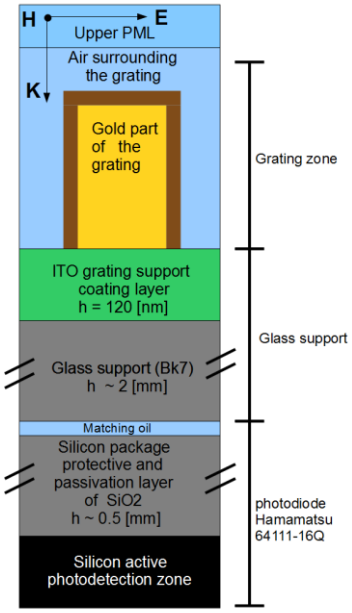

Figure 3.5: Simulated system scheme.

Once defined the geometry, subdomains optical properties, i.e. the refractive indexes or the dielectric constants, and boundary conditions must be defined. The upper condition is provided by the so-called "perfectly matched layer" (PML), that is an additional domain that properly absorbs the incident radiation without producing reflections. The 635 nm wavelength laser lights perpendicularly the grating and, thanks to the periodicity of the structure, SPPs are excited at gold/air interface when the following condition is reached:

$$k_{SPPs} = k_0 \sqrt{\frac{\varepsilon_m \varepsilon_d}{\varepsilon_m + \varepsilon_d}} = m \frac{2\pi}{\Lambda} \tag{3.17}$$

where ε_m=-12.1+*i*1.3 that is the dielectric constant of the gold, ε_d is the dielectric constant of the dielectric over the grating surface (ε_d=1 for the air), $k_0=2\pi/\lambda$ with λ=635 nm, and m is a natural number that indicates the diffraction order. In our analysis we have considered m=1.

The functionalization layer has been simulated as a 1.5 nm homogenous layer over the gold surface, with a refractive index of 1.45. The effect of this layer is to modify the value of ε_d and consequently the SPPs coupling constant of equation 3.15.

Grating geometrical parameters as the period, the duty cycle (ratio between the slits width and the period) and the gold height, have been varied in order to find the grating geometry that maximizes the transmittance variation between bare and functionalized grating, i.e.:

$$\Delta T = T_{func} - T_{bare} \tag{3.18}$$

This transmittance variation will be considered the sensing parameter.

Figure 3.6 shows the simulated transmittance map and the transmittance difference between bare and functionalized grating when it is lighted by TM-mode, fixing the duty cycle at 0.4. The right picture highlights in red the values of the geometrical parameters that maximize ΔT, that are 290 nm for the gold height and 630 nm for the grating period. These geometrical values allow to achieve a transmittance difference of $2x10^{-2}$ a.u. (arbitrary unit) and they will be used for grating fabrication.

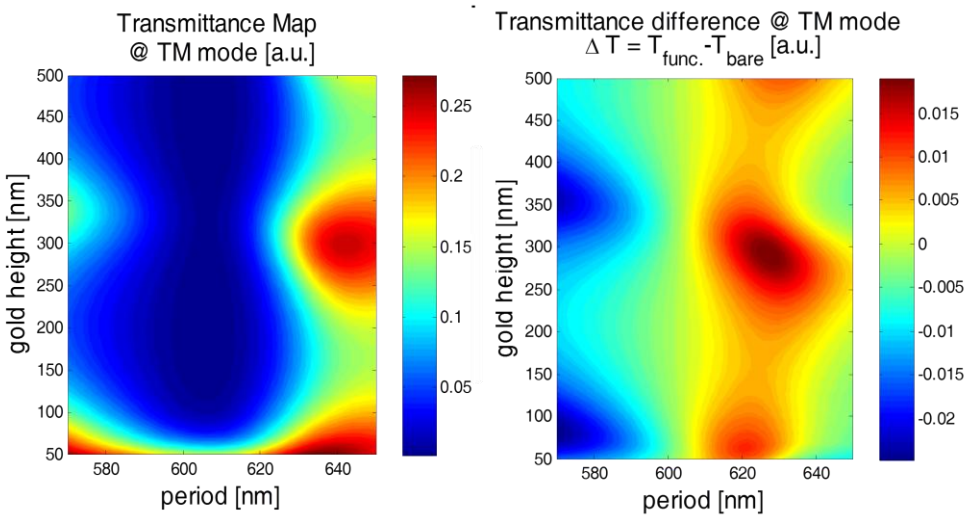

Figure 3.6: (left) Transmittance map at TM-mode as a function of gold height and grating period. (right) Transmittance difference between functionalized and bare grating at TM-mode.

In figure 3.7 the simulated transmission spectra of the grating perpendicularly illuminated are reported. The incepts of the figure show the magnetic field map calculated for different wavelengths. The grating parameters we have considered are a period of 628 nm, a gold height of 290 nm and a duty cycle of 0.4. The transmittance spectra shows typical features of digital grating structures, in particular we can see the presence of two Wood-Rayleigh anomalies, that are abrupt changes in transmission that

occur both in *s*- and *p*-polarization when a diffraction order lies in the plane of the grating, the excitation of SPPs at gold/air interface and a cavity mode.

The first Wood Rayleigh anomaly at 628 nm (magnetic field map reported in the incept (a) in figure 3.7) occurs when incident light wavelength equals the grating period. The second one occurs at 942 nm and it is related to the number of diffracted rays. The transmittance minimum that occurs at 654 nm (incept (b) in figure 3.7) is due to the SPPs excitation at gold-air interface. This excitation causes an absorption of the input light energy that can be seen as a drop of transmittance intensity.

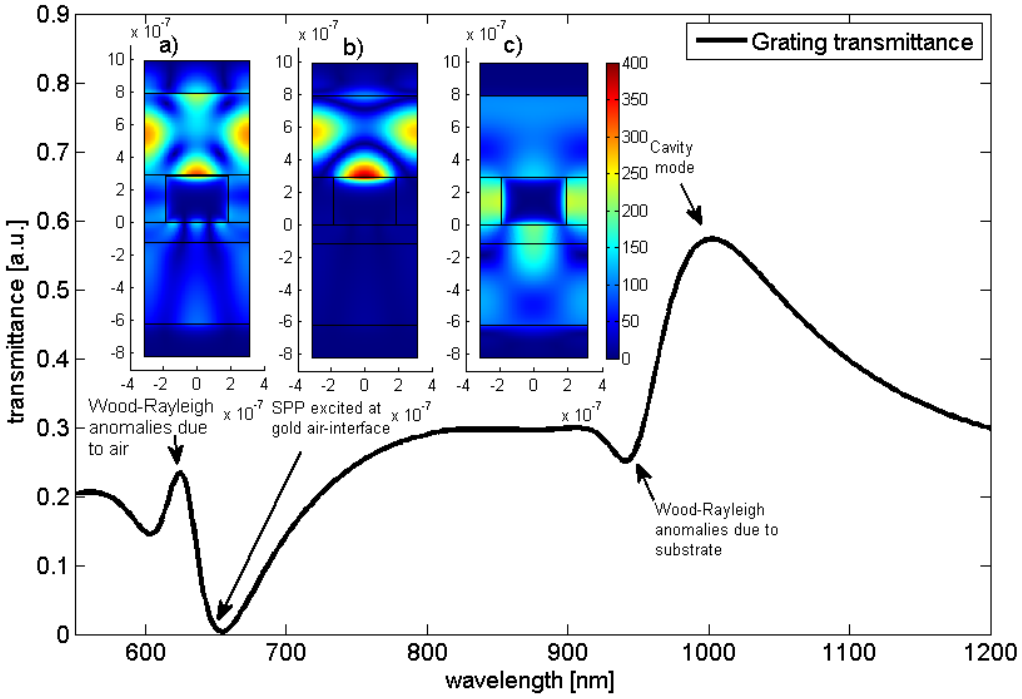

Figure 3.7: Simulated transmittance spectra of a digital grating (628 nm period, 290 nm gold height and 0.4 duty cycle). The incept shows the magnetic field maps of the grating for different wavelength: 628 nm (a), 654 nm (b), 1002 nm (c)

The maximum of transmittance spectrum refers to the excitation of a cavity mode (incept (c) in figure 3.7), that is a single mode Fabry-Perot like-resonance standing inside the slits, which occurs when the phase difference between the different waves transmitted to the substrate is a multiple of 2π, and a maximum in transmittance is observed [53].

The transmittance spectrum of optimized grating in both bare and functionalized state is shown in figure 3.8. The inset points out the spectrum zone in which SPPs excitation occurs (transmittance minimum) and the transmittance difference

is maximized. The presence of the dodecanethiol self-assembled monolayer on gold structure causes a shift of +2 nm of the transmittance minimum related to SPPs excitation.

The figure of transmittance difference as a function of incident p-polarized light wavelength (figure 3.8) shows that the maximum difference is achieved at 635 nm, i.e. our laser wavelength.

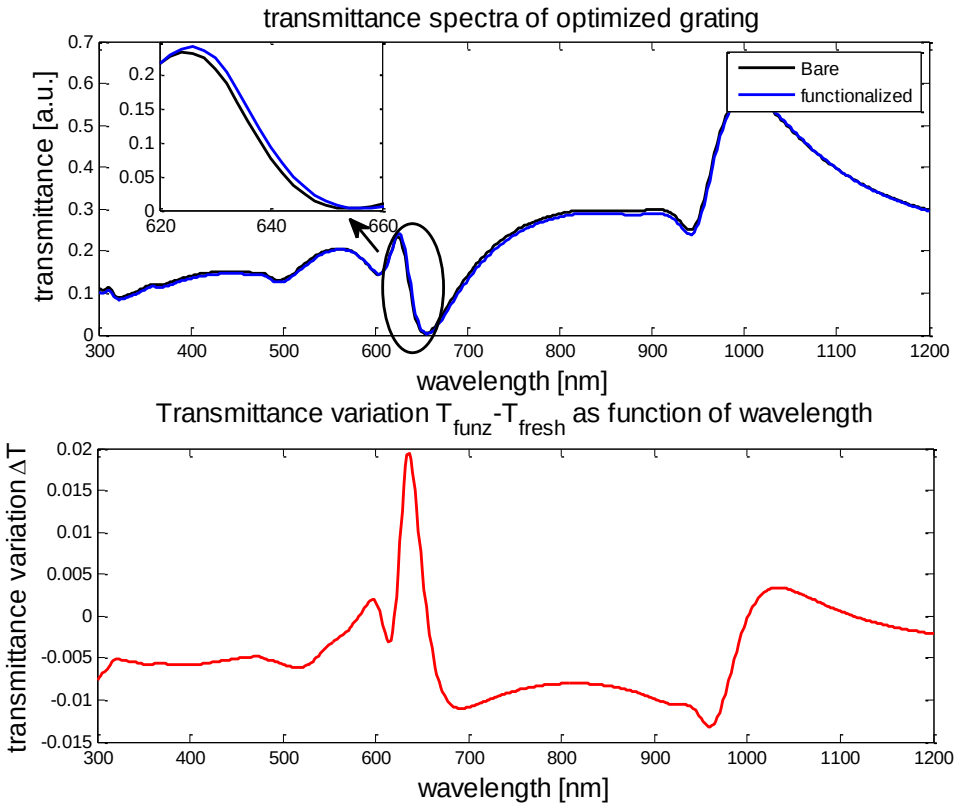

Figure 3.8: Transmittance as a function of incident light wavelength for bare and functionalized grating (upper); the inset shows the SPR region and the wavelength of interest, i.e. 635 nm, that corresponds to the maximum of transmittance between bare and functionalized grating (lower).

3.3 Simulations of silver trapezoidal grating: vector model and Rigorous Coupled-Wave Analysis (RCWA)

The vector model, based on wave vector conservation law and described in section 3.1, has been applied also for the study of silver trapezoidal gratings. This model allows to find the locus of point (ϑ,φ) that satisfies the following surface plasmon resonance condition, obtained from equation 3.4:

$$k_{SPPs}^2 = k_0^2 n_d^2 sin^2\vartheta + 2k_0 n_d mG \sin\vartheta \cos\varphi + m^2 G^2 \qquad (3.19)$$

where n_d is the refractive index of the dielectric, $k_0=2\pi/\lambda$ with λ=635 nm, m is a natural number that indicates the diffraction order and G is the modulus of grating vector.

This equation allows to identify the reflectance minima or the transmittance maxima, and the results for the diffraction orders m=1, -1, -2 are shown in figure 3.9.

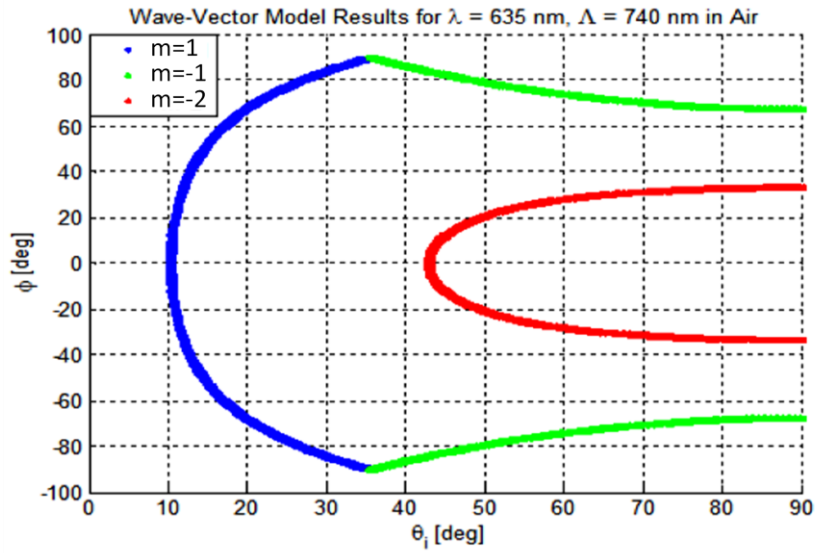

Figure 3.9: Transmittance maxima as a function of azimuth and incident angles for diffraction orders m=1, -1, -2, considering a bare grating in air.

Vector model is a simple tool that allows to identify resonance position with an accuracy that decreases for increasing grating amplitude, i.e. when grating profile must be taken into account in order to properly describe the coupling of the incident light. Moreover, the vector model cannot predict coupling strength and thus it is not able to give a precise estimation of diffracted order weights, e.g. reflectivity or transmission intensity.

Therefore a rigorous approach is necessary in order to exactly solve the problem of a monochromatic plane wave incident on a patterned surface and to simulate the optical response of such multilayered patterned structures. Our group has implemented (in MATLAB) also another more rigorous approach that is the rigorous coupled-wave analysis (RCWA). It is a semi-analytical method in computational electromagnetic that is most typically applied to solve scattering from periodic dielectric structures. It is a Fourier-space method so devices and fields are represented as a sum of spatial harmonics. It is a relatively straightforward, non iterative, deterministic technique. The accuracy of the solution obtained depends solely on the number of terms retained in the space-harmonic expansions of the fields, with conservation of energy always being satisfied [81]. In the technique to analyze the diffraction from surface relief grating structures, the grating is divided into a large number of sufficiently thin planar grating slabs in order to approximate the grating profile with an arbitrary degree of accuracy. The simulated grating structures are shown in figure 3.10, in which the functionalization layer has been considered as a homogeneous layer of fixed refractive index. The number of retained orders has been 85 in Floquet field expansion. The electromagnetic fields in each grating layer are determined by the coupled-wave approach. The electromagnetic boundary conditions (continuity of the tangential electric and magnetic field components) are then applied in sequence at the interfaces among the output region, the individual grating layers, and finally the input region to yield the reflected and the transmitted diffracted field amplitudes and the diffraction efficiencies.

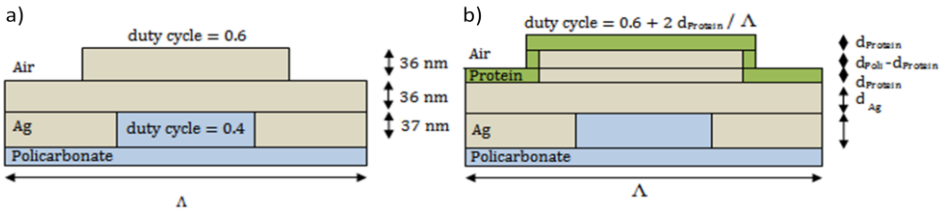

Figure 3.10: Geometry for the grating surface with the planar slabs assumed for the simulation for bare grating (a) and functionalized grating (b).

To model the grating geometry, a period of 740 nm and a silver thickness of 58 nm have been considered. The shape of the grating has been assumed to be trapezoidal with amplitude of 20 nm and ratio between the upper (lower) base and the period of 0.75 (0.93). The silver dielectric constant has been set to -17+0.7*i*, the refractive index of

polycarbonate substrate to 1.58 and the one of air and water respectively of 1 and 1.333.

The percentage difference between baseline signal reflectance and minimum reflectance, i.e., $\frac{R_{bias}-R_{min}}{R_{min}}\%$ obtained from simulation, has been considered as parameter for evaluating the goodness of reflectance signal. Similarly, the percentage difference between baseline signal transmittance and minimum transmittance, i.e. $\frac{T_{max}-T_{bias}}{T_{bias}}\%$ obtained from simulation, has been considered as parameter for evaluating the goodness of transmittance signal. The simulated transmittance parameter is about 700 %, while the reflectance parameter is about 40 %. Analyzing the transmittance signal instead of the reflected ones brings advantages in terms of peak shape.

RCWA allows to calculate transmittance value for each couple (ϑ,φ), and the relative map for bare grating in contact with air is reported in figure 3.11.

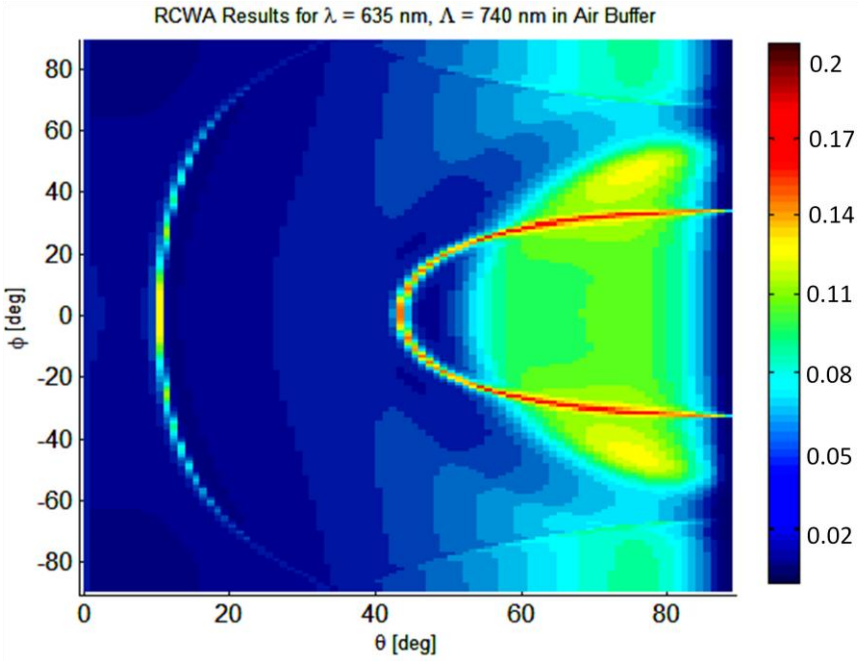

Figure 3.11: RCWA simulated transmittance map as a function of (ϑ,φ)

We can note that the couples (ϑ,φ) related to transmittance maxima in figure 3.11 correspond to the ones obtained with vector model (fig. 3.9).

Fixing an incident angle, the transmittance can be plotted as a function of azimuth angle φ and two symmetric peaks are visible (figure 3.12).

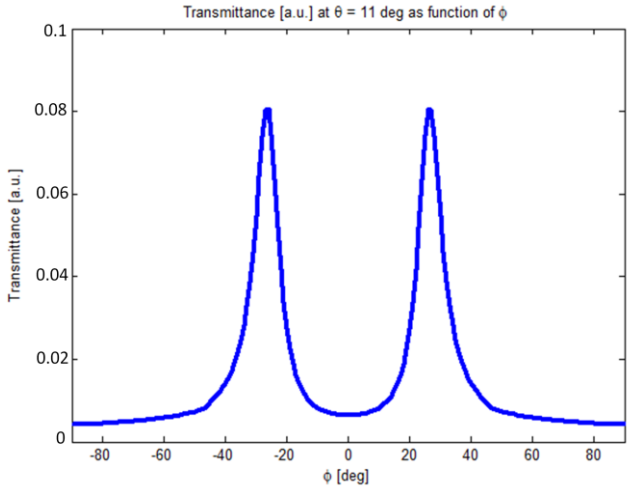

Figure 3.12: Transmittance, considering air as dielectric in contact with the grating, as a function of the azimuth angle φ for a fixed incident angle (ϑ=11 deg) obtained from a section in RCWA map: the two symmetric peaks are due to the first order plasmon

As already mentioned, a functionalization layer over the grating surface modifies the refractive index of the dielectric, and consequently the surface plasmon resonance conditions change, as reported in figure 3.13 where the curve shifts to higher incident angle with the increasing of effective refractive index value.

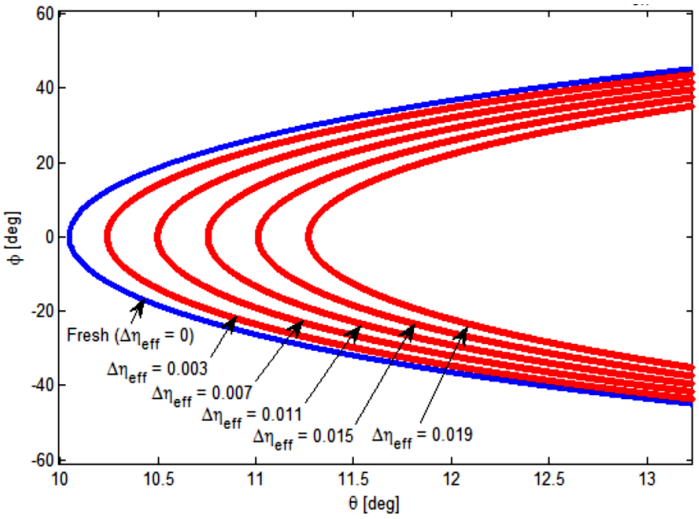

Figure 3.13: Transmittance maxima (vector model) for bare grating (blue line) and different effective refractive index dielectric media (red lines)

The transmittance peaks, for a fixed incident angle, occur at different azimuth angles for bare and functionalized grating, as figure 3.14 shows. The variation of azimuth angle in which resonance peaks occur will be considered the sensing parameter.

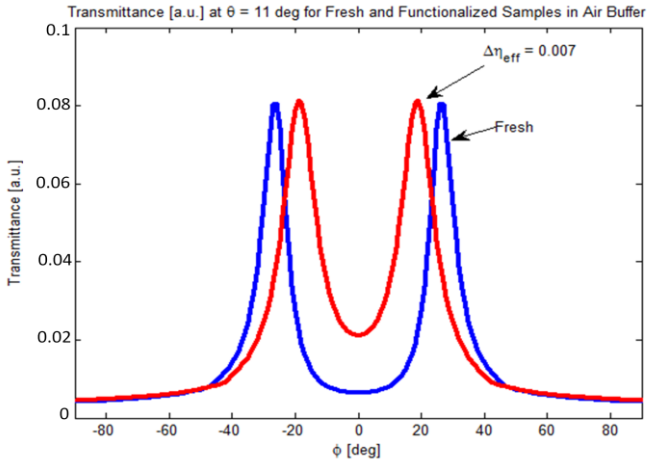

Figure 3.14: Transmittance for a fresh (bare) and a functionalized (Δn_{eff}: 0.007) grating as a function of the azimuth angle φ for a fixed ϑ=11 deg.

The same analysis has been done also considering water as the dielectric medium in contact with grating surface. Figure 3.15 represents the locus of point (ϑ_b,φ), where ϑ_b is the incident angle inside the buffer, of transmittance maxima (or reflectance minima) for different diffractive orders calculated through the vector model.

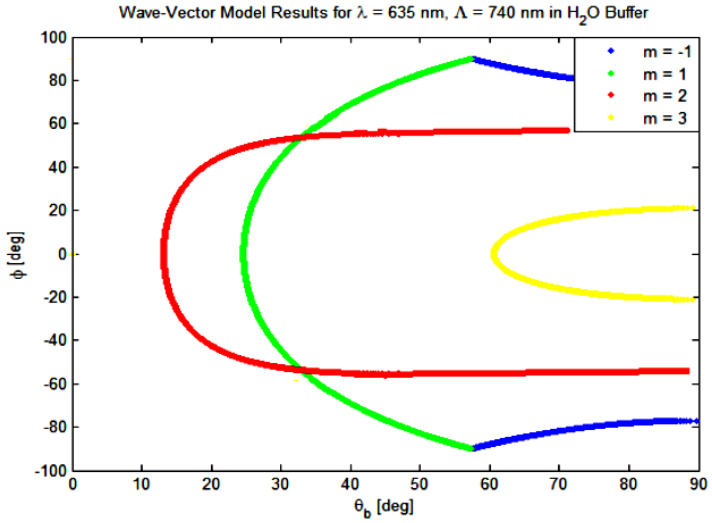

Figure 3.15: Locus of point (ϑ_b,φ) of transmittance maxima computed through vector model, for the diffractive orders m=±1, -2, -3.

The ϑ_b-axis identifies the angle, inside the buffer, for which there is plasmonic excitation: this means that the laser in air has to hit the buffer surface with a $\vartheta_{i,air}$ according to Snell's Law.

Similar results computed via RCWA simulation in (ϑ_b,φ) are reported in figure 3.16. The locus of point of transmittance maxima corresponds to the ones computed through vector model and shown in figure 3.16.

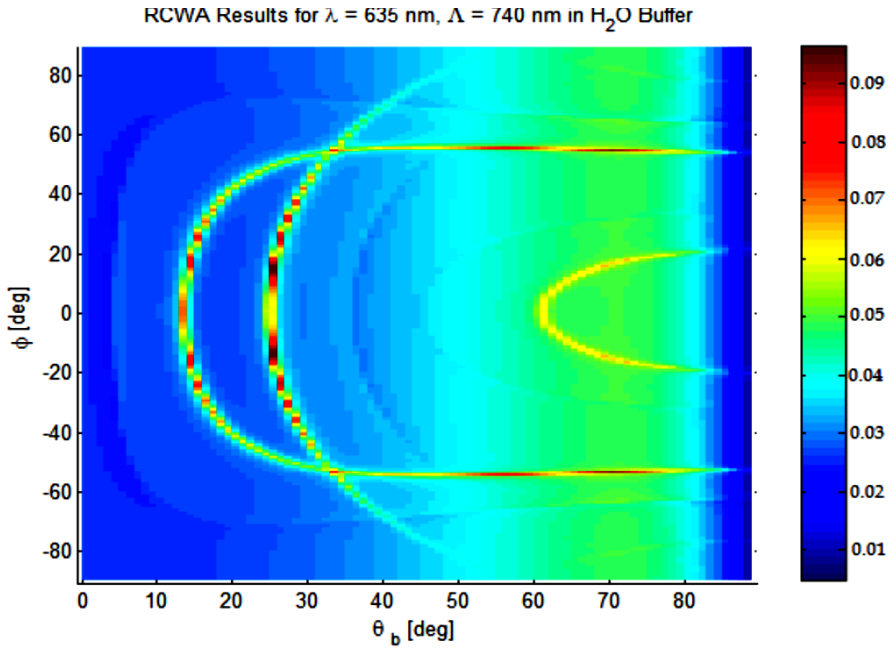

Figure 3.16: Transmittance map as a function of incident and azimuth angles, computed through RCWA, for the diffractive orders m=±1, -2, -3.

The transmittance as a function of azimuth angle for a fixed incident angle ϑ_b (27°) is shown in figure 3.17, and four peaks can be distinguished: the two central peaks are referred to diffracted order m=1 and the two external ones to the order m=-2.

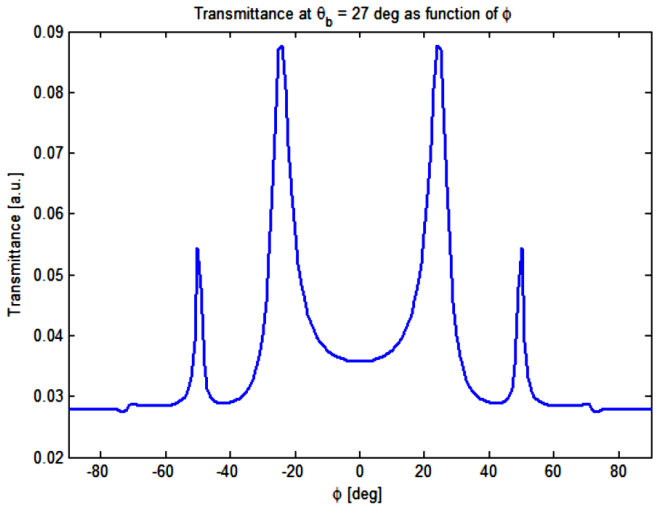

Figure 3.17: Transmittance for a H_2O buffer as function of azimuthal angle for a fixed ϑ_b (27°) obtained from a section of RCWA map.

Evaluating a functionalization layer, the simulated results are analogous to the case in air, in fact a shift towards the right side in the transmittance maxima locus of points due to Δn_{eff} and a change in the φ_{peak} values can be noted (figure 3.18).

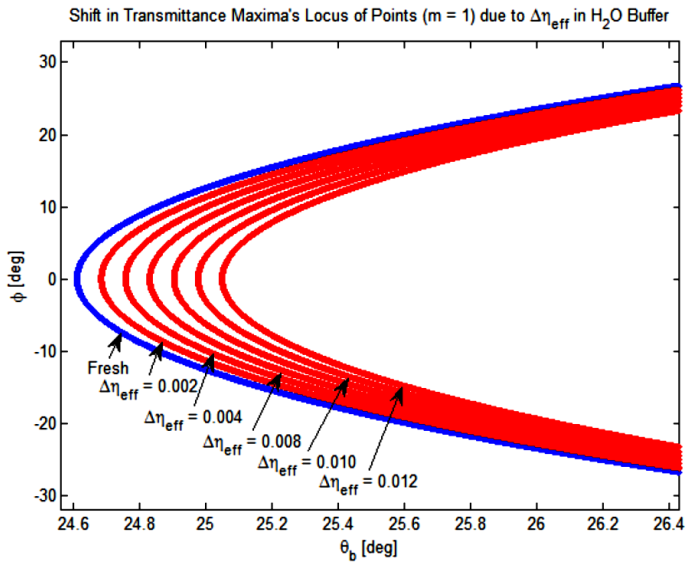

Figure 3.18: Transmittance maxima (vector model) for bare grating in water (blue line) and different effective refractive index dielectric media (red lines)

Then we have represented the azimuth angle variations between bare and functionalized condition for a fixed incidence angle ϑ, as function of bulk refractive index change Δn_{bulk} (figure 3.19), but it can be considered as the effective refractive index change Δn_{eff}. This analysis allows to identify the incident angle that maximizes the azimuth angle variation for a given Δn_{bulk} and consequently the sensitivity.

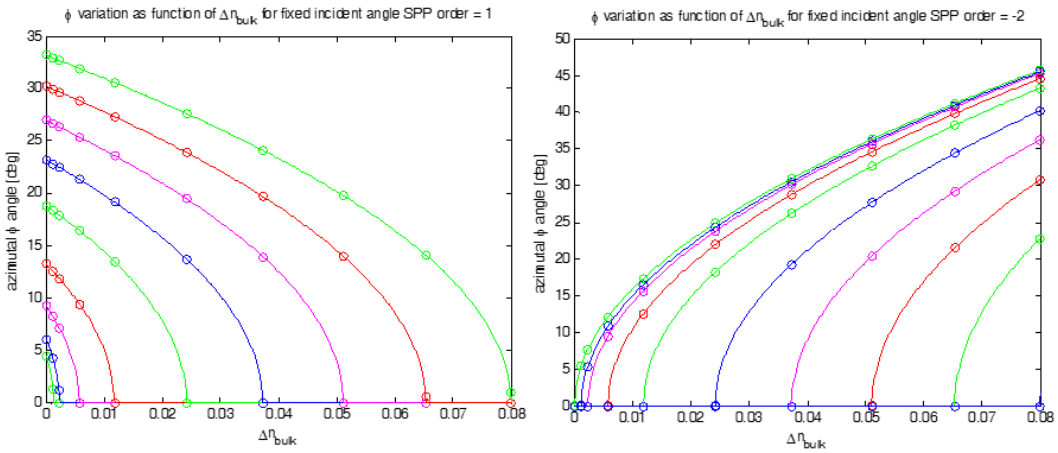

Figure 3.19: Azimuth angle as a function of bulk refractive index variation for different fixed incident angles for SPPs order 1 (on the left) and order -2 (on the right).

Each curve of figure 3.19 corresponds to a particular incident angle ϑ_i; the x-coordinate value of the intersection between the i-th curve and the x-axis represents the highest refractive index variation that can be detected for that particular ϑ_i. The measurement of transmittance as a function of φ (as the one reported in figure 3.14) in this condition reveals only one peak. The relative azimuth angle variation with respect to fresh condition is the curve value at $\Delta n_{bulk}=0$.

Through incident angle optimization, a sensitivity of 2500°/RIU can be theoretically achieved, as in the case of the green line next to the origin of figure 3.19 on the left.

4 Experimental results

In this chapter the results of the different gratings analysis will be presented. Each grating has been optimized for a different analysis so the effect of the various parameters modulations will be exposed and experimentally evaluated.

The results are divided by grating type and a brief introduction explains the measurements protocol and the data processing.

4.1 Measurements of gold sinusoidal grating reflectance

We present a homemade device implementing an innovative SPR technique based on polarization modulation of the incident light. Since the sensing configuration is kept fixed during analysis and the only degree of freedom is represented by incident polarization, the mechanical complexity of the SPR system is significantly reduced with respect to other prism-coupled or grating-coupled SPR devices based on angular or wavelength interrogation. In addition to a simplified architecture, this setup assures great performance in sensitivity and a refractive index resolution which is competitive to commercial SPR systems. The system has been tested both for bulk refractive index analysis and for analytes detection.

4.1.1 Measurement protocol

In this prototype the grating is rotated and kept fixed at the resonance position. The rotating half-wave plate between source and sample allows controlling the incident light polarization. Reflectivity data collected during a polarization scan are fitted with the harmonic relation

$$R_{min} = f_0 - f_1 \cos(2\alpha + \alpha_0) \tag{4.1}$$

and variations of the fitting parameters, e.g. amplitude f_1 or phase α_0, can be considered in order to detect surface functionalization or for solution-concentration analysis, after the system has been properly calibrated. In particular we have consider the phase variation $\Delta\alpha_0$ as sensing parameter.

Figures 4.1 exhibits the data collected for a gold grating with period 500 nm, that has been developed for functionalization and molecules detection process. As figure 4.1b shows, data present a harmonic dependence and are well fitted by the equation 4.1. The resonance incident angle as a function of azimuthal angle is also reported (figure 4.1a) to demonstrate the relation between the two angles, even if in the measurement protocol the incident polar angle ϑ is fixed. In fact, to reduce measurement complexity, ϑ is fixed (40°) in order to have the double surface plasmon polaritons excitation with one wavelength, that has been demonstrated to enhance the sensitivity of one order of magnitude [76] (see section 3.1.1). The inset of figure 4.1a reports the system output as a function of azimuthal angle: this measurement is performed to fix the grating at resonance condition.

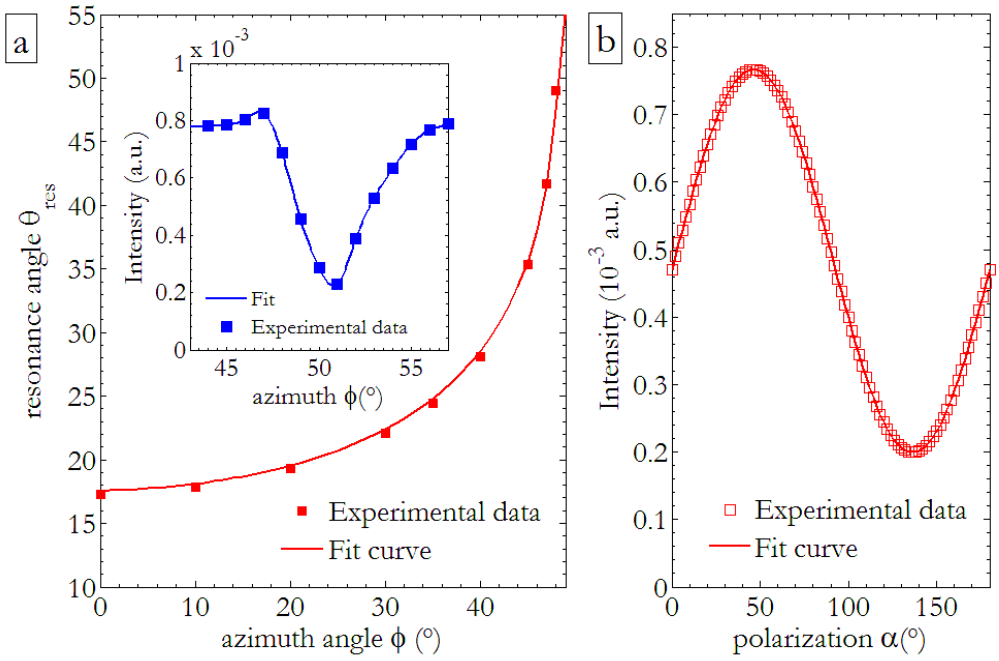

Figure 4.1: Resonance angle ϑ_{res} as a function of the azimuthal rotation angle φ: experimental data and fitting with eq. (1). Data collected with reflectivity analysis of the grating sample mounted on the spectroscopic ellipsometer. In the inset graph: output intensity for azimuthal scan in the range 43°÷57°, 1° step, on the bare grating. Fixed polar angle ϑ = 40°, polarization α= 130°. Data collected with the assembled prototype exploiting polarization-modulation GCSPR. b) Fixed polar angle ϑ = 40°, resonance azimuth φ = 50.4°: polarization scan in the range 0°÷180°, 2° step. Fit curve with eq. 4.1. Grating period 505 nm (AFM analysis)

The typical sensing procedure, performed in the analysis of gold sinusoidal grating, is as follows:

1) The metallic grating is fixed on the rotation sample holder, and it can be embedded either in a custom holder that allows the subsequent functionalization process without removing the sample in the case of analytes detection tests, or in the microfluidic chip in the case of solutions analysis;
2) the incident angle ϑ is selected considering the bare grating and fixed in order to excite high-sensitive SPPs modes (see section 3.1), and polarization is initially fixed at α_{min} (equation 3.14);
3) measurements of the output current at different azimuth angles (1° step) are performed in order to identify precisely the resonance azimuth angle φ_{res} at which the plasmonic dip occurs (figure 4.1, inset graph). The resonance azimuth angle position is finely identified through a weighted centroid algorithm [19]. The azimuth angle is then fixed at resonance azimuth angle position;
4) at the fixed resonance condition, the trend of the output current as a function of the incident polarization is collected (figure 4.1 b) and fitted by the harmonic relation 4.1. Usually 10 repetitions are acquired and only the average is then fitted. Estimations of fitting parameters, in particular the phase term α_0, are collected.
5) the polarization scan is repeated after the functionalization or sensing process or in presence of a different concentration solution.

This protocol allows to reduce the measurement complexity identifying the shift of phase term $\Delta\alpha_0$ as the only sensing parameter.

4.1.2 Response to bulk variations of refractive index: analysis of saline solutions

In order to estimate sensor sensitivity, measurements of bulk solutions with different refractive indexes have been performed. For analysis in aqueous liquid solution the gratings of period 400 nm has been considered, in order to analyze the resonance order m=-1 as in the case of the 500 nm grating in air.

The metallic grating was embedded in the pre-fabricated microfluidic cell (see section 2.4) and fixed to the sample-holder. After setting the incident angle ϑ at 40°, measurements of the output current at different azimuth angles were performed in order to identify the position of the resonance azimuth φ_{res}. For the fixed polar angle $\vartheta = 40°$, the reflectivity minimum is located at $\varphi_{res} = 59.5°$. At the fixed resonance condition, the trend of the output current as a function of the incident polarization was recorded for saline solutions of increasing sodium-chloride concentration (0 - 0.15 - 0.30 - 0.60 - 0.90 g of NaCl in 10 ml of double-distilled water) flowing through the cell (Fig. 4.2 a). The refractive index variation for each sodium-chloride concentration is reported in table 4.1 [82] [83].

The polarization angle was varied in the range 0°÷180°, that is a harmonic period, collecting 2060 points in a time of about 2.5 minutes (estimated rate ~ 11.4 pts/sec). Output data as a function of polarization were fitted with a least square algorithm, implemented in MATLAB, using equation 4.1 in order to estimate the phase shifts $\Delta\alpha_0$ (Fig. 4.2 b) and their corresponding errors σ_α.

Fitting results are shown in figures 4.2 and we can see that the harmonic curve shifts to higher polarization angles as the sodium-chlorite concentration increases.

NaCl dissolved in 10 ml of water [g]	**Refractive index of solution [RIU]**
0	1.3330
0.15	1.3357
0.3	1.3384
0.6	1.3438
0.9	1.3492

Table 4.1: Relation between NaCl concentration dissolved in water and the refractive index of the solution

The same measurements were performed numerically by our colleagues of LaNN laboratory with the Chandezon's algorithm [84] and the phase shift was computed for variations of the dielectric permittivity of the water environment from 1.77 to 1.83, step 0.007. Simulated shifts and experimental data are both reported in Fig. 4.2b and we can see that they are in good agreement.

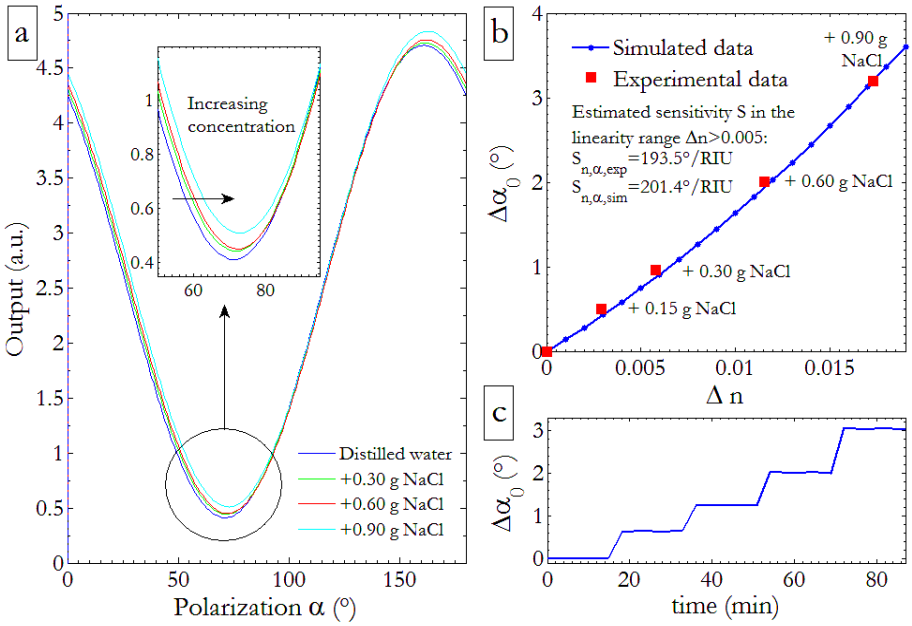

Figure 4.2: (a) Output intensity of polarization-scan curves in the range 0°÷180°, 2060 points, collected for increasing sodium-chloride concentration in the double-distilled water solutions flowing through the cell (0 – 0.15 – 0.30 – 0.60 – 0.90 g / 10 ml) . In the inset graph: detail of the curve shift. (b) Phase shift $\Delta\alpha_0$ (°) as a function of the bulk refractive index variation Δn: experimental data (red squared markers) and simulation results with Chandezon's method (blue dotted points). (c) Phase shift signal as a function of time. (Refractive index range: 1.33÷1.35)

The phase shifts obtained from the data fitting are reported in table 4.2, considering the correspondent refractive index variation.

Refractive index variation Δn [RIU]	**Phase shift $\Delta\alpha_0$ [°]**
0.0027	0.5367±0.0001
0.0054	1.1125±0.0002
0.0108	2.1805±0.0002
0.0162	3.1912±0.0002

Table 4.2: Phase shift values experimentally measured and the relative refractive index variation of the solution with respect to pure water

After calculating the experimental variation Δn of the refractive index with respect to pure water from the corresponding saline concentration [82] [83], it is possible to give an estimation of the phase sensitivity $S_{n,\alpha} = \Delta\alpha_0/\Delta n$ (Fig. 4.2 b) and to

calculate the refractive index resolution $\sigma_{n,\alpha} = \sigma_\alpha / S_{n,\alpha}$. Both $\Delta\alpha_0$ and σ_α are obtained from harmonic curve fitting. As figure 4.2b shows, there is a clear region of linearity after a refractive index variation of 0.005 RIU (Refractive Index Unit). By considering an average experimental sensitivity $S_{n,\alpha,exp} \sim 193.5$ °/RIU and the *a posteriori* error on phase $\sigma_\alpha \sim 1 \div 2 \cdot 10^{-4}$ degrees, the estimated refractive index resolution is around $\sigma_{n,\alpha} \sim 5 \cdot 10^{-7} \div 1 \cdot 10^{-6}$ RIU. The analysis of numerical data provides a slightly higher value for refractive index sensitivity, $S_{n,\alpha,sim} \sim 201.4$ °/RIU, so the experimental results are comparable to simulation one.

4.1.3 Measurements of surface variations of refractive index: detection of bio-analytes

The aim of a biosensor is to detect and quantify the presence of a specific analyte in a biological sample. The detection selectivity is given by the biorecognition molecules immobilized over the sensor active area, that must bind to the molecules of interest and avoid non-specific binding.

The GCSPR system developed has been tested for the detection of two biological molecules, that are the avidin and a DNA chain, and the results are summarized in the following sections.

4.1.3.1 Avidin detection

A grating with period around 500 nm was fixed on the rotation sample holder by using a custom socket, that allows to functionalize the sample without removing it from the stage. Afterwards, measurements of the output current at different azimuth angles were performed in order to identify the resonance azimuth angle φ_{res} at which the plasmonic dip occurs. For the fixed polar angle $\vartheta = 40°$, the reflectivity minimum is located at $\varphi_{res} = 50.4°$ and the azimuthal angle is fixed at this value. At the fixed resonance condition, the trend of the output current as a function of the incident polarization was collected in air (Fig. 4.3b) and well fitted by the harmonic curve of equation 4.1. The polarization angle was varied in the range 0°÷180°, collecting 2060 points, and the scan was performed before and after the deposition of the antifouling

biotin-PEO-Cysteine (b-PEO-Cys) biorecognizer layer and then after the addition of the avidin solution in order to test the detection of the protein as a polarization shift of the output sinusoid (Fig. 4.3).

Output data as a function of polarization were fitted with a least square algorithm using equation 4.1 in order to estimate the phase shifts $\Delta\alpha_0$ and their corresponding errors σ_α (Fig. 4.4). The deposition of the b-PEO-Cys layer results in a phase shift $\Delta\alpha_{0,PEO}$ = 0.5324 ± 0.0004°, that is a low value but higher than the measurement error found in bench characterization (0.12°). The binding of the avidin to the biotin-end of the biorecognizer layer causes a further phase shift $\Delta\alpha_{0,Avi}$ = 2.2024 ± 0.0004°.

By modelling the effective refractive index change Δn_{eff} with an effective medium approximation method (see section 2.3), it is possible to estimate the corresponding phase sensitivity $S_{n,\alpha}$ and to calculate the refractive index resolution $\sigma_{n,\alpha}$= σ_α /$S_{n,\alpha}$. The antifouling b-PEO-Cys layer is assumed to form a packed monolayer with refractive index n_{PEO}= 1.47 [85].

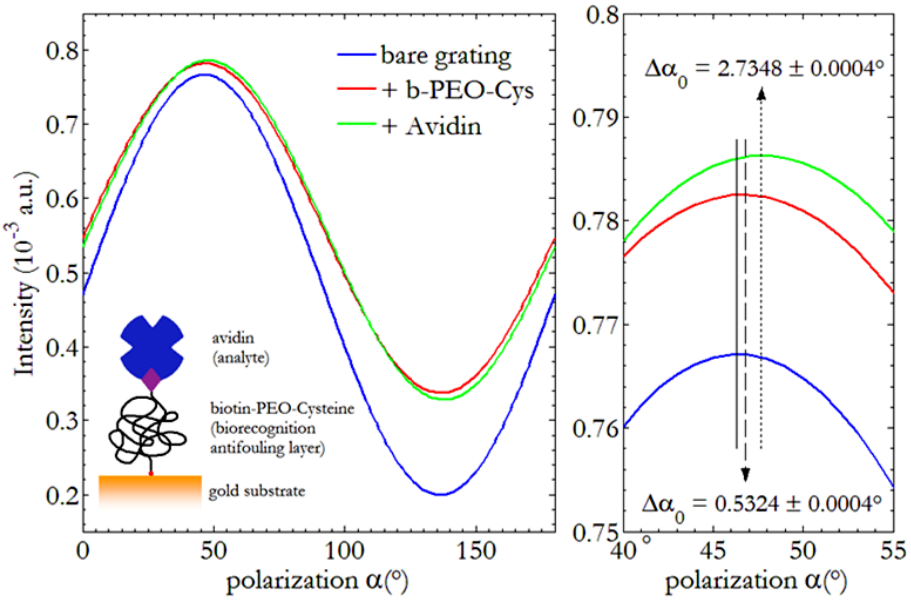

Figure 4.3: Output intensity for a polarization scan in the range 0°÷180° on the bare grating (blue line), after coating with biotin-PEO-Cysteine (b-PEO-Cys) biorecognizer layer (red line), after avidin detection (green line). Fixed polar and azimuthal angles: ϑ = 40°, φ = 50.4°. Incident wavelength λ = 635 nm. Details of the phase shift. Grating period 505 nm (AFM analysis).

In order to get an estimation of the layer thickness, a flat gold sample was functionalized following the same procedure and analyzed with spectroscopic ellipsometry. Collected data were fitted by means of the ellipsometer software package WVASE32 (J. A. Woollam) considering a Cauchy model for the b-PEO-Cys monolayer in the optical range with Urbach tail adsorption [86]. Reflectivity measurements of the grating samples in water environment were performed in the range 15°÷45°, step size 0.2° at the incident wavelength λ = 800 nm. The resulting thickness is d_{PEO} = 2.21 ± 0.04 nm. The same analysis was performed after exposition to avidin solution for the proper time. The adsorbed analyte is supposed to form a thin monolayer with refractive index n_{Avi} = 1.45 and the thickness from ellipsometric analysis is around d_{Avi} = 2.36 ± 0.04 nm, for a total thickness of the coating layer $d_{PEO+Avi}$ = 4.57 ± 0.08 nm. The consequent effective index variations, calculated with the effective medium approach (EMA), are $\Delta n_{eff,PEO}$ = 75.5·10^{-4} RIU and $\Delta n_{eff,Avi}$ = 79.2 ·10^{-4}RIU respectively for PEO and avidin grating detection.

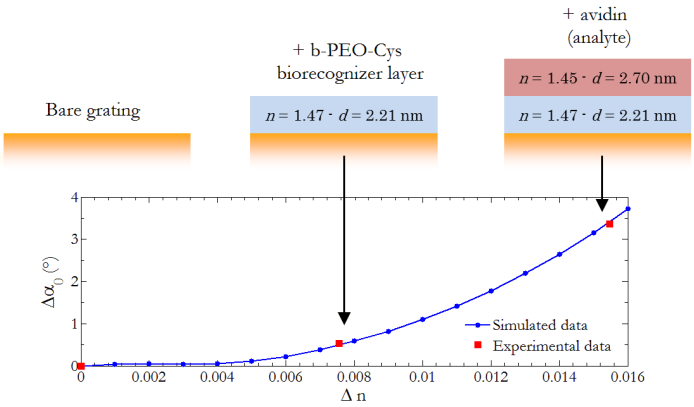

Figure 4.4: Phase shift $\Delta\alpha_0$ as a function of the corresponding effective refractive index variation Δn_{eff}, after coating with a biotin-PEO-Cysteine (b-PEO-Cys) biorecognizer layer ($\Delta n_{eff,PEO}$ = 7.55 · 10^{-3} RIU) and after avidin detection ($\Delta n_{eff,PEO+Avi}$ = 15.48 · 10^{-3} RIU). Experimental data (red squared markers) and simulation results (blue dotted points).

The sensitivity of the whole sensing platform is given by $S_{n,\alpha} = \Delta\alpha_{0,Avi}/\Delta n_{eff,Avi}$ = 278.09°/RIU, with a refractive index resolution around $\sigma_{n,\alpha}$ = 1 · 10^{-6} RIU. Experimental points of the phase shifts after grating PEO-grafting and avidin detection are well fitted by the simulated curve (see Fig. 4.4). The theoretical trend provided by simulations allows calculating an estimation of refractive index sensitivity in properly selected ranges of linearity. In the range 0.005 < Δn < 0.010, for instance, we get an estimate

sensitivity $S_{n,\alpha}$ = 240°/RIU, while in the range 0.011 < Δn < 0.018 sensitivity rises up to 622 °/RIU, with an estimated resolution around $3 \cdot 10^{-7}$ RIU [87] [88].

After avidin detection, an azimuthal scan was performed, in order to evaluate the peak azimuthal angle shift, that is around 1° (as shown in figure 4.5), that is lower that the correspondent phase shift value above reported. This proves that the gold sinusoidal grating has been optimized for polarization modulation.

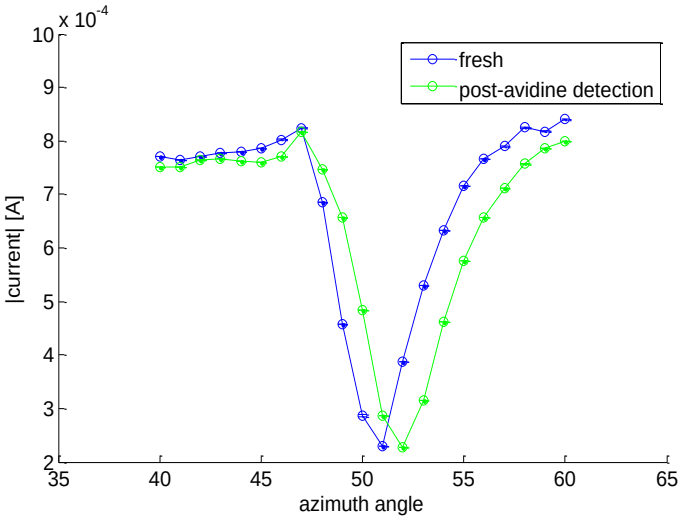

Figure 4.5: Measured current as a function of azimuth angle before and after biotin-PEO-Cysteine (b-PEO-Cys) biorecognizer layer

4.1.3.2 DNA detection

The gold sinusoidal grating has been also tested for the detection of a DNA chain [89], exploiting a DNA analogous with superior properties than DNA itself, that is the Peptide Nucleic Acids (PNAs), pseudopeptide nucleic acid structural mimics (see section 2.3). The analysis is similar to the avidin detection one.

An optimized gold grating with period of 500 nm was fixed on the sample holder with the laser bench at a polar angle ϑ = 40° and the azimuth resonance angle was identified through a preliminary measurement and then fixed at the dip position. Therefore a polarization scan was collected in the range 0°÷180° before and after the deposition of the HS-PNA recognizer layer with the antifouling HS-PEG capping layer; moreover the same scan was performed after the addition of the DNA target solution. Data are reported in figure 4.6.

The functionalization process causes a low phase shift $\Delta\alpha_{0,funct}$ = 0.810 ± 0.002°, that is greater than the measurements error (0.12°) found in the bench characterization (section 2.2.3), proving that the shift is due to the functionalization layer. On the contrary the binding of the DNA to the PNA-probe of the biorecognizer layer causes a phase shift $\Delta\alpha_{0,DNA}$ = 3.162 ± 0.001° [89].

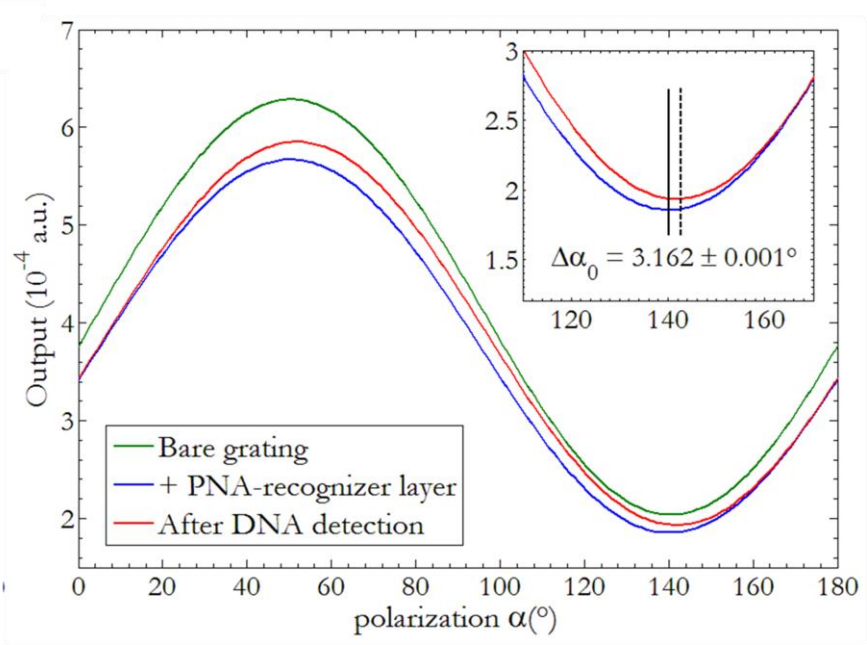

Figure 4.6: Output intensity for a polarization scan in the range 0°÷180° on the bare grating (green line), after coating with HS-PNA biorecognizer layer with antifouling PEG (blue line), after DNA detection (red line). Fixed polar and azimuthal angles: ϑ = 40°, φ= 54.5°. Incident wavelength λ = 635 nm. In the inset graph details of the detection shift.

In order to get an estimation of the layer thickness, a flat gold sample was grafted following the same procedure and analyzed with spectroscopic ellipsometry, as in the previous detection test. The thickness of the PNA-probe layer is around 1.5 nm and after DNA-binding the whole thickness increases to about 4 nm. Assuming an average refractive index n_{DNA} = 1.45 [90], the estimated effective refractive index variation is $\Delta n_{eff,DNA} = 77 \cdot 10^{-4}$ RIU, and the estimated sensitivity of the DNA sensing platform is $S_{n,\alpha} = \Delta\alpha_{0,DNA}/\Delta n_{eff,DNA}$ = 410°/RIU, with a refractive index resolution around $\sigma_{n,\alpha} = 2.5 \cdot 10^{-6}$ RIU. Sensitivity and resolution obtained in these experiments are comparable to the ones reported in literature (section 1.3.3). The estimated resolution could be further improved up to at least one order of magnitude with the use of a low-

noise photodetector with a greater signal-to-noise ratio or by further increasing data statistics with a shorter angular step of the polarization scan.

The advantage of this system is that provides a sensing architecture which is much more suitable to miniaturization than other techniques based for instance on angular or wavelength interrogation, and the performed experiments prove the system ability in sensing applications.

4.2 Measurements of gold digital grating transmittance

In this section experimental results of the gold digital grating are presented. The focus of the measurements is to verify if the developed system is capable to detect surface refractive index changes as transmittance variations when grating is lighted in TM-mode, as previously discussed in 3.2. The measurements results will be analyzed and compared to simulations ones.

4.2.1 Measurement protocol

The set-up for the gold digital grating is described in section 2.2.2. Gratings are perpendicularly lighted by the laser beam and their characterization consists of transmittance measurements as a function of incoming light polarization. In fact, refractive index changes can be evaluated as transmittance variation when incoming light is in TM-mode, since SPPs are excited in this condition. Measurement protocol consists of the following steps:

1) Grating are positioned over the photodiodes array, optically matched thanks to an appropriate oil (refractive index n=1.5) in order to avoid refractive index variations between the Bk7 glass and the fused silica photodiode protective layer, that could introduce artifacts in the measurements.
2) The polarized laser beam passes through the half wave plate mounted on the motorized rotation stage, so incident light polarization can be varied by properly rotating this lens. Fifty measurements for each condition have been performed with a sampling step of 0.1°. For each polarization angle 20 points have been acquired and only the mean value between them has been recorded. Transmittance is obtained normalizing the measured current value with the one measured when laser directly lights the photodiodes array.
3) The polarization scan is repeated after the functionalization process.

The functionalization process, aimed to immobilize dodecanethiol on grating surface, has been performed by drop-casting method without remove the sample from the photodiodes by using a custom socket, in order to avoid positioning errors.

Grating transmittance has been measured before and after dodecanethiol immobilization. Ellipsometric measurements have been also taken as control through an ellipsometer (J.A. Woollam Co VASE), impinging perpendicularly the grating surface with a TM polarized light and varying the light wavelength with a step of 2 nm. Its transmittance value is related to the order-zero transmittance ray which is the only one collected by the ellipsometer detector.

4.2.2 Measurements of surface refractive index variations

The capability of the system to detect refractive index variations has been evaluated through a functionalization with dodecanethiol (see section 2.3, "Alkanethiols"). Measurements of bare and functionalized gratings have been performed through the developed bench, and ellipsometric measurements have been done as control.

Figure 4.7 shows the transmittance spectra of the bare and functionalized grating measured through the ellipsometer.

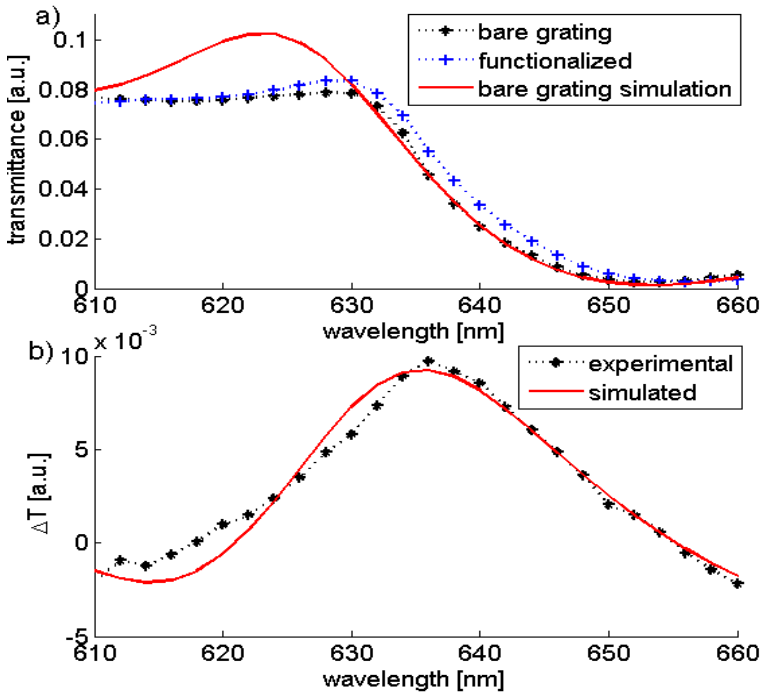

Figure 4.7: Experimental transmission spectra of bare and functionalized grating with the simulated fresh condition (a), and comparison between experimental and simulated ΔT (b)

We can see from figure 4.7 that experimental results, concerning the bare case, are well fitted by simulation, as well as the experimental ΔT parameter reported in figure 4.7 b. We measured a shift of 2 nm in the minimum of transmittance due to SPPs resonance condition change, in agreement with simulation results (see section 3.2).

Figure 4.8 shows an example of grating transmittance as a function of incoming light polarization angle measured with the optical test bench we have developed, for both bare and functionalized grating.

As we can see from the curves, the transmittance presents a harmonic dependence on polarization angle.

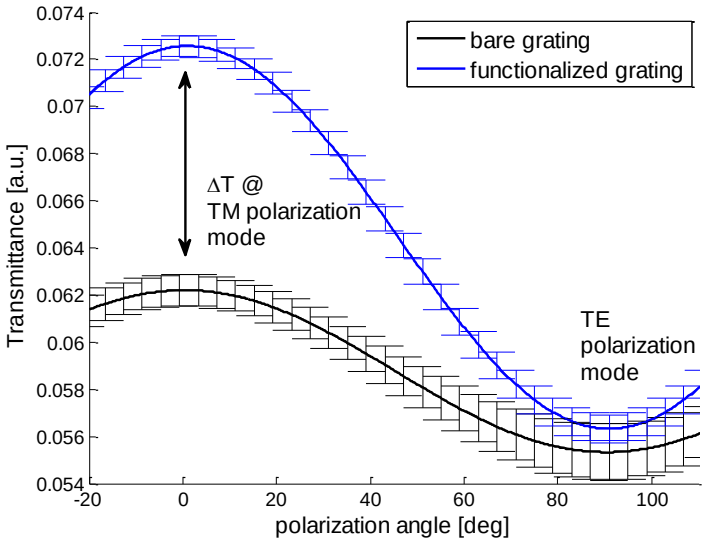

Figure 4.8: Mean and standard deviation of measured transmittance as a function of incoming light polarization (TM-mode=0°; TE-mode=90°)

A transmittance variation of ΔT = 0.01 a.u. has been measured between the bare and functionalized condition only when input light polarization is in TM mode, in accordance to the fact that SPPs are excited only by *p*-polarized waves. Since the orientation of grating slits respect to the photodiodes array geometry permits only the order-zero ray detection, transmittance variation value could be compared with the one obtained by ellipsometry measurement. The two results are in good agreement and they are comparable with the simulation one.

The error bars reported in figure 4.8 are mainly due to laser intensity variation, as discussed in section 2.2.3, and refers to 50 measurements of transmittance as function of polarization angle.

Moreover we can estimate the sensitivity and the resolution of the developed grating-coupled system. From simulation we have calculated that a shift of 2 nm in the SPPs resonance minimum corresponds to an effective refraction index variation of 0.0034 RIU. The sensitivity can be estimated in terms of $S=\Delta T/RIU$ and a value of 2.94 a.u./RIU is found. Resolution of our sensor can be estimated by considering the error bars in figure 4.8. Since the error bars values is about 6.6×10^{-4} a.u., resolution is 2.24×10^{-4} RIU that has a great value in comparison to other types of sensor [7] but it could be reduced by using laser with a more stable intensity. Nevertheless we have demonstrated that a simple and compact system based on EOT can detect the presence of a thin dodecanethiol SAM.

The proposed system has a simple measurement protocol and it is suitable for multiplexing and miniaturization. Its ability to detect a dodecanethiol SAM, which is a very thin layer respect to a protein or a DNA layer, let us suppose that such type of system could be used on large scale for bio-recognition applications.

4.3 Measurements of silver trapezoidal grating transmittance

Silver trapezoidal grating has been developed and analyzed by our research group in collaboration with the Spin-Off of the University of Padova Next Step Engineering. The bare grating behavior has been deeply analyzed in azimuthal angle modulation, optimizing the incoming light incident angle in order to enhance the sensor sensitivity.

A bare grating characterization will be discussed in detail and then the GCSPR system capability to detect refractive index variations has been analyzed through both SAM layers and solutions with increasing refractive indexes.

4.3.1 Measurement protocol

Silver trapezoidal grating has been analyzed modulating the azimuthal angle φ and fixing the incident angle and the *p*-polarization.

The choice of the incoming light incident angle ϑ has a central role in sensor sensitivity, since the azimuthal angle variation depends on it. If the refractive index to be detected is known, the transmittance peaks as a function of (ϑ,φ) can be simulated and the incident angle that maximizes the azimuthal angle variation Δφ, with respect to the bare grating, can be identified (figure 4.9). For this angle, the functionalized grating transmittance as a function of φ presents only one peak.

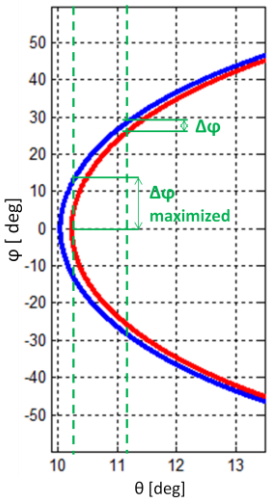

Figure 4.9: Transmittance maxima as a function of azimuthal φ and incident ϑ angle for bare (blue line) and functionalized (red line) grating. In green the relative azimuthal angle variation Δφ is enlightened for a non-optimized incident angle and an optimized one

The typical measurement protocol consists of the following steps:

1) the sample is positioned over the photodiodes array using the matching oil to ensure optical matching between the grating and the photodiodes.
2) Incident light polarization has been fixed in TM mode.
3) The incident angle is fixed considering the SPPs order to analyze, in the case of bare grating characterization, and the refractive index variation to detect, in the case of sensing test.
4) Transmitted light is then acquired varying the azimuthal angle (range: -60°÷+60°, 1500 points) through the motorized rotation stage. Transmittance is obtained normalizing the measured current value with the one measured when laser directly lights the photodiodes array.
5) To eliminate the error on the azimuth angle introduced by the manual positioning of the grating over the photodiodes, the measured signals are shifted exploiting the peak symmetry with respect to φ=0°, and then the peak azimuth angle is identified.

The azimuthal angle variation Δφ has been considered the sensing parameter for surface refractive index changes.

4.3.2 Bare grating characterization

Since the silver trapezoidal grating has been developed in collaboration with Next Step Engineering s.r.l. through an industrial process, a preliminary grating characterization has been performed varying some fabrication parameters as the temperature of plastic molder and the optical density of the metallic layer, related to silver thickness. This analysis has been done in order to identify the fabrication parameters that allow the best plasmonic signal in terms of transmittance variation between resonance peak and baseline, i.e.:

$$\Delta T\% = \frac{T_{\varphi_{peak}} - T_{\varphi_{=0°}}}{T_{\varphi_{=0°}}} 100 \tag{4.2}$$

Ten fresh measurements have been performed on ten samples for each of six different molding temperatures, that are identified with different codes (T1÷T6, T1 is the lowest and T6 the highest temperature). Temperatures and specific details are not specified for confidential agreements with Next Step Engineering. The idea was that the

molding temperature could affect grating geometry, especially grating height, since it affects the plastic viscosity. Figure 4.10 shows transmittance measurements of the all the samples as a function of azimuthal angle. The corresponding positive peak azimuthal angles, as a function of the temperatures, are reported in figure 4.11 and a decreasing of angle value with the temperature increasing can be noted. Only the positive peak has been analyzed, since transmittance curves are symmetric with respect of null azimuthal angle.

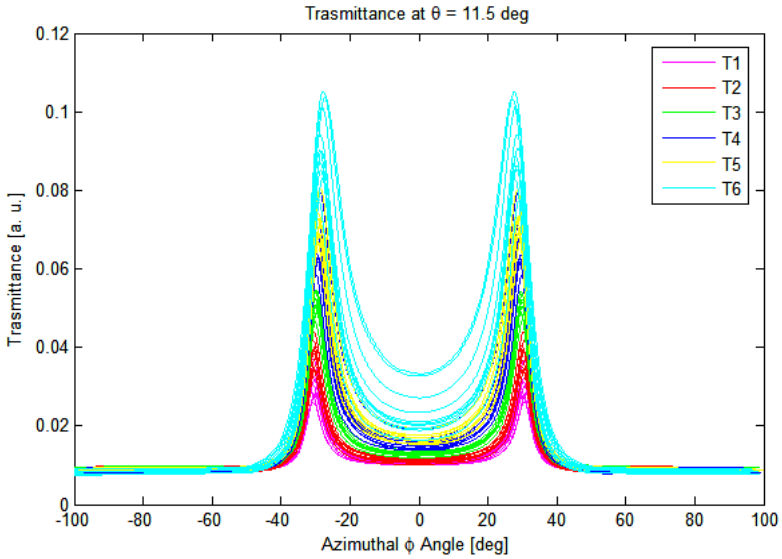

Figure 4.10: Transmittance as a function of azimuthal angle, with ϑ=11.5°, for the different molding temperatures.

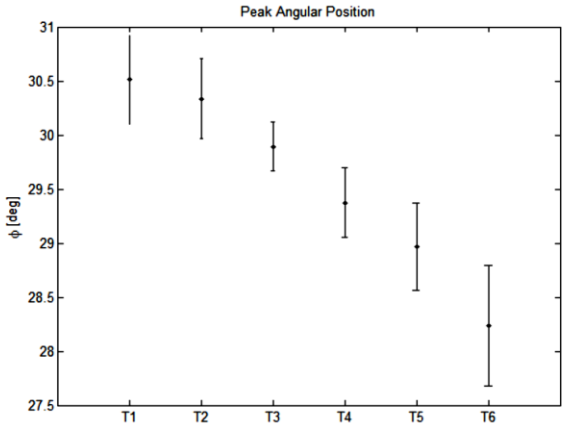

Figure 4.11: Mean and standard deviation of positive peak azimuthal angular position for the different temperatures.

The transmittance value at peak and at null azimuthal angle for the various temperatures analyzed is shown in figure 4.12: in this case we can note that the transmittance increases with the temperature.

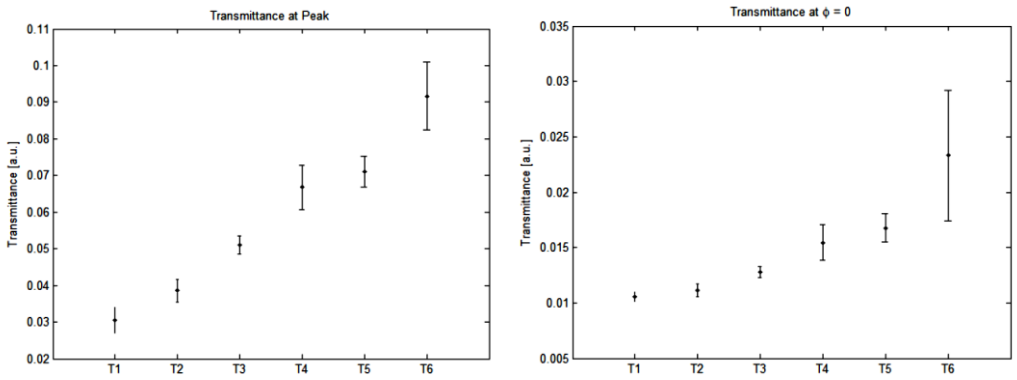

Figure 4.12: Mean and standard deviation of transmittance at peak (left) and at null azimuthal angle (right) for the different temperatures.

Evaluating the transmittance percentage variation (equation 4.2), T4, T5 and T6 temperatures present higher variation between baseline in φ= 0° and φ_{peak} with respect to the other temperatures (Table 4.3). T5 devices show a lower standard deviation from the computed mean value for both transmittance at peak and at φ= 0° than the other temperatures under analysis, that means a higher devices reproducibility. Therefore T5 temperature has been employed for gratings fabrication.

Temperature	**ΔT %**
T1	166
T2	213
T3	266
T4	287
T5	288
T6	273

Table 4.3: Percentage transmittance variation calculated from ten devices for each fabrication temperature

Once the best molding temperature has been chosen, we have performed an analogous analysis for five different optical densities of the metal layer, identified through the codes O.D.1÷O.D.5 (O.D.1 is the lowest optical density, O.D.5 the highest),

in order to select the one that implies the highest percentage transmittance variation. The values obtained are reported in table 4.4. The metal layers that correspond to O.D.1 and O.D.2 are too thin and resonance peaks are difficult to be distinguished.

Temperature	ΔT %
O.D.1	-
O.D.2	-
O.D.3	73
O.D.4	186
O.D.5	280

Table 4.4: Percentage transmittance variation calculated from ten devices for each silver layer optical density

The variability of resonance azimuth angle within a single device and between different devices has been studied by measuring sixteen spots for each of nine different gratings (figure 4.13). The maximum standard deviation within a grating is 0.32° whilst the variability between different devices is higher and reaches 1.8°.

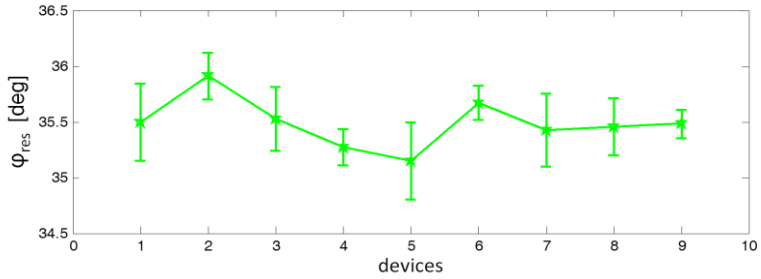

Figure 4.13: Mean and standard deviation of resonance azimuth angle for nine devices. For each device 16 spots have been measured.

Once defined fabrication process parameters, SPPs excitation of bare grating has been experimentally analyzed in azimuth angle modulation. The effect of SPPs excitation on transmittance map will be presented, considering two different dielectric media, i.e., air and water, and the diffraction orders 1 and -2. In this analysis transmittance as a function of azimuth angle has been measured for different light incident angle, in order to completely characterize the bare grating and compare experimental and simulated results [91].

Diffraction order 1 SPPs in air

The total transmittance signal has been measured and compared with RCWA simulation results for the excitation of order 1 SPPs, as can be seen in figure 4.14. The transmittance map cross-section at azimuthal angle 0° presents a maximum in transmittance at the incident angle ϑ_c that satisfies the condition $Re(k_{spp}) = n_{air}k_0 \sin(\vartheta_c) + G$.

The critical point (ϑ_c,0) also corresponds to the maximum value of the transmittance map. A cross section of the transmittance map at a fixed incident angle $\vartheta < \vartheta_c$ shows only a maximum in transmittance at $\varphi = 0$, whose intensity decreases as ϑ decreases. For incident angle $\vartheta > \vartheta_c$ the transmittance shows two maxima at $\varphi = \pm\varphi_r$. In the map of figure 4.14 only $+\varphi_r$ is reported due to map symmetry in φ. As can be seen, in this case the peak intensity decreases as ϑ increases. This behavior is described also by the vector model (green line in figure 4.14 c), where no resonance could occur for $\vartheta < \vartheta_c$ and over this critical value the maxima are present at $\pm\varphi_r$. Figure 4.14 also shows that the experimental position of the azimuthal maximum matches the curve predicted from the vector model with a correlation factor of 0.9991.

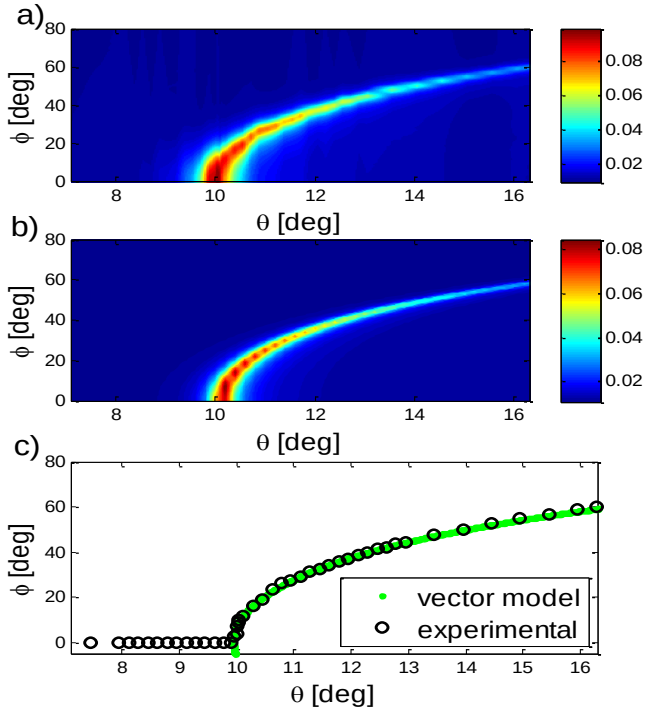

Figure 4.14: Normalized experimental SPR transmittance measured in air for m = 1 (a); simulated SPR transmittance for m = 1 (b); comparison between φ maximum position for different ϑ values obtained from vector model (green curve) and experimental measurements (black dots) (c).

Diffraction order -2 SPPs in air

SPPs at silver-air interface could be excited also for m = -2. For azimuthal angle fixed at 0, the transmittance as a function of incident angle reaches a maximum when $Re(k_{spp}) = n_{air}k_0 \sin(\sin\theta_c) - 2G$. Both the simulated and the experimentally measured SPR azimuthal angles are similar to the case m = 1, and a similar analysis of incident angle ϑ can be performed (see Figure 4.15). The correlation factor between the measured and the simulated angular peak positions is 0.9996. In this case the simulated and the measured transmittance of the background signal have both the same order of magnitude. Conversely, the simulated peak transmittance value is five times greater than the correspondent measured one. This difference can be ascribed to some defects of the grating periodicity not taken into account in the simulation models: the impact of these defects is negligible for order 1 but can no longer be ignored for order -2.

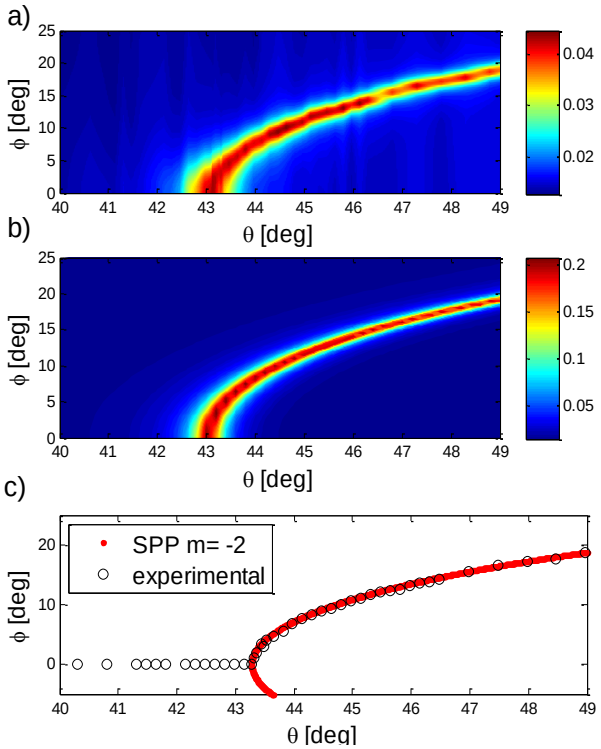

Figure 4.15: Normalized experimental SPR transmittance measured in air for m = -2 (a); simulated SPR transmittance for m = -2 (b); maximum position for different ϑ values obtained from vector model (red curve) and experimental measurements (black dots) (c).

Diffraction order 1 SPP in water

Similar analysis have been performed in ultrapure water buffer (n_d=1.333), and the grating has been embedded in the microfluidic chip described in section 2.4. As in the previous case a cross section of the transmittance map at a fixed incident angle $\vartheta < \vartheta_c$ shows a maximum in transmittance at $\varphi = 0$, meanwhile a cross section of the transmittance map at an incident angle $\vartheta > \vartheta_c$ shows two maximum at $\varphi = \pm\varphi_r$.

An excellent correlation factor of 0.9991, between experimentally measured peak position, and vector model simulated one is found. And both the transmittance values of peaks and baseline results to be in good agreement (figure 4.16).

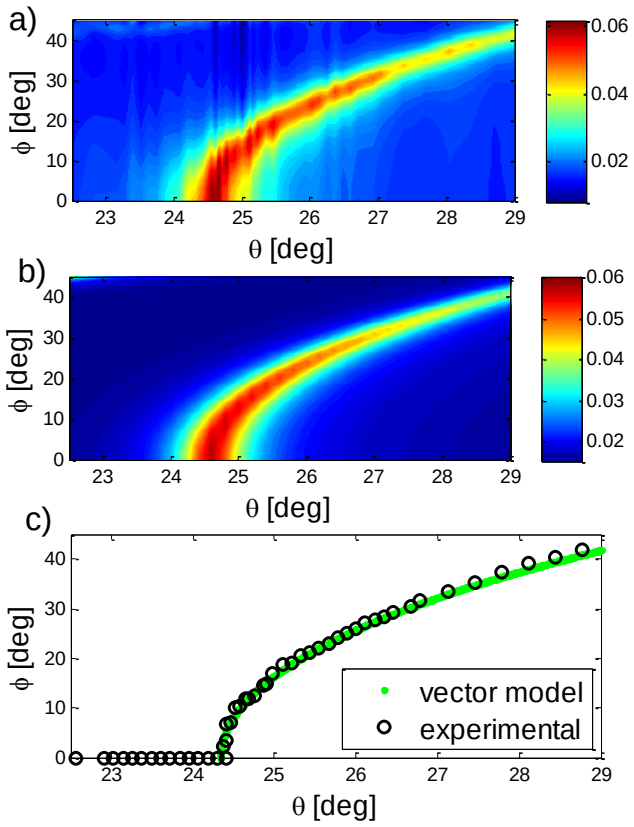

Figure 4.16: Normalized experimental SPR transmittance in water buffer for m = 1 (a); simulated SPR transmittance for m = 1 (b); maximum position for different ϑ values obtained from vector model (red curve) and experimental measurements (black dots) (c).

Diffraction order -2 SPP in water

The analysis of peaks with m = -2 gives similar results to those obtained from the correspondent air case. The correlation factor between experimentally measured peaks positions and vector model simulated one is 0.9984 (see Figure 4.17).

As can be seen, the background signal of the measured transmittance has the same order of magnitude of the simulated one, instead the peak value measured is lower. This is probably due to come geometrical inaccuracies that are not considered in the simulations.

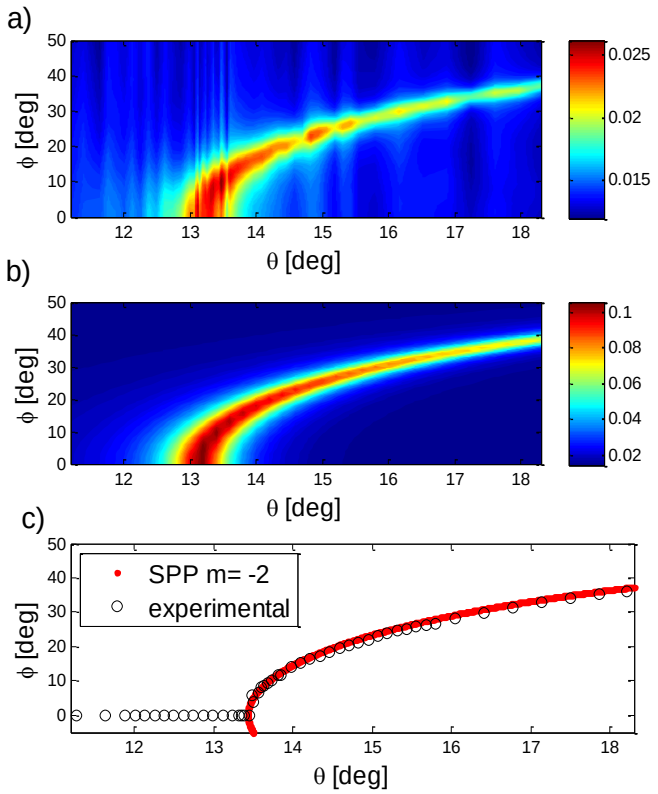

Figure 4.17: Normalized experimental SPR transmittance in water buffer for m= -2 (a);simulated SPR transmittance for m = -2; maximum position for different ϑ values obtained from vector model (red curve) and experimental measurements (black dots) (c).

The presented work demonstrates that the SPPs excitation can be effectively monitored by using gratings with specifically transmittance-optimized geometrical parameters and a compact optoelectronic measurement set up with two degrees of freedom. The simulations well describe the behavior of the device, that can be exploited

as surface for SPR sensing. This aspect will be analyzed through functionalization process and solution with different refractive index in the next sections.

A detailed analysis on the impact of the four diffracted rays on the total transmittance has been also investigated and it is reported in Appendix A.

4.3.3 Response to bulk variations of refractive index: analysis with different solutions

Silver trapezoidal grating behavior to bulk variations of refractive index has been evaluated through measurements of solutions of water and glycerol at different concentrations. We have used glycerol instead of saline solution as in gold sinusoidal grating case (4.1.2) because the sodium-chlorate deteriorates the silver layer. By analyzing the resonance shift for an increasing concentration of solution flowing through the cell, it is possible to calibrate the sensing device and get an estimation of its resolution and sensitivity to refractive index changes.

Sensor sensitivity in the case of GCSPR sensor in azimuthal angle modulation is given by:

$$S = \frac{\Delta\varphi}{\Delta n} \tag{4.3}$$

that is the ratio between the peak azimuthal angle variation and the refractive index variation.

The correlation between glycerol concentration and refractive index has been studied by David R. Lide [92], and the correspondent values are reported in table 4.5.

Glycerol percentage concentration	0%	2%	5%	10%	20%	30%	40%	50%	60%
Refractive index of solution	1.333	1.3353	1.3388	1.3448	1.3572	1.3703	1.3841	1.3982	1.4129
Refractive index variation Δn	0.0	0.0023	0.0058	0.0118	0.0242	0.0373	0.0533	0.0653	0.0799

Table 4.5: Correlation between glycerol concentration in solution and the refractive index of the solution. The third line reported the refractive index variation with respect of water (n_{water}=1.333).

Azimuthal peak variation Δφ reaches its maximum for incident angle closed to the critical value ϑ_c (see section 4.3.2), where transmittance peaks occur at azimuthal angles near to zero: this corresponds to high sensor sensitivity. Δφ decreases as the incident angle differs from the critical value ϑ_c. This means that the sensitivity depends

on the incoming light incident angle and the identification of the correct angle is crucial for sensor performance.

Silver gratings have been embedded in the microfluidic chip (see section 2.4) and fixed on the motorized rotation stage. The different solutions flowed through the chip thanks the peristaltic pump.

First we have fixed the incident angle in order to detect all the analyzed refractive indexes of the solutions (ϑ=27°), and the measured transmittance as a function of azimuthal angle is shown in figure 4.18, that shows the data referred to a single grating and each line corresponds to the mean of three measurements.

We can note that most of the curves have four peaks: the two central ones are due to the diffraction order 1, while the two external ones are due to the order -2. These peaks have a different behavior to refractive index variation, in fact order 1 peaks shift to the null azimuthal angle as the solution refractive index increases, instead order -2 peaks shift to azimuthal angles with higher magnitude.

This different behavior to refractive index changes implies a different incident angle optimization, that will be discussed in detail in this section. So we now analyze order 1 SPPs excitation and the role of the incident angle on sensor sensitivity.

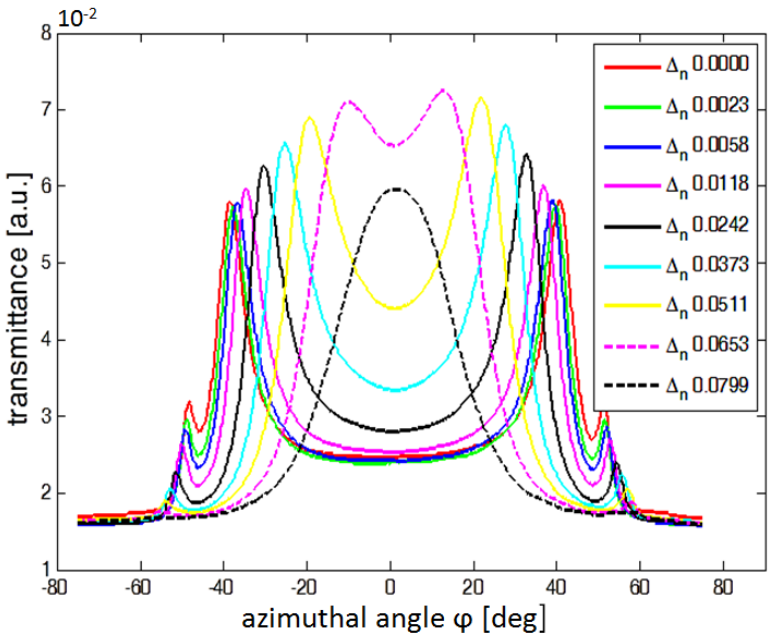

Figure 4.18: Transmittance measurements as a function of azimuthal angle of solutions with different refractive indexes. The legend reports the refractive index variation with respect of the water. The curves refer to one grating and each line represents the mean of three measurements.

Figure 4.18 shows the transmittance as a function of azimuth angle and the peak due to SPPs order 1 are featured for all the solutions analyzed.

The corresponding order 1 azimuthal angles of peak as a function of refractive index variation are shown in figure 4.19. Only positive peak angles are reported since they are symmetric with respect of null angle. As we can see from the figure, the increase of refractive index variation implies a lower resonance azimuthal angle, until the resonance occurs at φ=0° and the transmittance presents only one peak.

The curve slope corresponds to the sensors sensitivity that is maximum near Δn=0.0799 where the transmittance has only one peak in φ=0°.

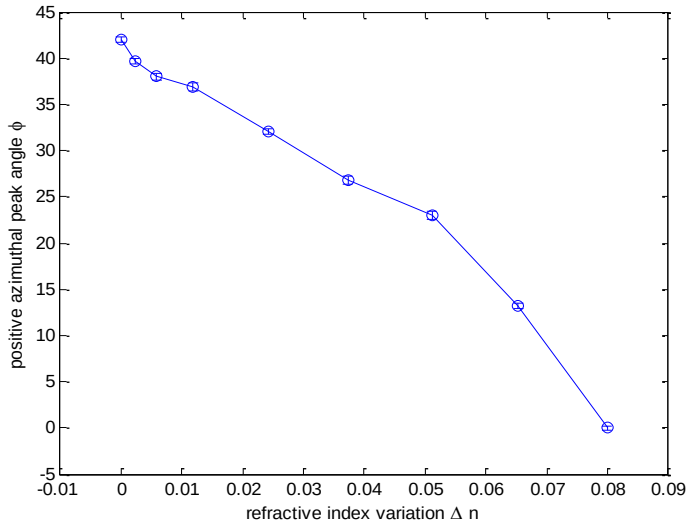

Figure 4.19: Positive azimuthal peak angles as a function of refractive index variation.

If the refractive index variation that must be detected is known, the azimuthal peak variation can be maximized by fixing the incident angle ϑ in order to have only one transmittance peak at null azimuthal angle. This ϑ value can be derived from the simulation by considering a medium with the known refractive index.

Considering a non-optimized incident angle as in figure 4.18, a refractive index variation Δn=0.0058 implies an azimuthal peak angle variation of about 4°, so the sensor sensitivity is 690°/RIU. The optimization of incident angle (figure 4.20) increases the azimuthal peak angle variation up to 14.5° and a sensitivity of 2500°/RIU is achieved. This experimental sensitivity results slightly higher than the simulated one (see section 3.3-figure 3.15); in fact the simulated azimuth angle variation due to a refractive index

variation of 0.005 RIU is about 10°, and the sensitivity is 2000°/RIU. This small discrepancy is probably due to some differences between the simulated geometry and the real one.

The error on azimuth angle estimation σ_φ for a single device is given by the measurement error (see section 2.2.3) and the resolution $\sigma_{n,\varphi} = \sigma_\varphi / S$ is about $7.6 \cdot 10^{-6}$.

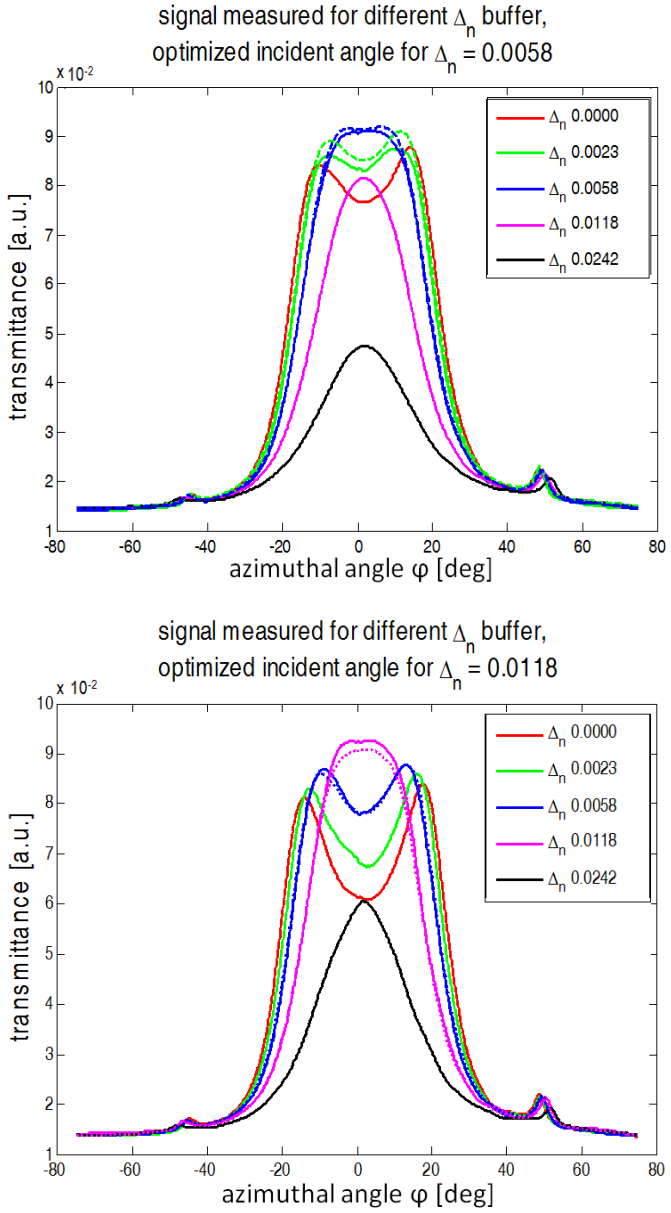

Figure 4.20: Transmittance measurements as a function of azimuthal angle of solutions with different refractive indexes. The legend reports the refractive index variation with respect of the water. The curves represent the mean of three measurements. The incident angle has been fixed for optimized the angle variation for Δn=0.0058 (upper) and Δn=0.0118 (lower).

The same considerations can be done also for the SPPs order -2. As previously mentioned, the transmittance peak in this case shifts to azimuthal angles with higher magnitude (figure 4.21). The following figure shows transmittance as a function of azimuthal angle for a non-optimized incident angle ϑ.

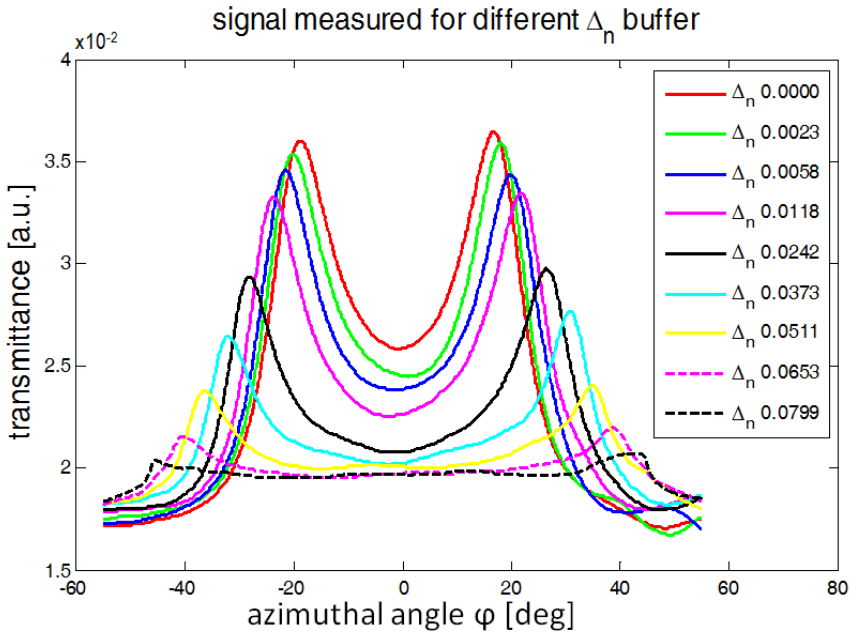

Figure 4.21: Transmittance as a function of azimuthal angle in the case of SPPs order -2 excitation and non-optimized incident angle, for solutions with different refractive indexes

For SPPs order -2, ϑ optimization must be performed on reference refractive index (in our case Δn=0), i.e. the transmittance in this case should have only one peak at φ=0° (figure 4.22), since a refractive index variation implies a peak azimuth angle higher in magnitude than the reference one.

The sensitivity is lower than the sensitivity achieved for the order 1. For the case of Δn=0.0058, the resonance azimuth angle variation is about 11° and a sensitivity of 1380°/RIU is obtained. The angle variation, and consequently the sensitivity, is in agreement with the simulated one (see section 3.3-figure 3.15).

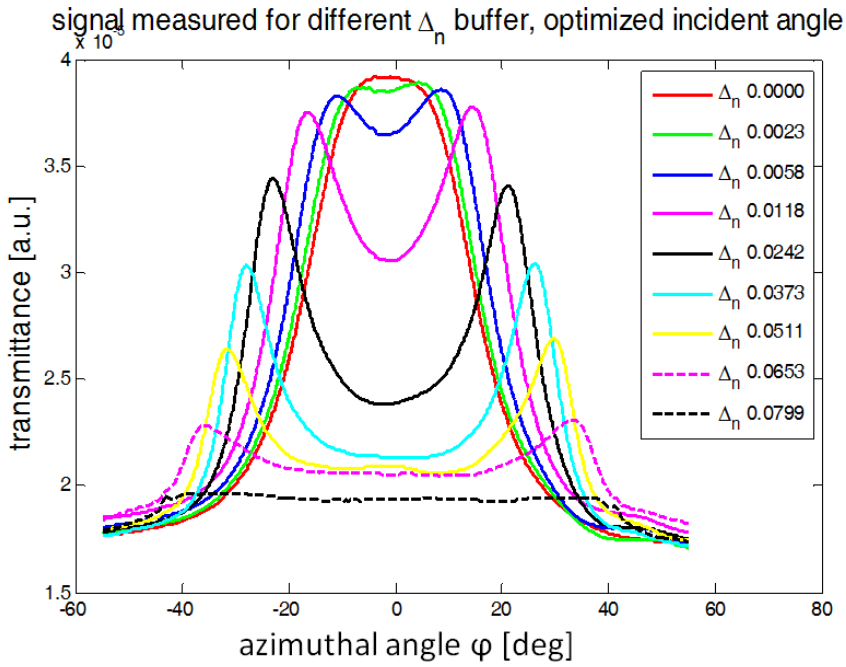

Figure 4.22: Transmittance as a function of azimuthal angle in the case of SPPs order -2 excitation and optimized incident angle with respect of Δn=0, for solutions with different refractive indexes

Measurements of bulk media with different refractive indexes allowed us to estimate sensors sensitivity and resolution and to study how the incident angle affects these performance values.

4.3.4 Measurements of surface refractive index variations: functionalization with increasing length alkanethiols

Further studies of grating functionalization with self-assembled monolayers (SAM) have been performed. In particular, we analyzed the optical response to functionalization with thiolate molecules, in our case alkanethiols, that bind to the gold surface in the form of a compact thin monolayer, thanks to the great affinity of the sulphur group with silver, of known thickness and refractive index.

The effective refractive index variations Δn_{eff} with respect to the bare grating of the various alkanethiols SAM are calculated through EMA (section 2.3) and reported in table 4.6. As it can be noted, the effective refractive index variation increases with carbon-chain length increasing (0.0023÷0.0074).

Alkanethiol SAM	Δn_{eff}
C_6	0.0023
C_8	0.0052
C_{12}	0.0068
C_{18}	0.0074

Table 4.6: Effective refractive index variation due to the alkanethiols self assembled monolayer

Two different functionalization protocols have been performed:

- Overnight immersion in a solution of ethanol and alkanethiol 10 mM
- Drop-casting of a solution of glycerol and alkanethiol 10 mM

Now we analyze the results obtained through the two methods, that focus on SPPs order 1 analysis.

Immersion tests

The gratings have been immersed overnight in a solution of ethanol and alkanethiol 10 mM, and then they have been rinsed in abundant deionized water and dried in nitrogen flux. Nine gratings for each functionalization process have been measured, initially fixing the incident angle at 11° and the results are shown in figure 4.23. Nine samples have been kept in pure ethanol for the same time of the functionalization process, to control that the solvent does not alter the grating surface (yellow line in figure 4.23).

The peaks azimuth angles measured for the various SAM are reported in table 4.7. The value is the mean of nine samples.

As we can see from figure 4.23 and table 4.7, there is a small variation between the bare gratings and gratings kept overnight in ethanol, but it can be negligible in the evaluation of SAM azimuthal peak variation.

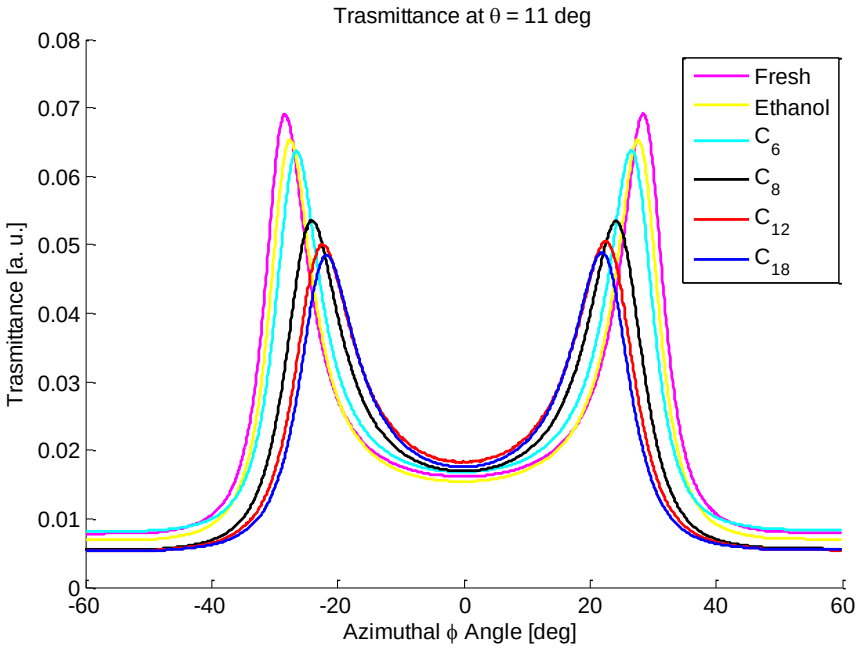

Figure 4.23: Transmittance measurements as a function of the azimuthal angle for fresh gratings, gratings kept in ethanol, C_6 10 mM (in ethanol), C_8 10 mM (in ethanol), C_{12} 10 mM (in ethanol),C_{18} 10 mM (in ethanol) overnight functionalized samples. Each curve is the mean of 9 samples.

Samples	**φ_{peak} [deg]**
Fresh	28.3±0.38
Ethanol	27.6±0.27
C_6	26.6±0.33
C_8	24.1±0.34
C_{12}	22.4±0.42
C_{18}	21.8±0.35

Table 4.7: Mean and standard deviation, referred to 9 samples, of the peak azimuth angle measured for the various SAM

In figure 4.24 the resonance azimuth angle variations are shown as a function of the refractive index variation with respect to the bare grating. The slope of the curve in figure 4.24 can give an idea of the sensor sensitivity for the detection of alkanethiols, that is $S_{n,\varphi}=\Delta\varphi/\Delta n$. The average sensitivity is 823°/RIU, but it can be increased since the incident angle was not optimized. To calculate the refractive index resolution $\sigma_{n,\varphi}= \sigma_\varphi / S_{n,\varphi}$ of a single device, we can consider the azimuthal angle standard deviation

σ_φ =0.019° found through bench characterization (see section 2.2.3) and a resolution $\sigma_{n,\varphi}$ of $2.3 \cdot 10^{-5}$ is obtained.

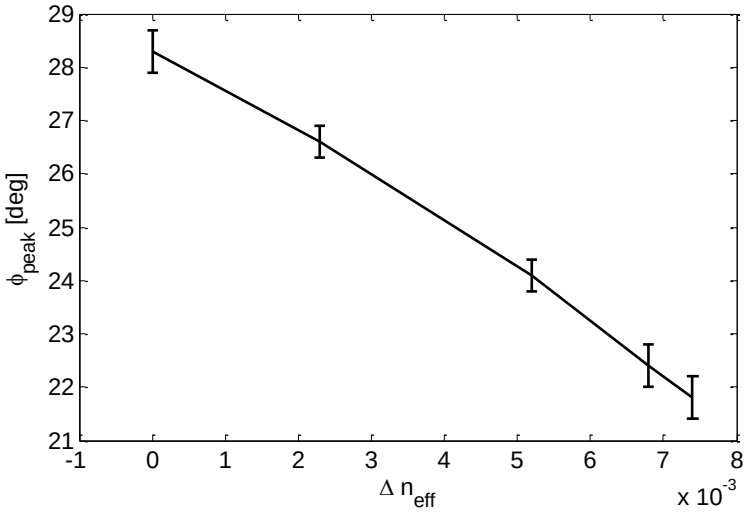

Figure 4.24: Peak azimuthal angle measured as a function of effective refractive index variation

Figure 4.25 shows the results obtained by incident angle optimization for the detection of a specific alkanethiol. In our case we have optimized the detection of the hexanethiol (C_6), the dodecanethiol (C_{12}) and the octadecanethiol (C_{18}), i.e. transmittance presents only a peak at azimuth angle φ=0° when gratings have been functionalized with the specific alkanethiol.

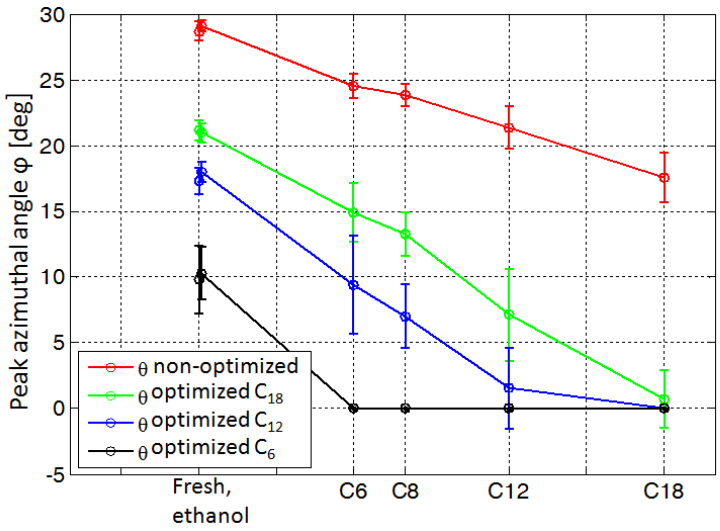

Figure 4.25: Peak azimuthal angles for bare and functionalized gratings obtained by the incident angle optimization. “Fresh” is referred to the bare grating, and “ethanol” to the bare grating kept in ethanol for the same alkanethiols functionalization time.

As we can see from the figure, the azimuthal angle variation is increased through incident angle optimization. For example, concerning octadecanethiol detection, the variation $\Delta\varphi_{peak}$ is 21.18° for the optimized incident angle compared to 11.14° for the non-optimized one, so the sensitivity is enhanced up to 2862°/RIU. A sensitivity more than 4000°/RIU can be reached for hexanethiol detection. The high standard deviation, that can be noted in figure 4.25, is due to the variability between the various measured gratings. For this reason we have considered as the error on azimuthal angle estimation σ_φ the measurement error (see section 2.2.3) obtaining a resolution of the order of 10^{-6}.

Drop–casting tests

The gratings functionalization with alkanethiols has been also performed by drop-casting. In this case alkanethiols have been dissolved in glycerol that is less volatile than ethanol and its high surface tension allows a stable drop on the surface.

Transmittance measurements are shown in figure 4.26. Each curve is the mean of nine samples and the incident angle has been fixed to 11° as in the measurements of figure 4.23.

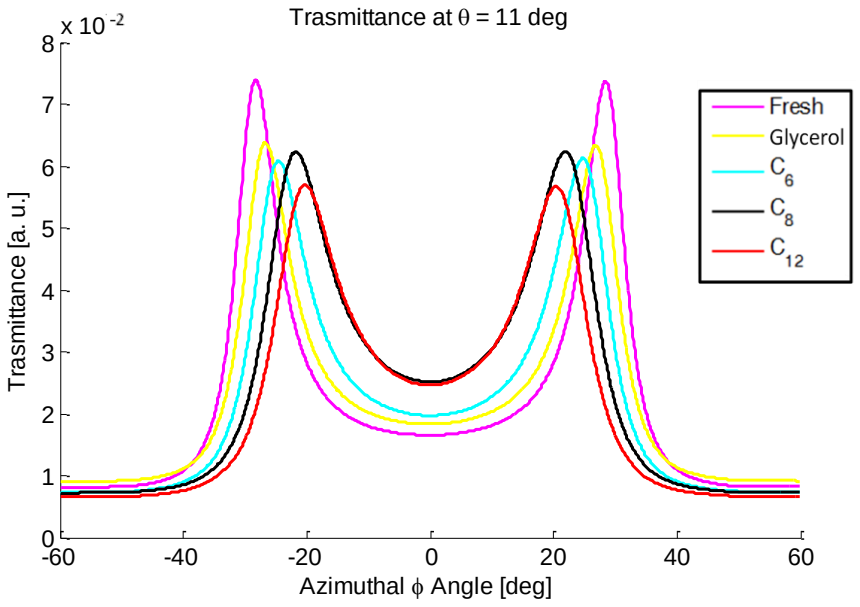

Figure 4.26: Transmittance measurements as a function of the azimuthal angle for fresh grating and grating kept in glycerol, C_6 10 mM (in glycerol), C_8 10 mM (in glycerol), C_{12} 10 mM (in glycerol) overnight functionalized samples. Each curve is the mean of 9 samples.

The correspondent peaks azimuth angles for the various SAM are reported in table 4.8 and in figure 4.27 the same values are shown as a function of the refractive index variation with respect to the bare grating.

Samples	**φ_{peak} [deg]**
Fresh	28.3±0.33
Glycerol	27.2±0.32
C_6	24.7±0.53
C_8	21.9±1.3
C_{12}	20.5±0.50

Table 4.7: Mean and standard deviation of the peak azimuth angle measured for the various SAM

The resolution can be calculated considering the measurement error as azimuth angle estimation error σ_φ and a value of about $1x10^{-6}$ is found.

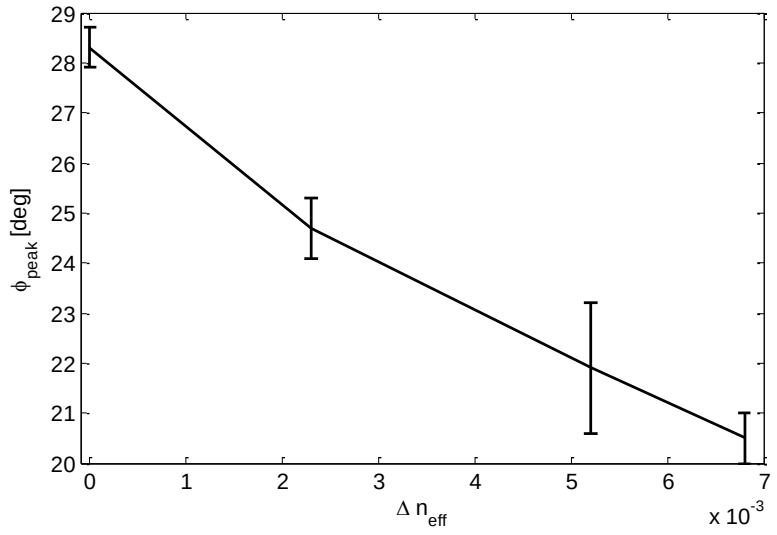

Figure 4.27: Peak azimuthal angle measured as a function of effective refractive index variation

Functionalization has been done with alkanethiols with increasing chain length, allowing the formation of increasing thickness/density dielectric layers, determining gradually higher variations in effective refractive index and a correspondent increasing variation of peak azimuth angle.

Silver grating system has proved to be suitable for sensing applications, since peak azimuth angle variation increases with SAM thickness increasing. The sensitivity estimated is high and can be enhanced up by incident angle optimization.

5 Conclusions

Plasmonic gratings have proved to assure a high sensitivity to surface refractive index variation due to functionalization or molecule detection, and they represent a promising component for the realization of miniaturized label-free devices for sensing applications with considerable performance in refractive index sensitivity and resolution.

A compact bench has been developed in order to measure the plasmonic event and to transduce it into an electric signal. Its versatility allows to perform both reflectance and transmittance analysis, automating the measurements by using a motorized stage.

Three different gratings have been analyzed and used for sensing applications, evaluating different parameter modulations. Preliminary simulations have been performed in order to evaluate sensor behavior as a function of specific set-up parameters and to compare the theoretical results with the experimental ones.

Gold sinusoidal grating has been measured in incident light polarization modulation, exploiting the sensitivity increase due to a non-zero azimuthal angle. The phase term of a polarization scan has been experimentally demonstrated to be a sensing parameter for surface functionalization analysis and for the detection of molecules of medical interest, such as avidin and DNA chain. In the presented prototype the control of azimuthal and incident angles is allowed only for a whole study of this sensing setup, but in a supposed commercial version, they can be fixed at the proper position, and the only variable component would be the rotating polarizer. The analysis of the phase shift for increasing sodium-chloride concentration of water solution flowing through the microfluidic chip has provided an estimation of sensitivity and resolution, respectively of about 200°/RIU and $5 \cdot 10^{-7} \div 1 \cdot 10^{-6}$ RIU. Further research is needed in order to completely understand phase-term shift dependence on refractive index changes, and to evaluate other sensor performance such as the reproducibility and the limit of detection.

Gold digital grating have been realized to exploit the light extraordinary optical transmission. The focus of this analysis was to realize a simple grating-coupled SPR sensor reducing the degree of freedom. Light source impinges perpendicularly the grating and the transmittance variation when light is in TM mode is considered the

sensing parameter. The proposed system has a simple measurement protocol based on polarization modulation, but it could be further simplified fixing the incident light at TM mode. The prototype has been experimentally tested to prove its capability to detect surface variations due to a functionalization process with dodecanethiol SAM. Its ability to detect such thin layer suggests that this type of system could be used for bio-recognition applications and the simple measurement protocol makes it suitable to miniaturization. Further research is needed to make the system reproducible, especially the gratings fabrication.

Silver trapezoidal gratings have been fabricated through an industrial process of plastic material, and I have contributed to their realization thanks a collaboration with a Spin-Off. This technology transfer proves the potentiality of grating-coupled SPR sensor for a mass production, reducing the cost. The sensing strategy is based on the detection of the device transmitted signal intensity maxima instead of the commonly used order zero reflectance minima. They have been first characterized in bare condition, both in air and water buffer, measuring the angles ϑ and φ that correspond to SPR excitations, and the results are in good agreement with RCWA simulations and with the vector model. Silver gratings have been analyzed in azimuthal angle modulation, exploiting the sensitivity enhance of incident angle optimization. The analysis of the resonance azimuthal angle shift for increasing glycerol concentration of water solution flowing through the microfluidic chip has provided an estimation of sensitivity and resolution, respectively of 2500°/RIU and $3.5 \cdot 10^{-5}$ RIU. The capability of the system to detect self-assembled monolayer has also been tested through functionalization with alkanethiols with increasing chain length, whose layers have been distinguished by increasing resonance azimuth angle variation. By properly fixing the incident angle, on the basis of simulated data, a sensitivity greater than 4000°/RIU can be reached. Gratings production process assures a good reproducibility and further research will be done to improve the resolution and evaluate the limit of detection. The system will be applied for other sensing applications, such as the detection of microorganisms, exploiting the binding antibody/membrane proteins, and DNA chains.

Appendix A

Analysis of diffracted rays output angle for the silver trapezoidal grating

Silver trapezoidal grating has been analyzed in bare condition considering both air and water buffer (section 4.3.2) [91]. In each analyzed case, when the grating is lighted with the laser beam four diffracted rays (DRs) are transmitted into the polycarbonate substrate, i.e., T_{-2}, $T_{-1,}$ T_0 and T_1 as illustrated in Figure A1.

We will show that all the diffracted rays exhibit typical features of the SPPs resonance in fact a surface plasmon excited at the metal/dielectric interface is converted into radiation by a diffraction grating when the diffracted rays satisfy momentum matching between SPP and output ray angle given by:

$$sin(\vartheta_{out}) = \frac{-m_p G cos(\varphi_{out}) \pm \sqrt{-m_p{}^2 G^2 \sin^2(\varphi_{out}) + Re^2(k_{spp})}}{k_0 \eta_p}$$

where η_p is the polycarbonate substrate refraction index (1.58) and m_p is the grating order that allows the plasmon decoupling process.

Solving this vector model equation we found the pair (ϑ_{out}, φ_{out}) that could allow SPPs decoupling into the polycarbonate substrate.

We used the RCWA model to characterize diffracted rays behavior when order 1 SPPs is excited at silver/air interface. To achieve this we report each diffracted rays transmittance as a function of (ϑ_{out}, φ_{out}). Then the results from the two simulation methods are compared as shown in figures A1-A4.

Figure A1 shows the T_1 diffracted ray transmittance as function of (ϑ_{out}, φ_{out}). This is the most important diffracted rays and refers to the Kretschmann decoupling.

The transmittance peak resonance feature is described by the vector model using $m_p = 0$. It is independent from φ_{out} and it occurs at a fixed output angle $\vartheta_{out} = 40.9°$. This output angle is exactly the same that must be used to reach SPPs excitation at the silver/air interface in a Kretschmann configuration. In fact it is the angle that solves the sequent equation:

$$Re(k_{spp}) = \eta_p k_0 \sin(\theta)$$

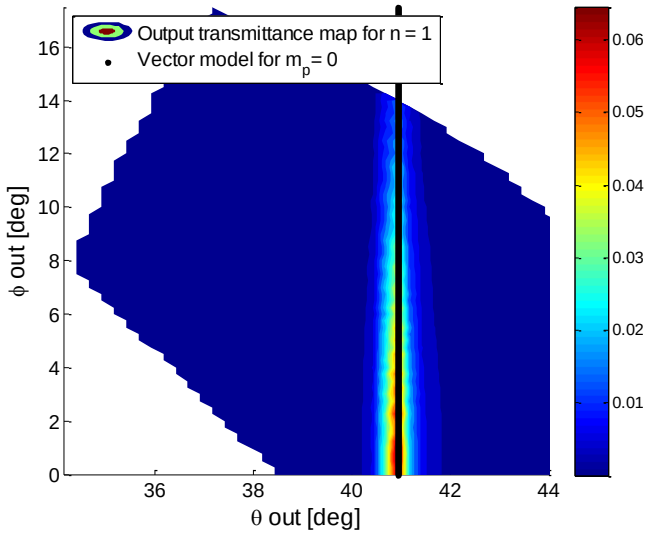

Figure A1: Transmittance map for T_1. Resonance features is independent from φ_{out} and the output angle ϑ_{out} fits the vector model results for m_p = 0, i.e., Kretschmann diffracted rays.

By comparing the peak transmittance value of T_1 (0.06 a.u.) with the total transmittance peak values (0.08 a.u.), see figure 4.14a and 4.14b of section 4.3.2, it can be observed that the total peaks transmittance is mainly due to this diffracted ray: in fact it determines the 87 % of total transmittance intensity.

The angle ϑ_{out} where transmittance peak occurs is subjected to total internal reflection when the light beam comes across polycarbonate-air interface. For this reason the grating total transmittance can be sensed experimentally only if the grating substrate is very close to the photodiode sensitive area [93], collecting in this way much of the output Kretschmann ray transmittance. Grating substrate and photodiodes must be perfectly optically matched to guarantee refractive index continuity by using an optical matching oil.

In Figure A2 the transmittance map for T_0 (i.e. the order zero diffraction order) shows a weak resonance that well overlap the result given by the vector model for m_p = 1. This diffracted ray is the one ruled by Snell's law at air-polycarbonate interface.

Its transmittance value varies in a restricted range (0.010÷0.013 a.u.). Referring to the transmittance map reported in figure 4.14a and 4.14b we notice that T_0 contributes mainly to the baseline transmittance value.

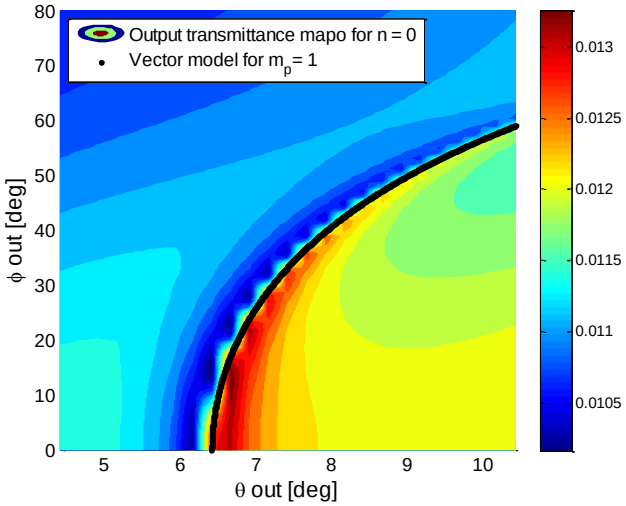

Figure A2: Transmittance map for T_0. Resonance features fit the vector model for m_p = -1. In this case the resonance is not a peak and the map represents a quasi-homogeneus transmittance value.

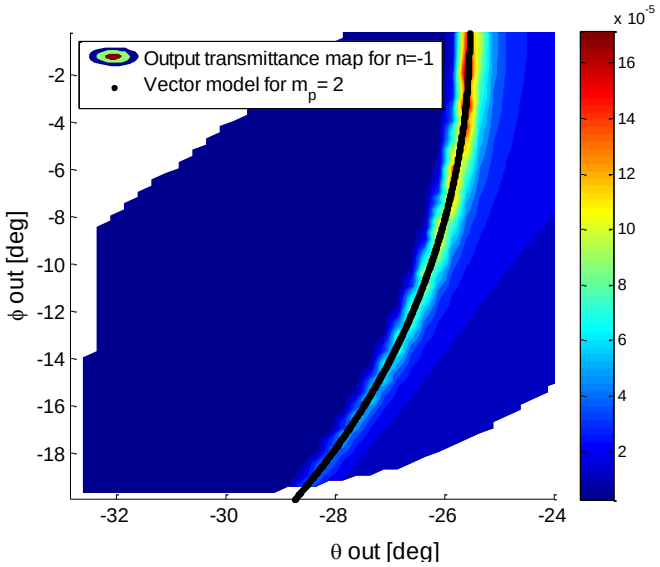

Figure A3: Transmittance map for T_{-1}. The resonance features fit the vector model results for m_p=2

The transmittance map for T_{-1} (Figure A3) shows a resonance well reproduced by the vector model results for m_p = 2. Noticeably the peak resonance values is two orders of magnitude smaller than T_1 peak shown in figure A1. This means that the contribution on total transmittance provided by this diffracted ray is negligible.

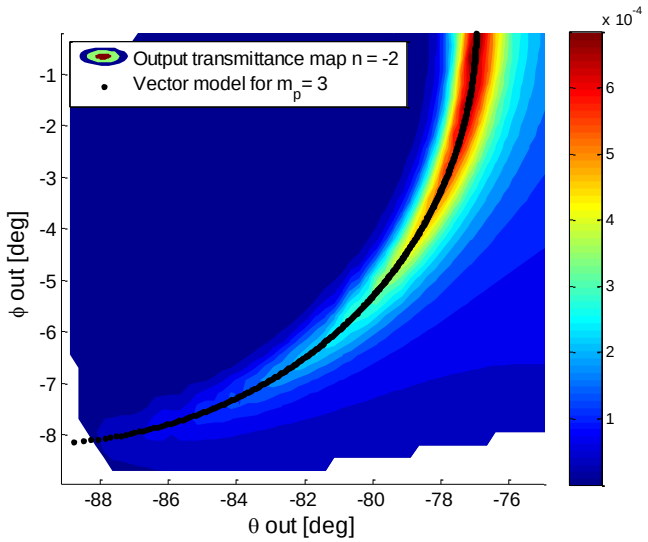

Figure A4: Transmittance map for T_{-2}. The resonance features fit the vector model results for m_p=3.

The T_{-2} transmittance map resonance feature (figure A4) is closely described by the vector model considering m_p = 3. The transmittance intensity related to this diffracted ray is negligible as in case of T_{-1}.

This analysis that we have performed for order 1 SPPs excitation at silver/air interface can be done for every SPP excitation order and for all type of dielectrics in contact with silver (table A1 and A2).

	SPP order 1	
n	m_p	DR
1	0	k
0	1	b
-1	2	--
-2	3	--

Table A1 Relation between the n-th diffracted order and the decoupling constant m_p for m=1 SPP excitation order. Results reported into the table are valid for both air and water dielectrics. Letters “k” and “b” stand for Kretschmann ray and baseline ray, respectively.

Table A1 summarizes the relation between the n-th diffracted order and the decoupling constant m_p we previously analyzed for the SPPs excitation order 1 at silver/air interface. As we previously found among all the DRs, the Kretschmann ray (mark in the table using “k”) carries most of the transmittance in resonance condition

(figure A1). T_0 (figure A2) is the other important diffracted ray that influences the baseline transmittance value (has been indicated with the “b”).

The other two rays can be neglected due to the fact that their transmittance is two orders of magnitude smaller than the transmittance carried by “k” and “b” rays and they are marked in table with “--”.

The Table relation is valid when SPPs order 1 is excited for every dielectric in contact with silver.

It is possible to expand what has been shown in detail for m=1 SPPs also to the case m = -2 SPPs which is a different way to excite the SPPs at silver/air or silver/water interface using such type of grating with a 635 nm wavelength.

	SPP order -2	
n	m_p	DR
1	-3	--
0	-2	b
-1	-1	--
-2	0	k

Table A2. Relation between the n-th diffracted order and the decoupling constant m_p for m=-2 SPP excitation order. Results reported into the table are valid for both air and water. Letters “k” and “b” stand for Kretschmann ray and baseline ray, respectively.

Table A2 shows the relation between the n-th diffracted order and the decoupling constant m_p in case of SPPs -2 order excitation.

As in order 1 SPPs two of these rays mostly influence the total transmittance signal: the one related to transmittance baseline, i.e., T_0, ruled by Snell’s law, and the one related to the Kretschmann decoupling ray, i.e., T_{-2}.

Acknowledgment

I would like to thank everyone who has accompanied me in this PhD experience, especially my colleagues, that have strictly collaborated with me, and my supervisor Prof. Paccagnella, that gave me this opportunity.

I cannot forget my parents, which have always supported me in every decision, because they believe in my capacity, even after twenty-four years of study!

I thank also all my friends, for the good leisure, especially my childhood friends, because I grew up and matured with them. Thanks to my roommate Chiara that has shared with me the everyday life during my PhD.

Finally I thank my partner, that has supported me during all my PhD period and he gives me the serenity.

Thank you all...

Bibliography

[1] R. W. Wood, "On a remarkable case of uneven distribution of light in a diffraction grating spectrum", *Philos. Mag. 4,* pp. 396-402, 1902.

[2] U. J. Fano, "The Theory of Anomalous Diffraction Gratings and of Quasi-Stationary Waves on Metallic Surfaces (Sommerfeld's Waves)", *Opt. Soc. Am. 31,* pp. 213-222, 1941.

[3] A. Otto, "Excitation of nonradiative Surface Plasma Waves in Silver by the Method of Frustrated Total Reflection", *Z. Phys. 216,* pp. 398-410, 1968.

[4] E. Kretschmann and H. Z. Raether, "Radiative decay of non-radiative surface plasmons excited by light", *Naturforsch 23,* pp. 2135-2136, 1968.

[5] J. J. Cowan and E. T. Arakawa, "Dispersion of surface plasmons in dielectric-metal coatings on concave diffraction gratings", *Zeitschrift fur Physik 235,* p. 97, 1970.

[6] S. A. Maier, "Plasmonics: Fundamentals and Applications", Springer, 2007.

[7] J. Homola, "Surface Plasmon Resonance Sensors for Detection of Chemical and Biological Species", *Chemical Reviews, Vol.108, n.2,* pp. 462-492, 2008.

[8] H. Raether, Surface Plasmons on Smooth and Rough Surfaces and on Gratings, Springer, 1988.

[9] J. Homola, "Surface Plasmon Resonance Based Sensors", Berlin, Germany: Springer, 2006.

[10] J. Homola, S. S. Yee and G. Gauglitz, "Surface Plasmon resonance sensors: review", *Sensors and Actuators B 54,* pp. 3-15, 1999.

[11] K. Matsubara, S. Kawata and S. Minami, "A compact Surface Plasmon Resonance Sensor for Measurement of Water in Process", *Appl. Spectrosc. 42,* pp. 1375-1379, 1988.

[12] L. M. Zhang and D. Uttamchandam, "Optical chemical sensing employing surface plasmon resonance", *Electron. Lett. 24,* p. 1469, 1988.

[13] A. D. Kersey, T. A. Berkoff and W. W. Morey, "High-resolution fibre-grating based strain sensor with interferometric wavelength-shift detection", *Electronics Letters, Vol. 28, Issue 3,* pp. 236-238, 1992.

[14] C. Nylander, B. Liedberg and T. Lind, "Gas detection by means of surface plasmon resonance", *Sensors and Actuators 3,* pp. 79-88, 1982.

[15] J. M. Brockman, B. P. Nelson and R. M. Corn, "Surface plasmon resonance imaging measurements of ultrathin organic films", *Annu. Rev. Phys. Chem. 51,* pp. 41-63, 2000.

[16] K. Kukanskis, J. Elkind, J. Melendez, T. Murphy, G. Miller and H. Garner, "Detection of DNA hybridization using the TISPR-1 surface plasmon resonance biosensor", *Anal. Biochem. 274,* pp. 7-17, 1999.

[17] S. Sjolander and C. Urbanitzky, "Integrated fluid handling system for biomolecular interaction analysis", *Anal. Chem. 63,* pp. 2338-2345, 1991.

[18] T. M. Chinowsky, L. S. Jung and S. S. Yee, "Optimal linear data analysis for surface plasmon resonance biosensors", *Sens. Actuators B 54,* pp. 89-97, 1999.

[19] K. Johansen, R. Stalberg, I. Lundstrom and B. Liedberg, "Surface Plasmon Resonance: Instrumental Resolution using Photo Diode Arrays", *Meas. Sci. Tech. 11,* pp. 1630-1638, 2000.

[20] V. Thomsen, D. Schatzlein and D. Mercuro, "Limits of detection in spectroscopy", *Spectroscopy 18,* pp. 112-114, 2003.

[21] G. A. Besselink, R. P. Kooyman, G. H. Enqbers and R. B. Schasfoort, "Signal amplification on planar and gel-type sensor surfaces in surface plasmon resonance-based detection of prostate-specific antigen", *Anal. Biochem.,* vol. 333, no. 1, pp. 165-173, 2004.

[22] H. Vaisocherovà, K. Mrkvovà, M. Piliarik, P. Jinoch, M. Steinbachovà and J. Homola, "Surface plasmon resonance biosensor for direct detection of antibody against Epstein-Barr virus.", *Biosens. Bioelectron.,* vol. 22, no. 6, pp. 1020-1026, 2007.

[23] J. F. Masson, L. Obando, S. Beaudoin and K. Booksh, "Sensitive and real-time fiber-optic-based surface plasmon resonance sensors for myoglobin and cardiac troponin I", *Talanta,* vol. 62, no. 5, pp. 865-870, 2004.

[24] T. J. Kim, H. S. Cho, N. Y. Park and J. I. Lee, "Serodiagnostic comparison between two methods, ELISA and surface plasmon resonance for the detection of antibody titres of Mycoplasma hyopneumoniae", *J. Vet. Med. Ser. B: Infect. Dis. Vet. Public Health,* vol. 53, no. 2, pp. 87-90, 2006.

[25] P. P. Dillon, S. J. Daly, B. M. Manning and R. O'Kennedy, "Immunoassay for the determination of morphine-3-glucuronide using a surface plasmon resonance-

based biosensor", *Biosensors & Bioelectronics,* vol. 18, no. 2-3, pp. 217-227, 2003.

[26] J. W. Chung, R. Bernhardt and J. C. Pyun, "Sequential analysis of multiple analytes using a surface plasmon resonance (SPR) biosensor", *J. Immunol. Methods,* vol. 311, no. 1-2, pp. 178-188, 2006.

[27] O. Lazcka, F. Javier Del Campo and F. X. Munoz, "Pathogen detection: A perspective of traditional methods and biosensors", *Biosensors & Bioelectronics,* vol. 22, no. 7, pp. 1205-1217, 2007.

[28] L. D. Mello and L. T. Kubota, "Review of the use of biosensors as analytical tools in the food and drink industries", *Food Chemistry,* vol. 77, no. 2, pp. 237-256, 2002.

[29] P. M. Fratamico, T. P. Strobaugh, M. B. Medina and A. G. Gehring, "Detection of Escherichia coli 0157:H7 using a surface plasmon resonance biosensor", *Biotechnology Technique,* vol. 12, no. 7, pp. 571-576, 1998.

[30] M. Minunni and M. Mascini, "Detection of Pesticide in Drinking Water Using Real-Time Biospecific Interaction Analysis (BIA)", *Anal. Lett.,* vol. 26, pp. 1441-1459, 1993.

[31] E. S. Forzani, H. Zhang, W. Chen and N. Tao, "Detection of Heavy Metal Ions in Drinking Water Using a High-Resolution Differential Surface Plasmon Resonance Sensor", *Environ. Sci. Technol.,* vol. 39, no. 5, pp. 1257-1262, 2005.

[32] M. Shimomura, Y. Nomura, W. Zhang, M. Sakino, K. H. Lee, K. Ikebukuro and I. Karube, "Simple and rapid detection method using surface plasmon resonance for dioxins, polychlorinated biphenylx and atrazine", *Anal. Chem. Acta,* vol. 434, pp. 223-230, 2001.

[33] K. E., "The determination of the Optical Constants of Metals by Excitation of Surface Palsmons", *Z. Phys.,* vol. 241, pp. 313-324, 1971.

[34] R. Karlsson and R. Stahlberg, "Surface plasmon resonance detection and multispot sensing for direct monitoring of interactions involving low-molecular-weight analytes and for determination of low affinities", *Anal. Biochem.,* vol. 228, no. 2, pp. 274-280, 1995.

[35] J. Homola, I. Koudela and S. S. Yee, "Surface plasmon resonance sensor based on diffraction gratings and prism couplers: sensitivity comparison", *Sensors & Actuators B Chem.,* vol. 54, pp. 16-24, 1999.

[36] G. G. Nenninger, P. Tobiska, J. Homola and S. S. Yee, "Long-range surface plasmons for high-resolution surface plasmon resonance sensors", *Sensors & Actuators B,* vol.

74, no. 1-3, pp. 145-151, 2001.

[37] R. Slavìk and J. Homola, "Ultrahigh resolution long range surface plasmon-based sensor", *J. Sens. Actuators B,* vol. 123, no. 1, pp. 10-12, 2007.

[38] J. Melendex, R. Carr, D. U. Bartholomew, K. Kukanskis, J. Elkind, S. Yee, C. Furlong and R. Woodbury, "A commercial solution for surface plasmon sensing", *Sensors & Actuactors B,* vol. 35, p. 212, 1996.

[39] T. M. Chinowsky, J. G. Quinn, D. U. Bartholomew, R. Kaiser and J. L. Elkind, "Performance of the Spreeta 2000 integrated surface plasmon resonance affinity sensor", *Sensors & Actuators B,* vol. 91, pp. 266-274, 2003.

[40] X. D. Hoa, A. G. Kirk and M. Tabrizian, "Towards integrated and sensitive surface plasmon resonance biosensors: a review of recent progress", *Sensors & Actuators B Chem.,* vol. 54, no. 1-2, pp. 16-24, 1999.

[41] K. H. Yoon, M. L. Shuler and S. J. Kim, "Design and optimization of nano-grating surface plasmon resonance sensors", *Opt. Express,* vol. 14, no. 11, pp. 4842-4249, 2006.

[42] J. Dostalek, J. Homola and M. Miler, "Rich information format surface plasmon resonance biosensor based on array of diffraction gratings", *Sensors & Actuators B Chem.,* vol. 107, no. 1, pp. 154-161, 2005.

[43] O. Telezhnikova and J. Homola, "New approach to spectroscopy of surface plasmons", *Opt. Lett.,* vol. 31, no. 22, pp. 3339-3341, 2006.

[44] S. Moon, Y. Kim, Y. Oh, H. Lee, H. C. Kim, K. Lee and D. Kim, "Grating-based surface plasmon resonance detection of core-shell nanoparticle mediated DNA hybridization", *Biosensors & Bioelectronics,* vol. 32, no. 1, pp. 141-147, 2012.

[45] A. Shalabney and I. Abdulhalim, "Sensitivity-enhancement methods for surface plasmon sensors", *Laser & Photonics Reviews,* vol. 5, no. 4, pp. 571-606, 2011.

[46] G. Zacco, F. Romanato, A. Sonato, D. Sammito, G. Ruffato, M. Morpurgo, D. Silvestri, M. Carli, P. Schiavuta and G. Brusatin, "Interferential lithography of 1D thin metallic sinusoidal gratings: accurate control of the profile for azimuthal angular dependent plasmonic effects and applications", *Microelecron. Eng. ,* no. 86, pp. 573-576, 2009.

[47] G. Zacco, F. Romanato, A. Sonato, D. Sammito, G. Ruffato, M. Morpurgo, D. Silvestri, M. Carli, P. Schiavuta and G. Brusatin, "Sinusoidal plasmonic crystal for bio-detection sensors", *Microelectron. Eng.,* no. 88, pp. 1898-1901, 2011.

[48] G. Ruffato, E. Pasqualotto, A. Sonato, G. Zacco, D. Silvestri, M. Morpurgo, A. De Toni and F. Romanato, "Implementation and testing of a compact and high-resolution sensing device based on grating-coupled surface plasmon resonance with polarization modulation", *Sensors and Actuators B: Chemical,* no. 185, p. 179– 187, 2013.

[49] T. W. Ebbesen, H. J. Lezec, H. F. Ghaemi, T. Thio and P. A. Wolff, "Extraordinary optical transmission through sub-wavelength hole arrays", *Nature,* vol. 391, pp. 667-669, 1998.

[50] P. Lalanne, J. P. Hugonin and J. C. Rodier, "Theory of surface plasmon generation at nanoslit apertures", *Phys. Rev. Lett.,* vol. 95(26), p. 263902, 2005.

[51] L. Salomon, F. Grillot, A. V. Zayats and F. De Fornel, "Near-field distribution of optical transmission of periodic subwavelength holes in a metal film", *Phys. Rev. Lett,* vol. 86(6), pp. 1110-1113, 2001.

[52] F. J. Garcia-Vidal, L. Martin-Moreno, T. W. Ebbesen and L. Kuipers, "Light passing through aubwavelength apertures", *Rev. Mod. Phys.,* vol. 82(1), pp. 729-787, 2010.

[53] P. Zilio, D. Sammito, G. Zacco and F. Romanato, "Absorption profile modulation by means of 1D digital plasmonic gratings", *Optics Express,* vol. 18(19), pp. 19558-19565, 2010.

[54] A. Barbara, P. Quémerais, E. Bustarett and T. Lopez-Rios, "Optical transmission through subwavelength metallic gratings", *Phys. Rev. B,* vol. 66(16), p. 161403, 2002.

[55] Y. Pang, C. Genet and T. Ebbesen, "Optical transmission through subwavelength slit apertures in metallic films", *Opt. Commun.,* vol. 280(1), pp. 10-15, 2007.

[56] T. Ongarello, F. Romanato, P. Zilio and M. Massari, "Polarization independence of extraordinary transmission through 1D metallic gratings", *Optics Express,* vol. 19(10), pp. 9416-9433, 2011.

[57] W. W. Hu, K. Sarveswaran, M. Lieberman and G. H. Bernstein, "Sub-10 nm electron beam lithography using cold development of poly (methylmethacrylate)", *Journal of Vaccum Science & Technology B: Microelectronics and Nanometer Structures,* vol. 22(4), pp. 1711-1716, 2004.

[58] C. Vericat, M. E. Vela and R. C. Salvarezza, "Self-assembled monolayers of alkanethiols on Au(111): surface structures, defects and dynamics", *Phys . Chem. Chem. Phys .,* vol. 7, pp. 3258-3268, 2005.

[59] B. K. Singh and A. C. Hillier, "Surface Plasmon Resonance Enhanced Transmission of Light through Gold-Coated Diffraction Gratings", *Anal. Chem.,* vol. 80, pp. 3803-3810, 2008.

[60] L. S. Jung and C. T. Campbell, "Sticking Probabilities in Adsorption from Liquid Solutions: Alkylthiols on Gold", *Physical Review Letters,* vol. 84, no. 22, pp. 5164-5167, 2000.

[61] L. S. Jung, C. T. Campbell, T. M. Chinowsky, M. N. Mar and S. S. Yee, "Quantitative Interpretation of the Response of Surface Plasmon Resonance Sensors to Adsorbed Films", *Langmuir,* vol. 14, pp. 5636-5648, 1998.

[62] R. Desikan, S. Armel, H. M. Meyer and T. Thundat, "Effect of chain length on nanomechanics of alkanethiol self-assembly", *Nanotechnology,* vol. 18, pp. 424028-424034, 2007.

[63] M. Wilcheck and E. A. Bayer, Avidin/biotin thechnology, San Diego: Academic Press, 1990.

[64] S. Fornera, T. E. Balmer, B. Zhang, A. D. Schluter and P. Walde, "Immobilization of peroxidase on SiO2 surfaces with the help of a dendronized polymer and the avidin-biotin system", *Mocromolecular Bioscence,* vol. 11, pp. 1052-1067, 2011.

[65] M. Heuberger, T. Drobek and N. D. Spencer, "Interaction Forces and Morphology of a Protein-Resistant Poly(ethylene glycol) Layer", *Biophys. J.,* vol. 88(1), pp. 495-504, 2005.

[66] C. Pale-grosdemange, E. S. Simon, K. L. Prime and G. M. Whitesides, "Formation of self-assembled monolayers by chemiosorption of derivatives of oligo(ethylene glycol) of structure HS(CH2)11(OCH2CH2)mOH on gold", *J. Am. Chem. Soc.,* vol. 113(1), pp. 12-20, 1991.

[67] J. M. Harris and S. Zalipsky, Poly(ethylene glycol): Chemistry and Biological Applications, New York: Plenum Press, 1992.

[68] P. Harder, M. Grunze, R. Dahint, G. M. Whitesides and P. E. Laibinis, "Molecular conformation in oligo(ethylene glycol)-terminated self-assembled monolayers on gold and silver surfaces determines their ability to resist protein adsorption", *J. Phys. Chem. B,* vol. 102(2), pp. 426-436, 1998.

[69] M. Dettin, D. Silvestri, R. Danesin, E. Cretaio, G. Piccariello, E. Casarin, A. Sonato, F. Romanato and M. Morpurgo, "Synthesis and chromatography-free purification of PNA-PEO conjugates for the functionalization of gold sensors", *Molecules,* vol. 17(9), pp. 11026-11045, 2012.

[70] S. Busse, V. Scheumann, B. Menges and S. Mittler, "Sensitivity studies for specific binding reactions using the biotin/streptavidin system by evanescent optical methods", *Biosensors & Bioelectronics,* vol. 17(8), pp. 704-710, 2002.

[71] M. I. Pividori, A. Merkoçi and S. Alegret, "Electrochemical genosensor design: immobilisation of oligonucleotides onto transducer surfaces and detection methods", *Biosensors & Bioelectronics,* vol. 15, pp. 291-303, 2000.

[72] M. Dettin, D. Silvestri, R. Danesin, E. Cretaio, G. Picariello, G. Casarin, A. Sonato, F. Romanato and M. Morpurgo, "Synthesis and chromatography-free purification of PNA-PEO conjugates for the functionalization of gold sensors", *Molecules,* vol. 17(9), pp. 11026-11045, 2012.

[73] M. Natali, S. Begolo, T. Carofiglio and G. Mistura, "Rapid phototyping of multilayer thiolene microfluidic chips by photopolymerization and transfer lamination", *Lab on Chip,* vol. 8, pp. 492-494, 2008.

[74] J. T. Cabral, S. D. Hudson, C. Harrison and J. F. Douglas, "Frontal photopolymerization for microfluidic applications", *Langmuir,* vol. 20, no. 9, pp. 10020-10029, 2004.

[75] F. Romanato, K. H. Lee, H. K. Kang, C. C. Wong, Y. Zong and W. Knoll, "Azimuthal dispersion and energy mode condensation of grating-coupled surface plasmon polaritons", *Phys. Rev. B 77,* pp. 245435-245441, 2008.

[76] F. Romanato, K. H. Lee, H. K. Kang, G. Ruffato and C. C. Wong, "Sensitivity enhancement in grating coupled surface plasmon resonance by azimuthal control", *OPTICS EXPRESS 14, Vol.17,* pp. 12145-12154, 2009.

[77] G. Ruffato and F. Romanato, "Grating-Coupled Surface Plasmon Resonance in the Conical Mounting with Polarization Modulation", *Optics Letters, Vol. 37, Issue 13,* pp. 2718-2720, 2012.

[78] A. Karabchevsky, O. Krasnykov, I. Abdulhalim, B. Hadad, A. Goldner, M. Auslender and S. Hava, "Metal grating on a substrate nanostructure for sensor applications", *Photonics and Nanostructures- Fundamentals and Applications,* vol. 7(4), pp. 170-175, 2009.

[79] R. Gordon, D. Sinton, K. L. Kavanagh and A. G. Brolo, "A new generation of sensors based on extraordinary optical transmission", *Accounts of chemical research,* no. 41, pp. 1049-1057, 2008.

[80] M. Sadiku, "Numerical techniques in electromagnetics with MATLAB", CRC Press, Taylor & Francis Group, 2009.

[81] M. G. Moharam, E. B. Grann, D. A. Pommet and T. K. Gaylord, "Formulation for stable and efficient implementation of the rigorous coupled-wave analysis of binary gratings", *J. of Optical Society of America A,* vol. 12, no. 5, pp. 1068-1076, 1995.

[82] V. K. Singh, B. B. S. Jaswal, V. Kumar, R. Prakash and P. Rai, "Application of He-Ne laser to study the variation of refractive index of liquid solutions with the concentration", *J. Integr. Sci. Technol.,* vol. 1, no. 1, pp. 13-18, 2013.

[83] N. E. Dorsey, Properties of ordinary water-substance, New York: Rainhold Publishing Corporation, 1940.

[84] J. Chandezon, D. Maystre and G. Raoult, "A new theoretical method for diffraction gratings and its numerical applications", *J. Optics,* vol. 11, pp. 235-241, 1980.

[85] L. D. Unsworth, Z. Tun, H. Sheardown and J. L. Brash, "Chemisorption of thiolated poly (ethylene oxide) to gold: surface chain densities measured by ellipsometry and neutron reflectometry", *J. Coll. Inter. Sci.,* vol. 281, no. 1, pp. 112-121, 2005.

[86] H. Fujiwara, Spectroscopic Ellipsometry – Principles and Applications, Chichester, England: John Wiley & Sons, 2007.

[87] E. Pasqualotto, G. Ruffato, A. Sonato, G. Zacco, D. Silvestri, M. Morpurgo, A. De Toni and F. Romanato, "Plasmonic platforms for innovative surface plasmon resonance configuration with sensing applications", *Microelectronic Engineering,* vol. 111, p. 348–353, 2013.

[88] G. Ruffato, E. Pasqualotto, A. Sonato, G. Zacco, D. Silvestri, M. Morpurgo, A. De Toni and F. Romanato, "Implementation and testing of a compact and high-resolution sensing device based on grating-coupled surface plasmon resonance with polarization modulation", *Sensors and Actuators B,* pp. 179-187, 2013.

[89] G. Ruffato, E. Pasqualotto, A. Sonato, G. Zacco, D. Silvestri, M. Dettin, M. Morpurgo, A. De Toni and F. Romanato, "Novel compact architecture for high-resolution sensing with plasmonic gratings in conical mounting", in *Proc. of SPIE Vol. 8722*, 2013.

[90] E. Özkumur, A. Yalçın, M. Cretich, C. A. Lopez, D. A. Bergstein, B. B. Goldberg, M. Chiari and M. S. Ünlü, "Quantification of DNA and Protein Adsorption by Optical Phase Shift", *Biosens. Bioelectron. ,* vol. 25, no. 1, pp. 167-172, 2009.

[91] M. Perino, E. Pasqualotto, M. Scaramuzza, A. De Toni and A. Paccagnella, "Characterization of Grating Coupled Surface Plasmon Polaritons using diffracted rays transmittance", *submitted to Plasmonics.*

[92] D. R. Lide, "CRC Handbook Chemistry and Physics", 2004.

[93] B. Turker, H. Guner, S. Ayas, O. Ekiz, H. Acar, M. O. Guler and A. Dana, "Grating coupler integrated photodiodes for plasmon resonance based sensing", *Lab on a chip,* vol. 11, no. 2, pp. 282-287, 2011.

[94] M. G. Moharam, D. A. Pommet and E. B. Grann, "Stable implementation of the rigorous coupled-wave analysis for surface-relief gratings: enhanced transmittance matrix approach", *J. Opt. Soc. Am. A., Vol. 12, No. 5,* pp. 1007-1086, 1995.

[95] J. C. McDonald, D. C. Duffy, J. R. Anderson, D. T. Chiu, H. Wu, O. J. A. Schueller and G. M. Whitesides, "Fabrication of microfluidic system in poly(dimethylsiloxane)" , *Electrophoresis,* vol. 21, no. 1, pp. 27-40, 2000.

[96] K. Johansen, R. Stalberg, I. Lundstrom and B. Liedberg, "Surface plasmon resonance: instrumental resolution using photo diode arrays", *Meas. Sci. Technol.,* vol. 11, no. 11, pp. 1630-1638, 2000.